

Saratov State University (National Research University of Russia)

**Chinese-Russian Workshop on
Biophotonics and Biomedical Optics-2020
Book of Abstracts**

Edited by Polina A.Dyachenko, Dan Zhu, and
Valery V.Tuchin

SEPTEMBER 29 – 30, 2020

SARATOV



УДК 535.8
ББК 22.34
К 45

Китайско-российский семинар по биофотонике и биомедицинской оптике-2020. Сборник тезисов/ под ред. Дьяченко П. А., Чжу Д., Тучина В. В. – Саратов, Российская Федерация, Ухань, КНР: Саратовский источник, 2020 – 97 с. [Электронный ресурс]. – Электрон, текстовые дан.(30 Мб) — 1 электрон, опт. диск (CD-ROM)

Chinese-Russian Workshop on Biophotonics and Biomedical Optics-2020. Book of Abstracts/ Edited by P.A.Dyachenko, D. Zhu, and V.V.Tuchin –Saratov, Russian Federation and Wuhan, P.R. China: Saratov source, 2020 – 97 p –[Electronic resource]. - Electron, text data.(30 MB) -- 1 electron, opt. disk (CD-ROM).

Saratov State University (National Research University of Russia), 410012, Saratov, Astrakhan str., 83

ISBN 978-5-6045836-2-3

The collection includes extended abstracts of lectures and reports of the participants of the Chinese-Russian Workshop on Biophotonics and Biomedical Optics, held online as part of the Saratov Fall Meeting 2020.

В сборник вошли расширенные тезисы лекций и докладов участников китайско-российского семинара по биофотонике и биомедицинской оптике, проходившего в режиме онлайн в рамках Саратовской осенней встречи 2020 года.

УДК 535.8
ББК 22.34

© Saratov State University, 2020

TABLE OF CONTENTS

INTRODUCTION: CHINESE-RUSSIAN WORKSHOP ON BIOPHOTONICS AND BIOMEDICAL OPTICS-2020.....	6
1. EARLY DIAGNOSIS OF DISEASES BY LABEL-FREE, HIGH-RESOLUTION, MULTIPARAMETRIC IMAGING, Zhiyi LIU, Jia MENG, Shuhao QIAN, Shenyi JIANG, and Zhihua DING.....	8
2. NIR SKULL OPTICAL CLEARING WINDOW FOR IN VIVO CORTICAL VASCULATURE IMAGING AND TARGETED MANIPULATION, Dong-yu LI, Zheng ZHENG, Ting-Ting YU, Ben Zhong TANG, Peng FEI, Jun QIAN and Dan ZHU.....	10
3. <i>IN VIVO</i> RAMAN SPECTROSCOPY FOR CHRONIC DISEASES DETECTION, Ivan BRATCHENKO, Lyudmila BRATCHENKO, Yulia KHRISTOFOROVA, Dmitry ARTEMYEV, Oleg MYAKININ, Alexander MORYATOV, Sergey KOZLOV, Peter LEBEDEV and Valery ZAKHAROV.....	13
4. PROGRESS ON STIMULATED EMISSION DEPLETION MICROSCOPY, Junle QU, Wei YAN, Zhigang YANG, Luwei Wang, Jia ZHANG and Jialin WANG.....	14
5. OPTICAL TECHNIQUES FOR ASSESSING BLOOD MICRORHEOLOGY: RED BLOOD CELLS DEFORMABILITY, AGGREGATION AND THEIR INTERRELATION, Andrei LUGOVTSOV, Anastasia MASLYANITSINA, Petr ERMOLINSKIY and Alexander PRIEZZHEV.....	17
6. MULTIPARAMETER OPTICAL DIAGNOSTICS OF MICROCIRCULATORY-TISSUE SYSTEMS: METHODS AND TECHNICAL MEANS, Andrey DUNAEV.....	19
7. CORRELATION OF HEMORHEOLOGIC PARAMETERS MEASURED <i>IN VITRO</i> AND <i>IN VIVO</i> BY DIFFERENT OPTICAL TECHNIQUES IN PATIENTS SUFFERING FROM VARIOUS SOCIALLY IMPORTANT DISEASES, Alexander PRIEZZHEV, Andrei LUGOVTSOV, Anastasia MASLYANITSINA, Petr ERMOLINSKIY and Yuri GURFINKEL.....	21
8. STRUCTURAL AND FUNCTIONAL OPTICAL COHERENCE TOMOGRAPHY, TECHNOLOGY AND APPLICATIONS, Zhihua DING, Zhiyi LIU, Jianrong QIU, Jia MENG, Tao HAN.....	23
9. MOUSE: ADVANCED APPROACHES TO SKIN <i>IN VIVO</i> OPTICAL CLEARING, Elina A. GENINA, Alexey N. BASHKATOV, Valery V. TUCHIN, and Vladimir P. ZHAROV.....	25
10. HIGH AFFINITY LIGANDS FOR PRECISE TUMOR DIAGNOSIS, Yueqing GU.....	27
11. OPTIMIZATION OF SPECTRAL AND SPATIAL LIGHT BEAM DISTRIBUTION OF OPTICAL SYSTEMS FOR PHOTODYNAMIC THERAPY, Andrey BELIKOV and Yulia SEMYASHKINA.....	28
12. BREAKTHROUGH STRATEGIES OF STIMULATION OF THE CEREBRAL LYMPHATICS DURING SLEEP, Oxana SEMYACHKINA-GLUSHKOVSKAYA, Thomas PENZEL, Jurgen KURTHS, Valery TUCHIN.....	32
13. TISSUE OPTICAL CLEARING: FROM <i>IN VITRO</i> TO <i>IN VIVO</i> , Dan ZHU.....	36
14. A SUPERSTABLE HOMOGENEOUS LIPIODOL-ICG FORMULATION FOR LOCOREGIONAL HEPATOCELLULAR CARCINOMA TREATMENT, Hu CHEN, Hongwei CHENG and Gang LIU.....	39
15. MINING POLARIZATION FEATURES FROM A MUELLER MATRIX, Dong YANG, Jiachen WAN and Hui MA.....	40
16. GAP-ENHANCED RESONANCE RAMAN TAGS FOR BIOIMAGING, Jian YE.....	43
17. DYNAMIC-RANGE COMPRESSION AND CONTRAST ENHANCEMENT IN SWEEP SOURCE OPTICAL COHERENCE TOMOGRAPHY, Shanshan LIANG, Xinyu LI, Yao QIN and Jun ZHANG.....	44
18. MULTISCALE PHOTOACOUSTIC MICROSCOPY, Lei XI.....	45
19. OPTICAL MICROENDOSCOPY AND ITS APPLICATIONS, Ling FU.....	46
20. BIOMEDICAL APPLICATIONS OF NONLINEAR OPTICAL MICROIMAGING TECHNIQUES, Shiqi WANG, Fangrui LIN, Sheng REN, Yihua ZHAO and Liwei LIU.....	47
21. LASER-INDUCED LOCAL VASCULAR RESPONSES, Dmitry POSTNOV and Elena LITVINENKO.....	49

22. BREAK THE UNBROKEN LIMITS TOWARD SUPER-RESOLUTION MICROSCOPY, Qiuqiang ZHAN..	51
23. MEDICAL APPLICATIONS OF IR AND THZ LASER MOLECULAR IMAGING AND MACHINE LEARNING, Yu.V. KISTENEV, A.V. BORISOV, A.I. KNYAZKOVA, D.A. VRAZHNOV, V.E. SKIBA, V.V. PRISCHEPA, A. CUISSET.....	53
24. REFRACTIVE PROPERTIES OF BLOOD SERUM OF RATS WITH EXPERIMENTAL LIVER CANCER, Ekaterina N. LAZAREVA, Polina A. DYACHENKO, Maxim M. NAZAROV, Alla B. BUCHARSKAYA, Valery V. TUCHIN, Alexander P. SHKURINOV	54
25. NANOMEDICINE IN CANCER PHOTOIMMUNOTHERAPY, Xiao-Long LIU, Ming WU, Da ZHANG and Zhixiong CAI	56
26. STUDY OF SKIN DEHYDRATION IN THE COURSE OF GRAFTED TUMOR DEVELOPMENT USING SPECTRAL REFRACTOMETRY, NIR AND THZ SPECTROSCOPY, Polina DYACHENKO (TIMOSHINA), Ekaterina LAZAREVA, Maxim NAZAROV, Alla BUCHARSKAYA, Valery TUCHIN ^{1,2,5} and Alexander SHKURINOV	59
27. SILICON NANOMATERIALS FOR BIOSENSING AND BIOIMAGING, Yao HE.....	60
28. DISPERSION-MEDIATED CONJUGATE SUPPRESSION FOR HIGH SPEED OPTICAL COMPUTING OCT IMAGING, Wenxin ZHANG, Chengming WANG, Zhenyu CHEN, Bin HE, Zhangwei HU and Ping XUE	61
29. THE ROLE OF INDIVIDUAL CYSTEINE SUBSTITUTIONS IN THE FAST PHOTOSWITCHING AND PHOTOCONVERSION OF THE BIPHOTOCHROMIC FLUORESCENT PROTEIN SAASOTi, Alexandra GAVSHINA, Nadezhda MARYNICH and Alexander SAVITSKY.....	63
30. STUDY ON THE RELATIONSHIP BETWEEN REDUCED SCATTERING COEFFICIENT AND YOUNG'S MODULUS IN MICROWAVE ABLATION, Zhiyu QIAN, Xiaofei JIN and Yu FENG.....	65
31. IMAGING PROCESSING OF LASER SPECKLE CONTRAST IMAGING OF BLOOD FLOW, Weimin CHENG, Xiaohu LIU, Jinling LU, and Pengcheng LI.....	68
32. TUMOR MICROENVIRONMENT-RESPONSIVE DRUG DELIVERY SYSTEMS, Yi MA and Yueqing GU	69
33. SAPPHIRE FIBER BUNDLES FOR TERAHERTZ IMAGING WITH SPATIAL RESOLUTION BEYOND THE ABBE LIMIT, K.I. ZAYTSEV, G.M. KATYBA, N.V. CHERNOMYRDIN, I.N. DOLGANOVA, A.S. KUCHERYAVENKO, A.N. ROSSOLENKO, V.V. TUCHIN, V.N. KURLOV, AND M. SKOROBOGATIY	70
34. MONTE CARLO SIMULATION OF THE COVID-19 SPREAD IN EARLY AND PEAK STAGES IN DIFFERENT REGIONS OF THE RUSSIAN FEDERATION USING AN AGENT-BASED MODELLING, Mikhail KIRILLIN, Ekaterina SERGEEVA, Aleksandr KHILOV, Daria KURAKINA, and Nikolay SAPERKIN	71
35. MACS: RAPID AQUEOUS CLEARING SYSTEM FOR THREE-DIMENSIONAL MAPPING OF INTACT ORGANS, Jingtian ZHU, Tingting YU, Yusha LI, Jianyi XU, Yisong QI, Yingtao YAO, Yilin MA, Peng WAN, Zhilong CHEN, Xiangning LI, Hui GONG, Qingming LUO, Dan ZHU.....	75
36. RECENT ADVANCES IN OPTICAL IMAGING FOR PHOTODYNAMIC THERAPY, Buhong LI.....	76
37. ANGIOGENESIS AND GLIAL RESPONSES AFTER NEAR-INFRARED LIGHT ATTENUATES AB BURDEN AND ALLEVIATES COGNITIVE IMPAIRMENTS IN APP/PS1 MICE, Lechan TAO and Xunbin WEI	77
38. MITOGENETIC EFFECT (STIMULATION OF MITOSES WITH ULTRA-WEAK UV-RADIATION) AND ITS APPLICATIONS TO CANCER RESEARCH AND DIAGNOSTICS, Ilya VOLODYAEV and Elena NAUMOVA	80
39. EXPRESS DIAGNOSTICS OF ERYTHROCYTES SIZE DISTRIBUTION ON THE BASIS OF HYPERSPECTRAL HOLOGRAPHY AND LASER DIFFRACTOMETRY TECHNIQUES, Andrei LUGOVTSOV, Vladislav USTINOV, Georgy KALENKOV, Sergey KALENKOV and Alexander PRIEZZHEV	83
40. CHARACTERIZATION OF TISSUE ELASTICITY WITH OPTICAL COHERENCE ELASTOGRAPHY: GOING BEYOND THE LINEAR PARADIGM, Vladimir Y. ZAITSEV, Alexander A. SOVETSKY, Lev A. MATVEEV, Alexander L. MATVEYEV, Ekaterina V. GUBARKOVA, Anton A. PLEKHANOV, Marina A. SIROTKINA and Natalia D. GLADKOVA	85

41. TWO-COMPONENT DIELECTRIC FUNCTION OF GOLD NANOSTARS: NOVEL CONCEPT FOR THEORETICAL MODELING AND ITS EXPERIMENTAL VERIFICATION, Nikolai G. KHLEBTSOV, Sergey V. ZARKOV, Vitaly A. KHANADEEV and Yuri A. AVETISYAN	90
42. MULTIMODAL TISSUE IMAGING AT OPTICAL CLEARING, Valery V. TUCHIN	95



**CHINESE-RUSSIAN WORKSHOP ON
BIOPHOTONICS AND BIOMEDICAL OPTICS-2020**

SEPTEMBER 28 – 30, 2020, SARATOV, RUSSIA

Organized by

Wuhan National Laboratory for Optoelectronics, Huazhong University of Science and Technology, P.R. China
Saratov State University (National Research University of Russia) (SSU)
Research-Educational Institute of Optics and Biophotonics, SSU
International Research-Educational Center of Optical Technologies for Industry and Medicine “Photonics”, SSU
Biomedical Photonics Committee of Chinese Optical Society, P.R. China
SPIE Student Chapter of SSU
OSA Student Chapter of SSU

Chairs

Dan Zhu, Ph. D, Professor, SPIE Fellow, Deputy Director of Wuhan National Laboratory for Optoelectronics, Huazhong University of Science and Technology, Wuhan, China
Valery V Tuchin, Corr.-member of the RAS, Doc. of Sci., Professor, SPIE/OSA Fellow, Head of Optics and Biophotonics Department, Saratov State University; Head of Laboratory of Laser Diagnostics of Technical and Living Systems, Institute of Precision Mechanics and Control of the RAS, Saratov, Russia

Secretaries:

Tingting Yu, Ph. D, Associate Professor, Wuhan National Laboratory for Optoelectronics, Huazhong University of Science and Technology, Wuhan, China
Polina A. Dyachenko, Ph. D, Associate Professor, Optics and Biophotonics Department, Saratov State University, Saratov, Russia

Organizing Committee

Ivan V. Fedosov
Anton A. Dyachenko
Elina A. Genina
Vadim D. Genin
Oleg V. Grishin
Ekaterina N. Lazareva
Dongyu Li
Isabella A. Serebryakova
Michael M. Slepchenkov
Daria K. Tuchina

Chinese-Russian Workshop on Biophotonics and Biomedical Optics-2020 was held online from 28 to 30 September 2020, with the aim of bringing together Russian and Chinese scientists, engineers and clinical researchers from various disciplines engaged in applying optics, photonics and imaging technologies to problems of biology and medicine. The scope of this bilateral Forum ranges from basic research to instrumentation engineering, biological and clinical studies.

The topics of this Forum are broad and will cover (but not limited to) the following:

- Optical Interactions with Tissue and Cells
- Biomedical Spectroscopy, Microscopy and Imaging
- Advanced Optical Techniques for Clinical Medicine
- Optical Molecular Imaging
- Multimodal Biomedical Imaging
- Nano/Biophotonics
- Photonics Therapeutics, Diagnostics and Instrumentations
- Tissue Optical Clearing and Drug Delivery

EARLY DIAGNOSIS OF DISEASES BY LABEL-FREE, HIGH-RESOLUTION, MULTIPARAMETRIC IMAGING

ZHIYI LIU¹, JIA MENG¹, SHUHAO QIAN¹, SHENYI JIANG¹, AND ZHIHUA DING¹

¹State Key Laboratory of Modern Optical Instrumentation, College of Optical Science and Engineering, International Research Center for Advanced Photonics, Zhejiang University, China

liuzhiyi07@zju.edu.cn

Abstract

Disease progression is associated with subtle changes in both cellular metabolism and extracellular matrix organization, especially at early stages [1, 2]. Therefore, detecting early changes of these components in a sensitive and accurate manner can serve as a powerful tool for prediction of diseases and better treatments. However, there are limited techniques that work well for this goal. Two-photon excited fluorescence (TPEF) has emerged as a powerful modality for high-resolution, label-free, quantitative assessments of metabolic activity [3, 4]. Two key coenzymes actively involved in several important metabolic pathways, NAD(P)H and FAD, can provide endogenous fluorescence for these metabolic assessments [5]. Second harmonic generation (SHG) microscopy, another multi-photon modality, is an effective method for direct non-invasive, label-free imaging of collagen fibers (main components in extracellular matrix) in biological tissues at sub-micrometer resolution [6, 7].

In this work, we use TPEF and SHG to acquire images from cells and collagen fibers, respectively, without the need for any exogenous labels. Based on these images, we have developed quantitative, multi-parametric measures, including optical redox ratio and mitochondrial clustering corresponding to cellular metabolic activity, as well as directional variance and fiber concentration representative of collagen spatial organization. A combination of these quantitative metrics can provide systematic investigations of correlation between cells and matrix during progression of diseases.

Figure 1 shows the TPEF images of coenzymes NAD(P)H and FAD within cardiomyocyte spheroids, and optical measures generated to quantify cellular metabolism. The merged image contains three different contrasts, including NADH, FAD and collagen fibers (Fig. 1a). Throughout this study, two optical measures are developed for characterization of cell metabolic activity. The first one is optical redox ratio defined as $FAD / (NADH + FAD)$ (Fig. 1d), which is generated on a per pixel basis relying on raw NADH (Fig. 1b) and FAD (Fig. 1c) images. Optical redox ratio reflects the reduction-oxidation events based on which cells optimize energy production to maintain cellular homeostasis through various metabolic pathways [8]. Meanwhile, mitochondria dynamically fuse and fission to manage energy distribution or to protect the cell from insult [9]. To account for this, we develop the other optical metric which is corresponding to the spatial organization of mitochondria, named mitochondrial clustering, generated from the clone-stamped map (Fig. 1e) of raw NADH image. Briefly, we acquire the power spectral density (PSD) curve (Fig. 1f) of the 2D Fourier transformation of the clone-stamped image, and fit the curve to obtain the exponential power which is an indicator of the mitochondrial clustering level.

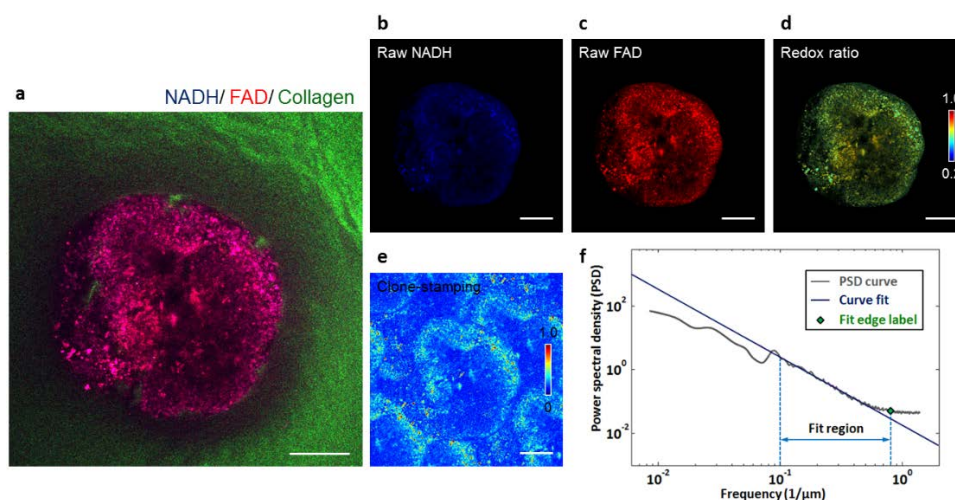


Figure 1. Imaging and quantification of cellular metabolism. (a) Merged image of cardiomyocyte spheroids containing TPEF images of NADH (blue) and FAD (red), and SHG image of collagen fibers (green). (b) Raw NADH image. (c) Raw FAD image. (d) Redox ratio map defined as: $FAD / (NADH + FAD)$ on a per pixel basis. (e) The clone-stamping of raw NADH intensity image used for

assessment of mitochondrial clustering. (f) The power spectral density (PSD) curve generated from the clone-stamped NADH image for acquisition of the exponential power, which is used as a quantitative measure of mitochondrial clustering level. Scale bar: 100 μm . Besides quantitative characterizations of cellular metabolism from TPEF images of coenzymes, we acquire SHG images of collagen fibers from mouse breast tissue (Fig. 2a), and quantify their spatial randomness and density. Directional variance, ranging between 0 and 1, is a measure of spatial alignment, with 0 corresponding to perfect parallel alignment, and 1 corresponding to complete randomness (Fig. 2b) [10, 11]. Fiber concentration, slightly different from fiber density, focuses more on the relationship among collagen fibers in localized regions. It is generated on a per pixel basis and ranges between 0 and 1, with 0 indicating no fibers in neighbouring regions of the assessed pixel, while 1 corresponding to full occupying by collagen fibers in neighbouring regions (Fig. 2c).

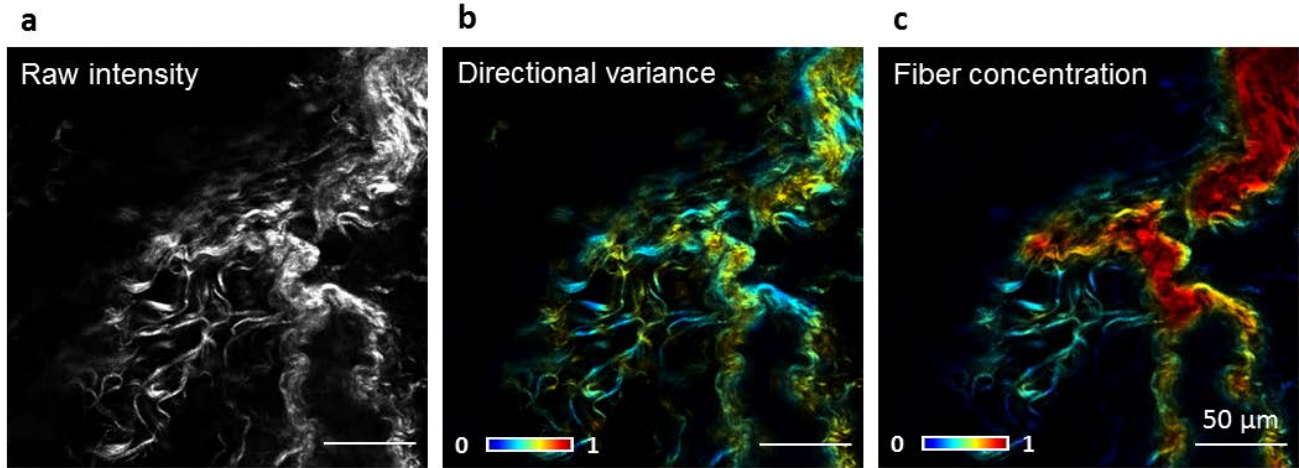


Figure 2. Imaging and quantification of collagen fiber spatial organization. (a) Raw SHG intensity image of mouse breast tissue. (b) The pixel-wise directional variance map of the same field which reflects the fiber alignment. (c) The pixel-wise fiber concentration map. Scale bar: 50 μm .

Overall, in this study we acquire TPEF and SHG images from both cells and extracellular matrix, relying on completely endogenous contrast. Especially, these label-free, high-resolution imaging modalities, along with highly-quantitative characterizations, enable a better understanding of cellular metabolic activity and collagen fiber organization. These optical biomarkers provide complementary insights into the functional and structural alterations at early stages of diseases, and offer opportunities to study interactions between cells and matrix as disease progresses. Thus, a combination of them might serve as a sensitive approach to early diagnosis of diseases.

References

- [1] R.J. DeBerardinis, C.B. Thompson, Cellular metabolism and disease: what do metabolic outliers teach us?, *Cell* 148(6) (2012) 1132-44.
- [2] E. Brown, T. McKee, E. diTomaso, A. Pluen, B. Seed, Y. Boucher, R.K. Jain, Dynamic imaging of collagen and its modulation in tumors in vivo using second-harmonic generation, *Nat Med* 9(6) (2003) 796-800.
- [3] W. Denk, J.H. Strickler, W.W. Webb, Two-photon laser scanning fluorescence microscopy, *Science* 248(4951) (1990) 73-6.
- [4] I. Georgakoudi, K.P. Quinn, Optical imaging using endogenous contrast to assess metabolic state, *Annu Rev Biomed Eng* 14 (2012) 351-67.
- [5] M.C. Skala, K.M. Riching, A. Gendron-Fitzpatrick, J. Eickhoff, K.W. Eliceiri, J.G. White, N. Ramanujam, In vivo multiphoton microscopy of NADH and FAD redox states, fluorescence lifetimes, and cellular morphology in precancerous epithelia, *Proc Natl Acad Sci U S A* 104(49) (2007) 19494-9.
- [6] Y. Zhang, M.L. Akins, K. Murari, J. Xi, M.J. Li, K. Luby-Phelps, M. Mahendroo, X. Li, A compact fiber-optic SHG scanning endomicroscope and its application to visualize cervical remodeling during pregnancy, *Proc Natl Acad Sci U S A* 109(32) (2012) 12878-83.
- [7] P.J. Campagnola, L.M. Loew, Second-harmonic imaging microscopy for visualizing biomolecular arrays in cells, tissues and organisms, *Nat Biotechnol* 21(11) (2003) 1356-60.
- [8] K.P. Quinn, G.V. Sridharan, R.S. Hayden, D.L. Kaplan, K. Lee, I. Georgakoudi, Quantitative metabolic imaging using endogenous fluorescence to detect stem cell differentiation, *Sci Rep* 3 (2013) 3432.
- [9] D. Pouli, M. Balu, C.A. Alonzo, Z. Liu, K.P. Quinn, F. Rius-Diaz, R.M. Harris, K.M. Kelly, B.J. Tromberg, I. Georgakoudi, Imaging mitochondrial dynamics in human skin reveals depth-dependent hypoxia and malignant potential for diagnosis, *Sci Transl Med* 8(367) (2016) 367ra169.
- [10] Z. Liu, K.P. Quinn, L. Speroni, L. Arendt, C. Kuperwasser, C. Sonnenschein, A.M. Soto, I. Georgakoudi, Rapid three-dimensional quantification of voxel-wise collagen fiber orientation, *Biomed Opt Express* 6(7) (2015) 2294-310.
- [11] Z. Liu, D. Pouli, D. Sood, A. Sundarakrishnan, C.K. Hui Mingalone, L.M. Arendt, C. Alonzo, K.P. Quinn, C. Kuperwasser, L. Zeng, T. Schnelldorfer, D.L. Kaplan, I. Georgakoudi, Automated quantification of three-dimensional organization of fiber-like structures in biological tissues, *Biomaterials* 116 (2017) 34-47.

NIR SKULL OPTICAL CLEARING WINDOW FOR IN VIVO CORTICAL VASCULATURE IMAGING AND TARGETED MANIPULATION

DONG-YU LI^{1,2,3}, ZHENG ZHENG⁴, TING-TING YU^{1,3}, BEN ZHONG TANG⁴, PENG FEI⁵, JUN QIAN² AND DAN ZHU^{1,3}

¹Britton Chance Center for Biomedical Photonics, Wuhan National Laboratory for Optoelectronics, Huazhong University of Science and Technology, China

²State Key Laboratory of Modern Optical Instrumentation, Centre for Optical and Electromagnetic Research, College of Optical Science and Engineering, Zhejiang University, China

³MoE Key Laboratory for Biomedical Photonics, Huazhong University of Science and Technology, China

⁴Department of Chemistry, Hong Kong Branch of Chinese National Engineering Research Center for Tissue Restoration and Reconstruction Division of Life Science, State Key Laboratory of Molecular Neuroscience, Institute for Advanced Study, Institute of Molecular Functional Materials, Division of Biomedical Engineering, The Hong Kong University of Science and Technology, China

⁵School of Optical and Electronic Information-Wuhan National Laboratory for Optoelectronics, Huazhong University of Science and Technology, China

dawnzh@mail.hust.edu.cn

Abstract

In vivo observation of brain in its natural environment is of vital significance to better understand the function of vasculature and neural networks, as well as various diseases related to the dysfunction of brain [1-3]. Modern optical imaging technology combined with a variety of fluorescent labelling technology can obtain the structure and function information of biological tissue with high spatial and temporal resolution, providing an important means for brain science [4-6]. However, the high scattering characteristic of skull limits the penetration depth of light [7, 8]. Since the scattering of tissue decreases with the increase of wavelength [9], the imaging in near infrared band, especially in the second region of near infrared, shows great advantages for improving the ability of optical imaging in deep tissue imaging [10-16]. Compared to two-photon fluorescence or second harmonic generation, three-photon fluorescence or third harmonic generation (THG) based on longer wavelength excitation, can obtain deeper information with high resolution.

The recent development of tissue optical clearing technology reduces the effect of scattering from another perspective, providing a new idea for deep tissue imaging. With the novel skull optical clearing window, optical imaging techniques, laser speckle contrast imaging, hyperspectral imaging and two-photon fluorescence microscopy have been applied to observe cortical neuron, microglia, vascular structures and functions [17-21]. Since NIR-II excitation based nonlinear optical microscopy and skull optical clearing are useful means, respectively, to realize *in vivo* cortical imaging without craniotomy, does the combination of the both have an enhancement effect? After all, the previous optical clearing windows only demonstrated the efficacy of optical imaging in the wavelength range of visible to NIR-I [17, 18].

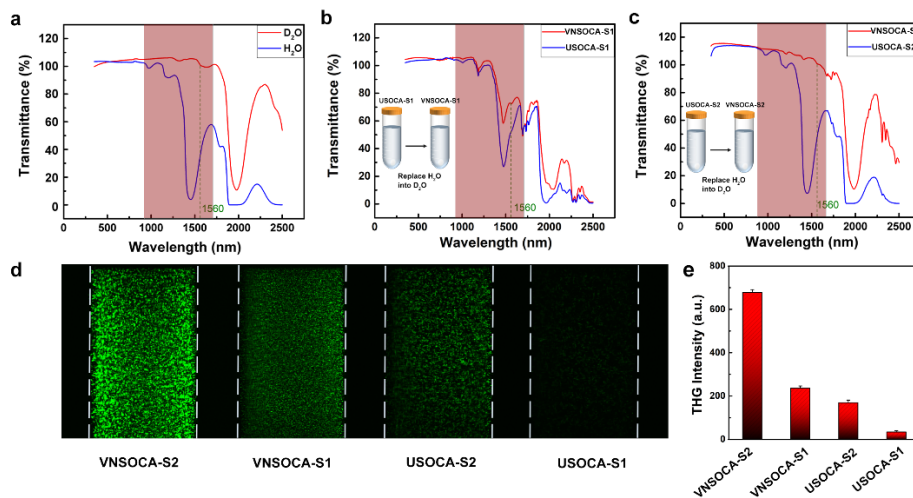


Figure 1. (a) Transmission spectra of D₂O (red line) and H₂O (blue line). (b) Transmission spectra of S1 of VNSOCA (red line) and USOCA (blue line). (c) Transmission spectra of S2 of VNSOCA (red line) and USOCA (blue line). (d) THG images of glass capillaries filled with DCCN nanocrystal dispersion with the 25× objective immersed in S1 and S2 of VNSOCA and USOCA respectively. The dashed lines represent the edges of the capillaries. (e) The THG intensities of DCCN nanocrystal dispersion filled in capillaries with the objective immersed in S1 and S2 of VNSOCA and USOCA respectively.

In this work, we systematically studied the combination of NIR-II excited THG microscopy and *in vivo* tissue optical clearing technique, and further developed Vis-NIR-II compatible optical clearing window. Compared with the previous urea-based skull optical clearing agent (USOCA), the newly developed vis-NIR-II optical clearing agent (VNSOCA) not only had the same transmittance in the shorter wavelength range, but also had greatly enhanced transmittance in the near infrared region (Fig. 1).

The optical clearing window could remarkably increase signal intensity as well as the imaging depth of cortical THG vascular imaging (Fig. 2 and Fig. 3). Finally, the imaging depth of 650 μm was obtained (Fig. 4), which was even close to it without skull [22].

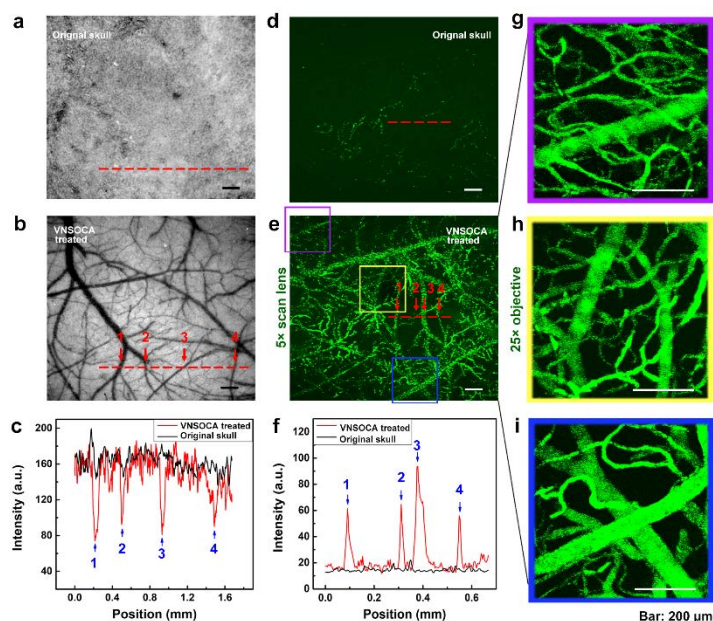


Figure 2. (a, b) Typical white-field images of cortical blood vessels before and after VNSOCA treated. (c) Intensity profiles along the red dashed lines across the vasculature in (a): black, and (b): red. The arrows indicate vessels those couldn't be observed before VSOCA treated. (d,e) Typical large-field THG images collected with a 5 \times scan lens before and after skull clearing. (f) Intensity profiles along the red dashed lines across the vasculature in (d): black, and (e): red. The arrows indicate vessels those couldn't be observed before VSOCA treated. (g-i) THG microscopic images of various areas in (e), using a 25 \times objective. The frame color was used to represent the congruent relationship.

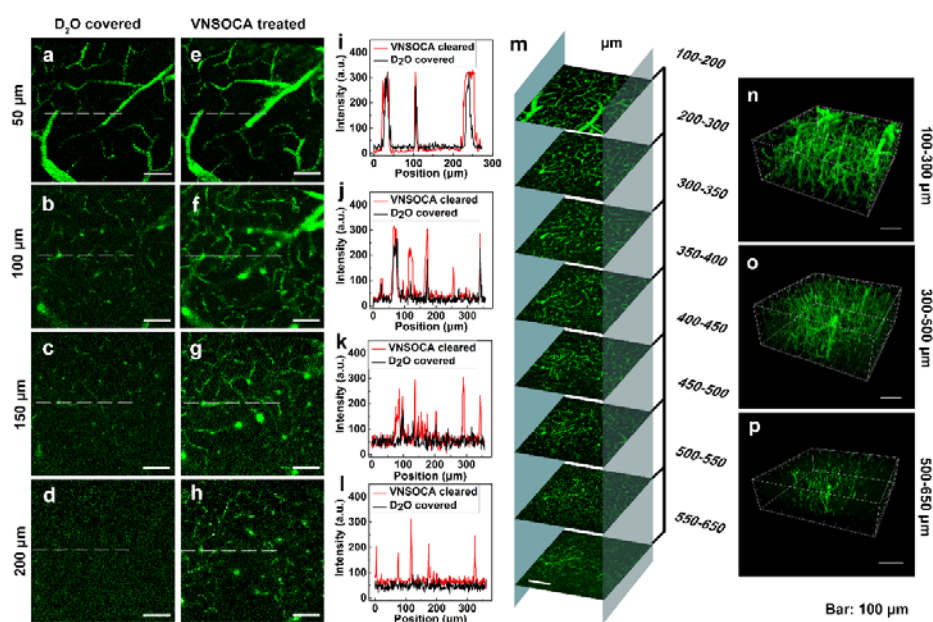


Figure 3. (a-d) THG scanning microscopy at different depth using the 25 \times objective without skull clearing. (e-h) THG scanning microscopy at different depth using the 25 \times objective with skull clearing. (i-l) Intensity profiles along the white dashed lines across the vasculature in (a-h), respectively. (m) THG imaging of cortical vasculature at particular imaging depths. (n-p) 3D reconstruction of vasculature in certain volumes.

In addition of imaging, the effectiveness of optical manipulation is also significant. The results showed that precise NIR-II light manipulation could be performed through the established skull optical clearing window. Using the 1550-nm fs laser, both large vessel or small capillary could be targeted injured (Fig. 4).

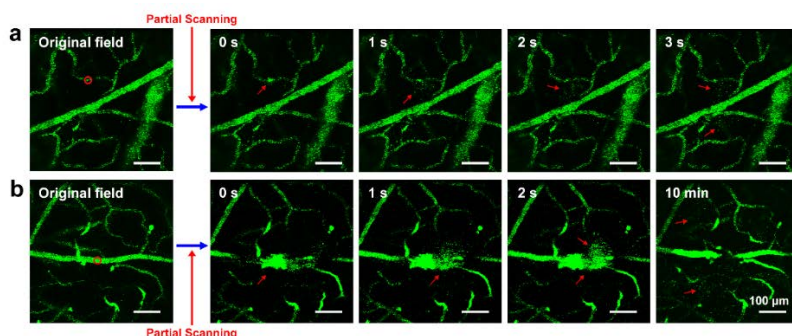


Figure 4. Dynamically observing cerebral hemorrhage using THG scanning imaging. The cerebral hemorrhage was made by partially scanning the region showed by the red circles for (a) 10 s and (b) 15 s.

The novel Vis-NIR-II optical clearing skull window is well adapted to the whole band from visible light to NIR-II region, which greatly expands the wavelength selection range of deep cortex optical imaging and can effectively combine various NIR-II imaging technologies developed in recent years. The first established scalp-cranial window model further simplifies the cranial window model and provides a new approach for imaging the transcranial cortex in vivo.

References

- [1] P. McGonigle, Animal models of CNS disorders, *Biochemical Pharmacology*,87(1), 140-149, 2014.
- [2] M. Wiesmann et al., A specific dietary intervention to restore brain structure and function after ischemic stroke, *Theranostics*,7(2), 493-512, 2017.
- [3] M. Draijer et al., Review of laser speckle contrast techniques for visualizing tissue perfusion, *Lasers in Medical Science*,24(4), 639-651, 2009.
- [4] K. H. Wang et al., In vivo two-photon imaging reveals a role of arc in enhancing orientation specificity in visual cortex, *Cell*,126(2), 389-402, 2006.
- [5] N. Wagner et al., Instantaneous isotropic volumetric imaging of fast biological processes, *Nature Methods*,16(6), 497, 2019.
- [6] R. Prevedel et al., Fast volumetric calcium imaging across multiple cortical layers using sculpted light, *Nature Methods*,13(12), 1021-1028, 2016.
- [7] M. Kneipp et al., Effects of the murine skull in optoacoustic brain microscopy, *Journal of Biophotonics*,9(1-2), 117-123, 2016.
- [8] X. F. Fan, W. T. Zheng, and D. J. Singh, Light scattering and surface plasmons on small spherical particles, *Light-Science & Applications*,3, e179, 2014.
- [9] N. G. Horton et al., In vivo three-photon microscopy of subcortical structures within an intact mouse brain, *Nat Photonics*,7(3), 205-209, 2013.
- [10] J. T. Robinson et al., High Performance In Vivo Near-IR ($> 1 \mu\text{m}$) Imaging and Photothermal Cancer Therapy with Carbon Nanotubes, *Nano Research*,3(11), 779-793, 2010.
- [11] Z. Feng et al., Excretable IR-820 for in vivo NIR-II fluorescence cerebrovascular imaging and photothermal therapy of subcutaneous tumor, *Theranostics*,9(19), 5706-5719, 2019.
- [12] K. Welscher, S. P. Sherlock, and H. J. Dai, Deep-tissue anatomical imaging of mice using carbon nanotube fluorophores in the second near-infrared window, *Proceedings Of the National Academy Of Sciences Of the United States Of America*,108(22), 8943-8948, 2011.
- [13] H. Wan et al., A bright organic NIR-II nanofluorophore for three-dimensional imaging into biological tissues, *Nature Communications*,9, 1171, 2018.
- [14] M. X. Zhang et al., Bright quantum dots emitting at similar to 1,600 nm in the NIR-IIb window for deep tissue fluorescence imaging, *Proceedings of the National Academy of Sciences of the United States of America*,115(26), 6590-6595, 2018.
- [15] W. Yu et al., NIR-II fluorescence in vivo confocal microscopy with aggregation-induced emission dots, *Science Bulletin*,64(6), 410-416, 2019.
- [16] J. Qi et al., Real-Time and High-Resolution Bioimaging with Bright Aggregation-Induced Emission Dots in Short-Wave Infrared Region, *Advanced Materials*,30(12), 1706856, 2018.
- [17] Y. J. Zhao et al., Skull optical clearing window for in vivo imaging of the mouse cortex at synaptic resolution, *Light-Science & Applications*,7(2), 17153, 2018.
- [18] C. Zhang et al., A large, switchable optical clearing skull window for cerebrovascular imaging, *Theranostics*,8(10), 2696-2708, 2018.
- [19] C. Zhang et al., Photodynamic opening of the blood-brain barrier to high weight molecules and liposomes through an optical clearing skull window, *Biomedical Optics Express*,9(10), 4850-4862, 2018.
- [20] C. Zhang et al., Age differences in photodynamic therapy-mediated opening of the blood-brain barrier through the optical clearing skull window in mice, *Lasers in Surgery and Medicine*,51(7), 625-633, 2019.
- [21] W. Feng et al., Comparison of cerebral and cutaneous microvascular dysfunction with the development of type 1 diabetes *Theranostics*,9(20), 5854-5868, 2019.
- [22] Z. Zheng et al., Aggregation-induced nonlinear optical effects of AIEgen nanocrystals for ultradeep *in vivo* bioimaging, *advanced materials*,31(34), 1904799, 2019.

IN VIVO RAMAN SPECTROSCOPY FOR CHRONIC DISEASES DETECTION

IVAN BRATCHENKO¹, LYUDMILA BRATCHENKO¹, YULIA KHRISTOFOROVA¹, DMITRY ARTEMYEV¹,
OLEG MYAKININ¹, ALEXANDER MORYATOV², SERGEY KOZLOV², PETER LEBEDEV³ AND
VALERY ZAKHAROV¹

¹Department of Laser and Biotechnical Systems, Samara University, Russia

²Department of Oncology, Samara State Medical University, Russia

³Department of Internal Medicine, Samara State Medical University, Russia

iabratchenko@gmail.com

Abstract

In this study we performed *in vivo* diagnosis of skin cancer and kidney failure based on the estimation of biochemical changes in skin tissues employing a portable spectroscopy setup combining analysis of Raman and autofluorescence spectra in the near infrared region [1]. We studied 617 cases of skin cancer (70 melanomas, 122 basal cell carcinomas, 12 squamous cell carcinomas and 413 benign tumors) and 90 adult patients with kidney failure (90 spectra) and 40 healthy adult volunteers (80 spectra) *in vivo* with a portable setup. The studies considered the patients examined by GPs in local clinics and directed to specialized clinics with suspected skin cancer and kidney failure patients that undergo hemodialysis. The spectra were classified with a projection on latent structures and discriminant analysis (PLS-DA) [2]. To check the classification models stability, a 10-fold cross-validation was performed. We obtained ROC AUCs of 0.75 (0.71 – 0.79; 95% CI), 0.69 (0.63-0.76; 95% CI), and 0.81 (0.74 – 0.87; 95% CI) for classification of a) malignant and benign tumors, b) melanomas and pigmented tumors and c) melanomas and seborrheic keratosis respectively. The positive and negative predictive values ranged from 20% to 52% and from 73% to 99% respectively. The biopsy ratio varied from 0.92:1 to 4.08:1 (at sensitivity levels from 90% to 99%). Application of Raman spectroscopy to investigate the forearm skin in patients with kidney failure and healthy adult volunteers has yielded the accuracy of 0.96, sensitivity of 0.94 and specificity of 0.99 in terms of identifying the target subjects with kidney failure. The autofluorescence analysis in the near infrared region identified patients with kidney failure among healthy volunteers of the same age group with specificity, sensitivity, and accuracy of 0.91, 0.84, and 0.88, respectively. The most informative Raman spectral bands when classifying subjects by the presence of kidney failure using the PLS-DA method are 1315-1330 cm^{-1} , 1450-1460 cm^{-1} , 1700-1800 cm^{-1} . Figure 1 demonstrates variable importance in the projection (VIP) for discrimination of kidney failure. VIP makes it possible to assess the impact of individual variables of the predicate matrix array on the model [3].

In general, the performed study demonstrates that for *in vivo* skin analysis, the conventional Raman spectroscopy can provide the basis for cost-effective and accurate detection of kidney failure and associated metabolic changes in the skin. The accuracy of automatic analysis with the proposed portable system is higher than the accuracy of GPs and trainees, and is comparable to the accuracy of trained dermatologists. The proposed approach may be combined with other optical techniques of skin lesion analysis, such as dermoscopy- and spectroscopy-based computer-assisted diagnosis systems to increase accuracy of neoplasms classification.

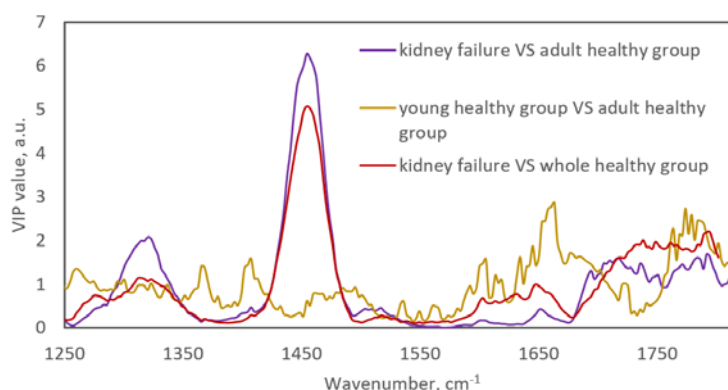


Figure 1. VIP-scores of the Raman spectra matrices for the constructed PLS-DA models

References

- [1] Y.A. Khristoforova, I.A. Bratchenko, O.O. Myakinin, et al., Portable spectroscopic system for *in vivo* skin neoplasms diagnostics by Raman and autofluorescence analysis. J Biophotonics. 12,e201800400, 2019.
- [2] D.M. Haaland, E.V. Thomas, Partial least-squares methods for spectral analyses. 1. Relation to other quantitative calibration methods and the extraction of qualitative information. Anal Chem. 60, 1193–1202, 1988.
- [3] I.G. Chong, C.H. Jun, Performance of some variable selection methods when multicollinearity is present. Chemometr Intell Lab Syst. 78, 103–112, 2005.

PROGRESS ON STIMULATED EMISSION DEPLETION MICROSCOPY

JUNLE QU, WEI YAN, ZHIGANG YANG, LUWEI WANG, JIA ZHANG AND JIALIN WANG

Center for Biomedical Optics and Photonics (CBOP)
College of Physics and Optoelectronic Engineering
Shenzhen University

jlqu@szu.edu.cn

Abstract

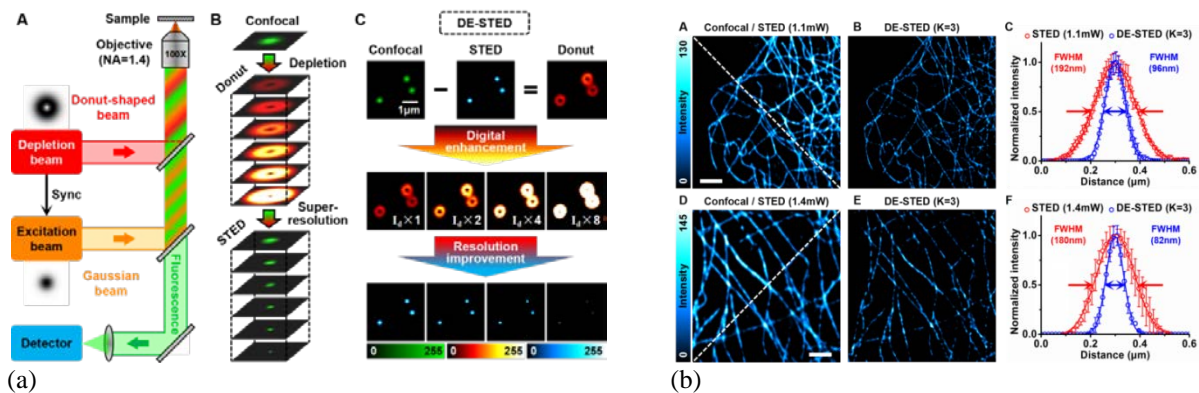
Stimulated emission depletion (STED) microscopy, as an advanced imaging technique, was theoretically proposed in 1994 and experimentally performed later. In principle, two laser beams are needed to carry out super resolution imaging using STED method. One pulsed laser beam is used to transfer fluorescent dyes to the excited states, generating a fluorescent spot owing to optical diffraction; and the second one (STED laser) with larger pulse width, actually producing a doughnut-shape spot, is employed to selectively deactivate the fluorescent dyes lying in the overlapping region of excitation and STED laser spots. Typically, the doughnut-shaped STED beam selectively suppresses fluorescence photon emission in the periphery of the excitation beam to preferably ensure almost zero-intensity at the center. Undoubtedly, in STED, the depletion laser power is an important factor to determine the imaging resolution.

In this advanced optical microscopic technique, especially for the biological samples, selecting apposite fluorescent dyes with excellent nonlinear response is another determining factor to achieving better spatial resolution. Basically, all the fluorophores around the focal excitation spot need to be in their fluorescent 'off' state to attain an exceptionally high resolution, since the stimulated emission rate has a non-linear dependence on the intensity of the STED beam. To retrieve the high resolution images, the focal spot is then scanned across the object. Theoretically, the full-width-at-half maximum (FWHM) of the PSF at the excitation focal spot can be compressed by increasing the intensity of the STED pulses as presented in equation (1).

$$\Delta r = \frac{\Delta}{\sqrt{1+I_{\max}/I_s}}, \quad (1)$$

where, Δr is the lateral resolution, Δ represents the FWHM of the diffraction limited PSF, I_{\max} is the peak intensity of the STED laser, and I_s stands for the threshold intensity needed in order to achieve saturated emission depletion.

The STED microscopy can provide a lateral resolution of 10-80 nm and a longitudinal resolution of 30-600 nm with high imaging speed. These abilities of the STED microscopy stimulated its increasing contribution in visualizing and understanding many complex biological structures and dynamic functions in a plethora of cell and tissue types at nanoscale level. However, for live cell STED imaging, the use of intense laser could be detrimental as it can cause severe photodamage to the live cells, tissues and even the used fluorophores. Moreover, use of intense STED laser beam is likely to accelerate the photobleaching process of fluorophores which may impede the long-term STED imaging. Therefore, optimizing the STED laser power is crucial to achieve a successful good quality STED image.



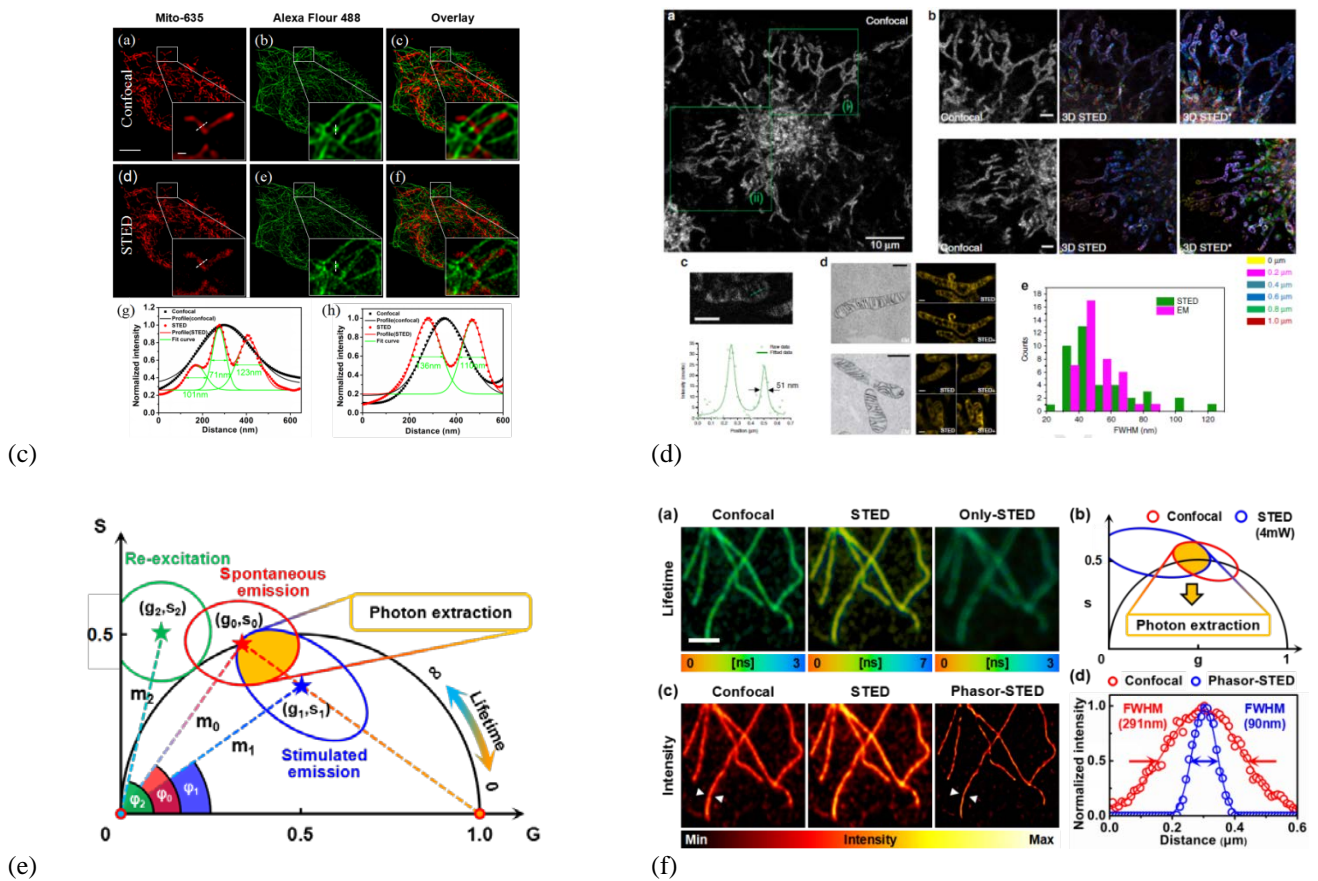


Figure 1. (a) Principle of DE-STED. (b) DE-STED imaging of microtubules in fixed BSC-1 cells. (c) Dual color STED imaging of cells with a single super-continuum laser. (d) STED imaging of mitochondrial dynamics with an enhanced squaraine variant probe. (e) Working principle of accurate photon extraction in the phasor plot. (f) Re-excitation eliminating STED imaging in a biological cell

In this talk I will present our recent work in STED microscopy. We proposed two major strategies to achieve successful STED imaging with reduced STED laser power. The first method relies on the development of novel STED imaging techniques such as adaptive optics STED [1, 2], phasor analysis STED [3, 4] and digitally enhanced STED [5] to lower the depletion power during the acquisition of STED images. The other significant method to minimize the STED laser power basically relies upon the development of new dedicated STED probes/fluorophores with better photostability and lower saturation intensity (I_s). We developed perovskite quantum dots [6], carbon dots [7] organosilicon nanohybrids [8] and enhanced squaraine variant probe [9] for STED imaging with very low STED laser power. Typically, these new fluorescent materials contain superior photostability and much lower saturation intensity (I_s) compared to the traditional STED probes. In addition, a dual-color STED microscope with a single laser source is developed, and the spatial resolutions of 75 nm and 104 nm have been achieved for mitochondria and tubulin in HeLa cells [10].

References

- [1] W. Yan, Y. Yang, Y. Tan, X. Chen, Y. Li, J. Qu, T. Ye, Coherent optical adaptive technique improves the spatial resolution of STED microscopy in thick samples, *Photonics Res.*, 5:176-181, 2017.
- [2] L. Wang, W. Yan, R. Li, X. Weng, J. Zhang, Z. Yang, L. Liu, J. Qu, Aberration correction for improving the image quality in STED microscopy using the genetic Algorithm, *Nanophotonics*, 7:1971-1980, 2018.
- [3] L. Wang, B. Chen, W. Yan, Z. Yang, X. Peng, D. Lin, X. Weng, T. Ye, J. Qu, Resolution improvement in STED super-resolution microscopy at low power using a phasor plot approach, *Nanoscale*, 10:16252-16260, 2018.
- [4] Y. Chen, L. Wang, W. Yan, X. Peng, J. Qu, J. Song, Elimination of Re-excitation in Stimulated Emission Depletion Nanoscopy Based on Photon Extraction in a Phasor Plot, *Laser Photonics Rev.*, 14: 1900352, 2020.
- [5] L. Wang, Y. Chen, X. Peng, J. Zhang, J. Wang, L. Liu, Z. Yang, W. Yan, J. Qu, Ultralow power demand in fluorescence nanoscopy with digitally enhanced stimulated emission depletion, *Nanophotonics*, DOI: 10.1515/nanoph-2019-0475.
- [6] S. Ye, W. Yan, M. Zhao, X. Peng, J. Song, J. Qu, Low-Saturation-Intensity, High-Photostability, and High-Resolution STED Nanoscopy Assisted by CsPbBr₃ Quantum Dots, *Adv. Mater.*, 30:201800167, 2018.
- [7] H. Li, S. Ye, J. Guo, H. Wang, W. Yan, J. Song, J. Qu, Biocompatible carbon dots with low-saturation-intensity and high photobleaching-resistance for STED nanoscopy imaging of the nucleolus and tunneling nanotubes in living cells, *Nano Research*, 12: 3075-3084, 2019.

- [8] L. Liang, W. Yan, X. Qin, X. Peng, H. Feng, Y. Wang, Z. Zhu, L. Liu, Y. Han, Q. Xu, J. Qu, X. Liu, Designing Sub-2 nm Organosilica Nanohybrids for Far-Field Super-Resolution Imaging, *Angew. Chem.*, 7: 746-751, 2020.
- [9] X. Yang, Z. Yang, Z. Wu, Y. He, C. Shan, P. Chai, C. Ma, M. Tian, J. Teng, D. Jin, W. Yan, P. Das, J. Qu, P. Xi, Mitochondrial dynamics quantitatively revealed by STED nanoscopy with an enhanced squaraine variant probe, *Nature Communications*, 11, 1:1-9, 2020.
- [10] J. Wang, J. Zhang, L. Wang, X. Gao, Y. Shao, L. Liu, Z. Yang, W. Yan, J. Qu, Dual-color STED super-resolution microscope using a single laser source, *J. Biophotonics*, 13: e202000057, 2020.

OPTICAL TECHNIQUES FOR ASSESSING BLOOD MICRORHEOLOGY: RED BLOOD CELLS DEFORMABILITY, AGGREGATION AND THEIR INTERRELATION

ANDREI LUGOVTSOV^{1,2}, ANASTASIA MASLYANITSINA¹, PETR ERMOLINSKIY¹ AND ALEXANDER PRIEZZHEV^{1,2}

¹Physics Department, Lomonosov Moscow State University, Russia

²International Laser Center, Lomonosov Moscow State University, Russia

anlug@biomedphotonics.ru

Abstract

The state of human organism largely depends on blood microcirculation that, in turn, depends on the microrheologic properties of red blood cells (RBCs), in particular, the RBC intrinsic properties of deformability and aggregation that are supposed to be interdependent [1]. The RBCs have the ability to reversibly deform in the blood flow. Usually they elongate in the direction of the flow but, also, they can change their shape dramatically in the vessels that are smaller than the size of the RBCs, for example, capillaries with diameters from 3 to 5 μm [2]. A considerable contribution to the deformability comes from the elasticity of the cell membrane, as well as from the viscosity of hemoglobin solution inside the cell [3]. RBC deformability plays a significant role in the blood circulation. In particular, RBC filtering in narrow circulatory pathways in the human spleen is based on their impaired deformability. Another important process that influences the blood flow is the aggregation of RBCs [4]. It is a reversible process of formation of linear and more complex structures of RBCs. The aggregation happens predominantly inside large vessels. However, the aggregates can become quite large, and if not their ability to disaggregate to single cells due to shear stress, the blood flow would be impaired.

Socially significant diseases such as arterial hypertension, diabetes mellitus and others are associated with serious changes in the RBC deformability [4-6]. At the same time a significant change in the aggregation parameters may happen [4]. For example, RBC aggregates in the blood of patients suffering from arterial hypertension are stronger and form faster than in the blood of healthy people [6]. Moreover, these pathologies are accompanied by an alteration in the number of RBC involved in the process of spontaneous aggregation. This can be caused by many reasons: a change in the protein composition of plasma, cell membrane changes, different rigidity and age of the cells, as well as the average patient age and their medication, etc. [4].

The aim of this work is to identify the relationship between the deformability of RBCs and their aggregation properties, both of which are the key factors for the blood flow. Laser diffractometry, diffuse light scattering and laser tweezers were implemented for *in vitro* measurements.

Laser diffractometry performed with the RheoScan diffractometer (RheoMeditech, Korea) was used to obtain the shear induced deformation parameters of RBCs by processing the light intensity distribution in the diffraction pattern [7]. This pattern is based on diffraction of a laser beam on a highly diluted RBC suspension in a flow channel *in vitro*. The dimensions of the channel are 0.2 mm high \times 4.0 mm wide \times 40 mm long. We measured the RBC deformability index (DI) that describes the average elongation of the cells by shear stress. The elongation of the cells corresponds to the elongation of the diffraction pattern. Different shear stresses from 20 Pa to 0.5 Pa were applied to the RBC suspension in order to change the shear stress and, consequently, the elongation of the cells.

Laser aggregometry was performed using the RheoScan aggregometer (RheoMeditech, Korea) [8]. It is based on diffuse light scattering and is applied to whole blood samples in order to retrieve a number of the RBC aggregation properties. By analyzing the scattered light intensity as a function of time during the process of RBC spontaneous aggregation we can evaluate the aggregation index (AI), which characterizes the relative number of aggregated cells during the first 10 sec of the aggregation process [14]. Besides that, the critical shear stress (CSS) that characterizes the balance of aggregation and disaggregation processes was measured. In order to do it, the blood flow conditions were created *in vitro* with varying shear stress, and the light scattered backwards was analyzed.

Different osmolarities of plasma (150–500 mOsm/l) and concentrations of glutaraldehyde (GA) (up to 0.004%) were used to change the deformability of the RBCs *in vitro*. The measurements were performed at 37 °C. The study was conducted on the blood of 2 healthy donors. The values of AI, DI and the forces of RBC interaction were measured 5 times for the same sample. The results were then averaged and the standard deviations from the mean values were calculated.

The RBC deformability changes are presented in the Fig. 1. The results in the Fig. 1a show a decrease in the DI with the increase of GA concentration. Secondly, in a separate experiment, the osmolarity of the suspension was also shown to influence RBC deformability as seen in Fig. 1b.

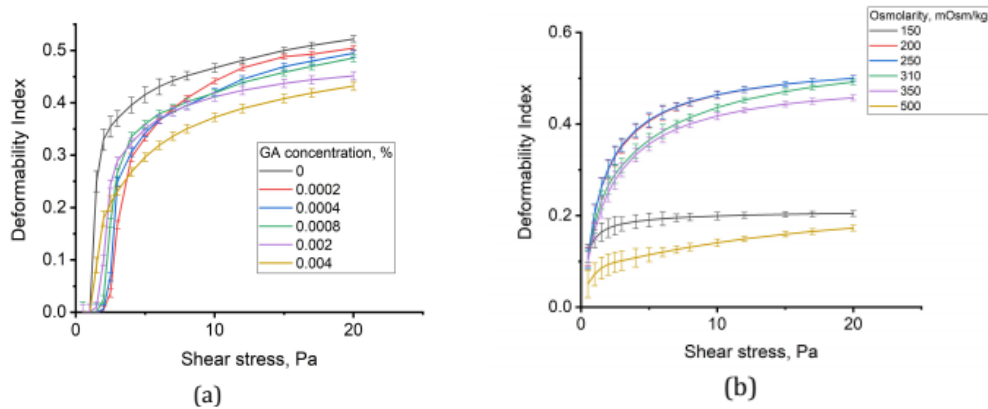


Figure 1: The deformability index as a function of the shear stress (a) at different glutaraldehyde concentrations and (b) at different osmolarities.

The results obtained by laser aggregometry for the samples treated with GA are shown in Fig. 2a. The AI significantly drops for samples with low DI, which corresponds to high GA concentration. Namely, the control measurement (0% GA) yields DI equal to 0.522 ± 0.006 and AI equal to $39 \pm 4\%$. For 0.004% GA concentration DI decreases to 0.426 ± 0.006 and AI decreases to $9 \pm 3\%$. This means that at high GA concentrations the process of spontaneous aggregation almost stops. For the samples suspended in plasma at different osmolarities the laser aggregometry method shows similar results (Fig. 2b). Lower deformability corresponds to smaller AI.

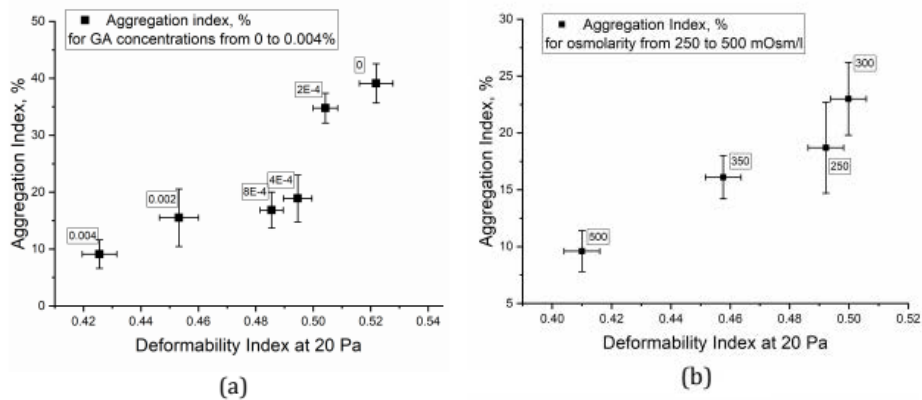


Figure 2: The aggregation index as functions of the deformability index for different glutaraldehyde concentrations (a) and osmolarities (b).

The method of laser diffractometry confirmed that with the addition of glutaraldehyde and with a large change in the osmolarity of the solution, RBCs become more rigid. Secondly, the methods of laser aggregometry and laser tweezers gave consistent results: with the decreased ability of RBCs to deform the formation of aggregates becomes impaired. However, the critical shear stress and the disaggregation force measured with laser tweezers remain mostly unchanged. This means that the RBC aggregate formation is dependent on the deformability of the membrane, while the connection to disaggregation is less pronounced and more complicated in nature.

Acknowledgement: This work was supported by the Russian Foundation for Basic Research grant #19-52-51015.

References

- [1] V. Leftov, S. Regirer, and N. Shadrina, Blood Rheology, Meditsina, Moscow, 1982 [in Russian].
- [2] V. V. Tuchin (Ed.), Handbook of Optical Biomedical Diagnostics, Vol. 1. Chapter 2, Optics of Blood, SPIE Press, Bellingham, Washington, USA, 2016.
- [3] N. Firsov, A. Priezhev, N. Klimova, and A. Tyurina, Fundamental laws of the deformational behavior of erythrocytes in shear flow, J. of Engineering Physics and Thermophysics 79(1), 118–124, 2006.
- [4] O. Baskurt, B. Neu, and H. Meiselman, Red Blood Cell Aggregation, CRC Press, 2012.
- [5] A. Lugovtsov, Y. I. Gurfinkel, P. B. Ermolinskiy, A. I. Maslyanitsina, L. I. Dyachuk, and A. V. Priezhev, Optical assessment of alterations of microrheologic and microcirculation parameters in cardiovascular diseases, Biomedical Optics Express 10(8), 3974–3986, 2019.
- [6] P. Ermolinskiy, A. Lugovtsov, A. Maslyanitsina, A. Semenov, L. Dyachuk, and A. Priezhev, Interaction of erythrocytes in the process of pair aggregation in blood samples from patients with arterial hypertension and healthy donors: measurements with laser tweezers, Journal of Biomedical Photonics & Engineering 4(3), 030303, 2018.
- [7] S. Shin, J. Hou, J. Suh, and M. Singh, Validation and application of a microfluidic ektacytometer (RheoScan-D) in measuring erythrocyte deformability, Clinical Hemorheology and Microcirculation 37(4), 319–28, 2007.
- [8] S. Shin, Y. Yang, and J. Suh, Measurement of erythrocyte aggregation in a microchip stirring system by light transmission, Clinical Hemorheology and Microcirculation 41(3), 197–207, 2009.

MULTIPARAMETER OPTICAL DIAGNOSTICS OF MICROCIRCULATORY-TISSUE SYSTEMS:METHODS AND TECHNICAL MEANS

ANDREY DUNAEV

Research and Development Center of Biomedical Photonics, Orel State University named after I.S. Turgenyev, Russia

dunaev@bmecenter.ru

Abstract

In the last decade, there has been a steady increase in the interest of researchers in the problems of non-invasive research of microcirculatory-tissue systems (MTS). This is due to the essential role of blood microcirculation in the pathogenesis of various diseases (in particular, diseases of the rheumatological and endocrinological profiles). A modern trend in the development of optical biomedical diagnostics is a multiparametric approach when various optical (and sometimes additionally other) research methods are combined in one diagnostic technology. This allows one to obtain highly efficient diagnostic tools for rheumatology, endocrinology, surgery, oncology, neurology, and other areas of medicine, where it is necessary to determine the parameters of the perfusion-metabolic status of tissues.

The aim of this work was to scientifically substantiate and develop a methodology for multiparametric optical non-invasive diagnostics (mOND) to assess the functional state of the microcirculatory-tissue systems of the human body with the development of metrological support of methods and technical means that contribute to improving the quality of optical non-invasive diagnostics and its wider implementation in clinical practice.

To solve the research problems, a systematic approach was used to develop a methodology for the synthesis of mOND for assessing the functional state of MTS in various diseases. A method for assessing angiospastic and microcirculatory [1] disorders in rheumatic diseases and a method for assessing microcirculatory-metabolic disorders in MTS of the lower extremities in diabetes mellitus [2] were developed. Also in this work, methods were developed for assessing the state of the MTS of the human body under various conditions, such as sports and physiological stresses [3], the provision of physiotherapeutic effects, during minimally invasive surgical interventions [4]. The developed methods are based on the combined application of several widely used methods of optical non-invasive diagnostics, such as laser Doppler flowmetry(LDF), diffuse reflection spectroscopy (DRS), fluorescence spectroscopy (FS), etc.The scheme for implementing the multiparametric optical measurements is shown in the Fig. 1a.The block diagram of one of the variants of the device for assessing the functional state of the MTS of the human body on the basis of multiparametric optical diagnostics using 3 methods of OND (LDF, FS and DRS) is shown in the Fig. 1b.

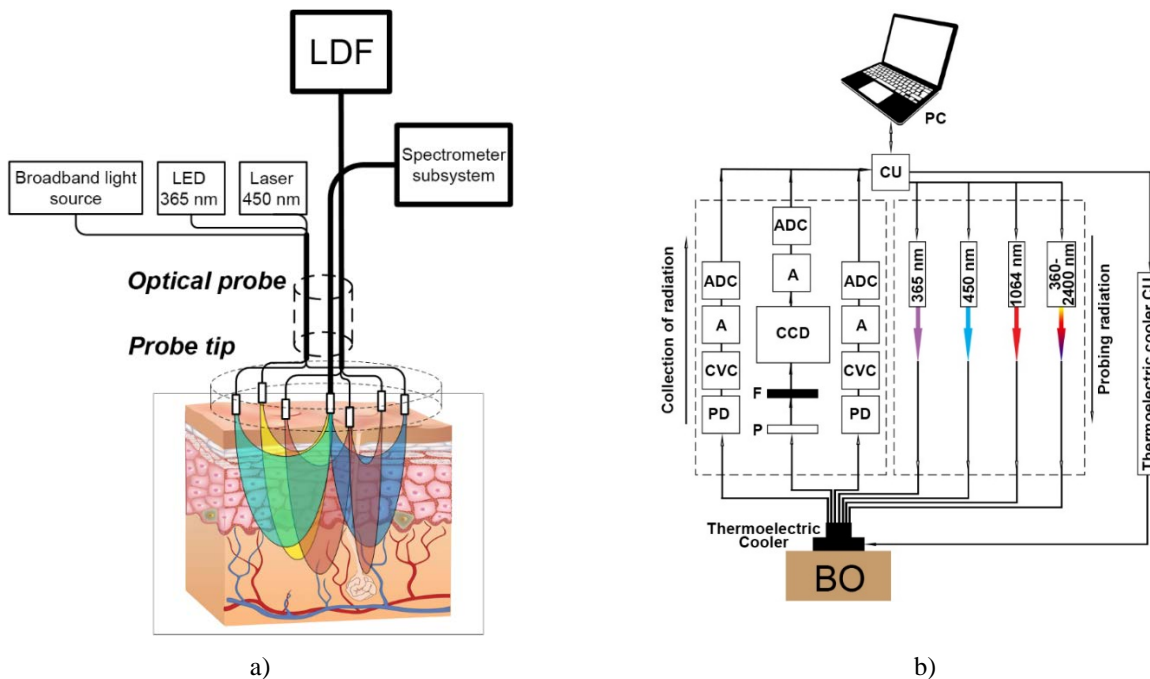


Figure 1: The scheme for implementing the multiparametric optical measurements (a) and the block diagram of the device for assessing the functional state of the MTS (b).

The LDF optical-electronic system is made in the form of two identical channels for recording the Doppler signal and includes a laser radiation source with a wavelength of 1064 nm connected to a driver that sets the power supply, and an optical-electronic system for recording secondary optical radiation, consisting of photodiodes (PD) with optical filters, connected in pairs with the Doppler signal forming unit, consisting of current-to-voltage converters (CVC), signal amplifiers (A) and analog-to-digital converters (ADC). Each channel has a sequential signal conversion.

The FS and DRS channels include sources of fluorescence excitation with wavelengths of 365 and 450 nm, connected to drivers that set the power supply, and a broadband radiation source, a polychromator (P), a set of replaceable light filters (F), and a CCD radiation detector. The polychromator is built according to the Czerny-Turner scheme with a flat diffraction grating.

The channels are controlled by a common control unit (CU), which is an PLD with a binding connected through an interface with a personal computer (PC). The CU controls the operation of the emitters (supplying control signals to their drivers) and turning on the broadband radiation source. Laser emitters with wavelengths of 450 and 1064 nm, a light-emitting diode with a wavelength of 365 nm and a broadband radiation source with a wavelength range of 360 ... 2400 nm are used as sources of primary optical radiation. The light from these sources is transmitted through a fiber bundle to the area of study of the biological object (BO). Fluorescence, diffuse reflectance, and Doppler signals are received by closely spaced receiving fibers. If it is necessary to conduct temperature tests through the CU, an additional temperature exposure channel is connected, built on a thermoelectric cooler with its own control unit, which allows one to change the polarity of the supply voltage. This channel is used to carry out a functional temperature tests in the range of 5-42 °C.

The user communicates with the control unit through a specialized program installed on the PC.

Approbation of the developed methods was carried out on the basis of 3 Departments of the Orel Regional Clinical Hospital (Orel, Russia). The reliability of the results obtained has been confirmed by numerous clinical observations of more than 200 patients.

The results of the work can be extended to other areas of medicine, for example, in the direction of improving methods of optical biopsy in minimally invasive surgery, rheumatology, endocrinology, otolaryngology, dermatology, neurology and other areas of medicine. The introduction of mOND into wearable devices (fitness bracelets, gadgets) for long-term monitoring (daily or during sleep, tracking of circadian biorhythms) and monitoring in vivo (and not only in a hospital) also has great diagnostic potential.

The study was supported by the Russian Science Foundation (the project №18-15-00201), Russian Foundation for Basic Research (the project 18-02-00669) and by the grant of the Russian Federation Government (the project №075-15-2019-1877).

References

- [1] A.I. Zherebtsova, V.V. Dremmin, I.N. Makovik, E.A. Zherebtsov, A.V. Dunaev, A.Goltsov, S.G. Sokolovski, E.U. Rafailov, Multimodal optical diagnostics of the microhaemodynamics in upper and lower limbs, *Front. Physiol.* 10, 416, 2019.
- [2] V. Dremmin, E. Zherebtsov, V. Sidorov, A. Krupatkin, I. Makovik, A. Zherebtsova, E. Zharkikh, E. Potapova, A. Dunaev, A. Doronin, A. Bykov, I. Rafailov, K. Litvinova, S. Sokolovski, E. Rafailov, Multimodal optical measurement for study of lower limb tissue viability in patients with diabetesmellitus, *J. Biomed. Opt.* 22(8), 085003, 2017.
- [3] A.V. Dunaev, V.V. Sidorov, A.I. Krupatkin, I.E. Rafailov, S.G. Palmer, N.A. Stewart, S.G. Sokolovski, E.U. Rafailov, Investigating tissue respiration and skin microhaemocirculation under adaptive changes and the synchronization of blood flow and oxygen saturation rhythms, *Physiol. Meas.* 35(4), 607, 2014.
- [4] V. Dremmin, E. Potapova, E. Zherebtsov, K. Kandurova, V. Shupletsov, A. Alekseyev, A. Mamoshin, A. Dunaev Optical percutaneous needle biopsy of the liver: a pilot animal and clinical study, *Sci. Rep.* 10, 14200, 2020.

**CORRELATION OF HEMORHEOLOGIC PARAMETERS MEASURED *IN VITRO* AND *IN VIVO*
BY DIFFERENT OPTICAL TECHNIQUES IN PATIENTS SUFFERING FROM
VARIOUS SOCIALLY IMPORTANT DISEASES**

ALEXANDER PRIEZZHEV^{1,2}, ANDREI LUGOVTSOV^{1,2}, ANASTASIA MASLYANITSINA¹,
PETR ERMOLINSKIY¹ AND YURI GURFINKEL³

¹*Physics Department, Lomonosov Moscow State University, Russia*

²*International Laser Centre, Lomonosov Moscow State University, Russia*

³*Medical Research-Educational Centre, Lomonosov Moscow State University, Russia*

avp2@mail.ru

Abstract

In this work, *in vivo* and *in vitro* optical methods were used to study the microrheologic properties of red blood cells (RBC) in patients suffering the coronary heart disease (CHD) and comorbidities such as type 2 diabetes mellitus (T2DM). The main focus of our study was the aggregation of RBC, which significantly influences the viscosity of blood [1]. Aggregation is a reversible process of formation of linear and more complex structures of RBC. It promotes the formation of peripheral cell-poor fluid layer that lowers the hydrodynamic vessel resistance to the blood flow [1]. *In vitro* as well as *in vivo*, the process of RBC aggregation can be described in several ways: by the amount of cells aggregating during a given time interval, by how many aggregates are observed, or by how fast a couple of RBCs can form a doublet. These parameters require specialized tools in order to be measured, so they are not used widely in clinical conditions.

Many methods can be applied to study RBC including the micropipette aspiration [2], but optical techniques have several advantages: non-invasiveness and lack of direct mechanical contact with the cells; the option to study both individual cells and their ensembles; the possibility of *in vivo* and *in vitro* application. The last point can pose a challenge in terms of comparing results for these different conditions - *in vitro* measurements require anticoagulants for stabilizing the blood samples and storing blood during sample preparation, which can influence the measured parameters; while *in vivo* methods allow for measuring a different set of parameters that may be difficult to correlate with those measured *in vitro*.

The aim of this work was to find correspondence between *in vivo* and *in vitro* optical methods by studying patients with cardiovascular and associated pathologies. Understanding the link between the RBC aggregation and widespread cardiovascular diseases is vital to create new methods of diagnosis and treatment. The age, state of health and lifestyle of an individual determine in part the aggregation parameters of RBC [3], as does the medicine intake [1,4].

The study enrolled 81 adults, including 25 healthy volunteers and 56 patients with CHD and arterial hypertension. The patients with CHD were divided into two groups depending on the presence of T2DM. First groups included 42 CHD patients without T2DM, second group included 14 CHD patients with T2DM. The healthy volunteers had an average age 27.5 and body mass index (BMI) 22.1, they were non-smokers, and had not been taking any medication. They were divided into two control groups (n = 10 and 15) that were studied independently by two different research teams.

Laser aggregometry method implemented in microchip stirring type RheoScan aggregometer (RheoMedTech, Rep. of Korea) was used to measure the aggregation parameters of RBC *in vitro* in whole blood samples [5]. The measurement technique is based on the diffused light scattering of a laser beam by the blood sample [6]. The RBC aggregation kinetics is reflected in the dependence of scattered light intensity on time and several parameters are calculated based on it. Firstly, $T_{1/2}$ characterizes the time interval, during which the signal (scattered light intensity) reaches half of the maximum value. Smaller $T_{1/2}$ corresponds to greater curve slope and faster aggregation of the cells. Secondly, the aggregation index (AI) characterizes the fraction of cells aggregated during the first 10 seconds of measurement. It is calculated as a ratio between the area under the intensity curve to the total area above and below it. Higher AI values correspond to more numerous RBC aggregates in the sample.

Lasers tweezers were used to measure the duration of the process of spontaneous aggregation of two individual RBCs [7]. The measurements are carried out on a highly diluted blood suspension inside a glass microcuvette with a 100 μm gap [8]. Patients' autologous platelet poor plasma was used as the suspension medium. The time of doublet aggregate formation T_{agg} was measured in real time. Smaller values of T_{agg} correspond to faster aggregate formation. It's worth noting that the T_{agg} parameter corresponds to the initial stage of the RBC aggregation process, while laser aggregometry parameters ($T_{1/2}$ and AI) represent the whole aggregation process, including the later stage of complex 3D structures formation.

Digital capillaroscopy (DC) [9] was used to evaluate the capillary blood flow parameters *in vivo*. Using the device Kapillaroskan-1 (AET, Russia) a quantitative assessment of the blood flow characteristics was carried out in the capillaries of the nail bed. Several nail bed capillaries of each individual were recorded at a high frame rate and then used

to assess the average capillary blood flow velocity (CBV), which was calculated by frame-by-frame analysis. The cases of absence or presence of aggregates in the bloodstream were defined as individual RBC or groups of several RBC separated by empty layers of plasma respectively.

For each blood sample, the parameters AI, $T_{1/2}$ and T_{agg} were measured 5 times. The calculation of the CBV and the detection of aggregates for the DC method was carried out using original software that analyzed recordings of the nail bed capillaries. Videos of at least 6 capillaries were used for calculations with the video duration of 3 to 5 seconds (at a recording rate of 100 frames per second, i.e., from 1800 to 3000 frames per patient).

The parameters assessed with all used methods for all CHD patients are shown different from those for the control groups. The first and second control groups do not show statistically significant differences between themselves. Our results show not only a significant difference of the aggregation parameters characteristic of patients compared to those of healthy people, but also a correspondence between the parameters measured *in vivo* and *in vitro*. RBC aggregate in CHD patients faster and more numerously, in particular the aggregation index increases by $20 \pm 7\%$.

The comorbidity of T2DM also significantly elevates aggregation in CHD patients. In particular, in CHD patients compared to the control group AI is higher by $20 \pm 7\%$ ($p < 0.05$), meaning more numerous aggregation, $T_{1/2}$ is lower by $14 \pm 9\%$ ($p < 0.05$), meaning faster aggregation, and T_{agg} is lower by $27 \pm 7\%$ ($p < 0.05$), showing faster doublet formation. As for CBV, it is smaller than in the control. The two groups CHD patients (with and without T2DM) show significant ($p < 0.05$) differences. The AI parameter for all studied groups decreases with an increase in CBV, while $T_{1/2}$, on the other hand, increases. T_{agg} remains constant for the whole CBV range. These results show that for patients with high CBV, the aggregation process *in vitro* is weaker compared to that for the patients with low CBV: it is less numerous and the doublet formation takes longer time. No statistically significant difference in aggregation was found between several patient subgroups, including the division by gender and smoking habits. AI weakly correlated with BMI and did not correlate with age.

The novelty of this work consists in a complex analysis of the parameters measured *in vitro* and *in vivo* for different groups of people. The results of studies performed by alternative methods do not contradict our conclusions and show increased aggregation of RBC in patients with CHD (including complications) compared to healthy donors [1, 10]. One of the limitations of the study is the small number of patients with both CHD and T2DM; in the future, we plan to increase this number. Another point that can be improved is the observation of additional factors that influence the blood flow, for example plasma components [1]. Also, BMI and other factors influence platelet activation and aggregation, which can indirectly affect the aggregation of RBCs; this was not accounted for in this work.

Acknowledgment: The authors acknowledge the financial support provided to this study by RFBR grant № 19-52-51015.

References

- [1] O. Baskurt, B. Neu, H. Meiselman, Red Blood Cell Aggregation, CRC Press, Boca Raton, 2012.
- [2] R. Hochmuth, Micropipette aspiration of living cells. *J. Biomechanics* 33(1), 15–22, 2000.
- [3] A. Priezzhev, K. Lee, N. Firsov, J. Lademann, Optical Study of RBC Aggregation in Whole Blood Samples and Single Cells. In: Handbook on Optical Biomedical Diagnostics, 2nd ed., V.V. Tuchin – editor, SPIE Press: Bellingham, Washington, pp. 5–36, 2016.
- [4] A. Muravyov, I. Tikhomirova, A. Maimistova, S. Bulaeva, P. Mikhailov, N. Kislov, Red blood cell aggregation changes are dependent on its initial value: Effect of long-term drug treatment and short-term cell incubation with drug, *Clin. Hemorheol. Microcirc.* 48(4), 231–240, 2011.
- [5] S. Shin, Y. Yang, J. Suh, Measurement of erythrocyte aggregation in a microchip stirring system by light transmission, *Clin. Hemorheol. Microcirc.* 41(3), 197–207, 2009.
- [6] V.V. Lopatin, A.V. Priezzhev, Multiple light scattering by suspensions of erythrocytes in geometrical optics approximation, *Proc. SPIE* 4749, 267–274, 2002.
- [7] P. Ermolinskiy, A. Lugovtsov, A. Maslyanitsina, A. Semenov, L. Dyachuk, A. Priezzhev, Interaction of erythrocytes in the process of pair aggregation in blood samples from patients with arterial hypertension and healthy donors: measurements with laser tweezers, *J. Biomed. Photonics & Eng.* 4(3), 030303, 2018.
- [8] K. Lee, M. Kinnunen, M. Khokhlova, E. Lyubin, A. Priezzhev, I. Meglinski, A. Fedyanin, Optical tweezers study of red blood cell aggregation and disaggregation in plasma and protein solutions, *J. Biomed. Opt.* 21(3), 035001, 2016.
- [9] Yu. Gurfinkel, O. Suchkova, M. Sasonko, A. Priezzhev, Implementation of digital optical capillaroscopy for quantifying and estimating the microvascular abnormalities in diabetes mellitus, *Proc. SPIE* 9917, 991703, 2015.
- [10] Q. Yang, J.H. Wang, D.D. Huang, D.G. Li, B. Chen, L.M. Zhang, C.L. Yuan, L.J. Cai, Clinical significance of analysis of the level of blood fat, CRP and hemorheological indicators in the diagnosis of elder coronary heart disease, *Saudi J. Biol. Sciences* 25(8), 1812–1816, 2018.

STRUCTURAL AND FUNCTIONAL OPTICAL COHERENCE TOMOGRAPHY, TECHNOLOGY AND APPLICATIONS

ZHIHUA DING, ZHIYI LIU, JIANRONG QIU, JIA MENG, TAO HAN

College of Optical Science and Engineering, State Key Lab of Modern Optical Instrumentation, Zhejiang University, China

zh_ding@zju.edu.cn

Abstract

Optical coherence tomography (OCT) systems with ultralong depth range, ultrawide lateral field, ultrahigh axial resolution, and enhanced contrasts are introduced. As a depth-resolved optical imaging modality with the merits of non-destruction, high-resolution, and high-speed, OCT is promising for applications in variety areas. Most recently, our group has made a step forward in OCT instrumentations. The depth range is extended to be over 200 mm, the lateral field of view is increased to be 35 mm, and the axial resolution is improved to be 0.9 μm . Angio-OCT with enhanced contrast is developed for vasculature mapping. Pump-probe OCT with molecular contrast is also developed. These novel OCT systems will open new OCT applications.

Figure 1(a) shows the developed Orthogonal Dispersive Spectral Domain OCT (OD-SDOCT) system [1-3]. Dimensional metrology of the central optical distances in assembled lenses based on this system is given in Fig. 1(b). In comparison with commercial product (LS200, Fogale), our system achieves greatly enhancement in precision ($>10 \times$) and speed ($>30 \times$). Uniform focusing with an extended depth range and increased working distance for OCT probe is designed and fabricated [4,5]. Figure 2(a) gives the simulated field intensity of the output beams for six typical cases of the designed probe. Microscope image of the fabricated probe and in vivo 3D OCT images of human skin at the fingertip are shown in Fig. 2(b). With merits of enhanced imaging quality and easy fabrication, the proposed probe poses great potential for important applications, especially for endoscopic imaging of human internal organs *in vivo*.

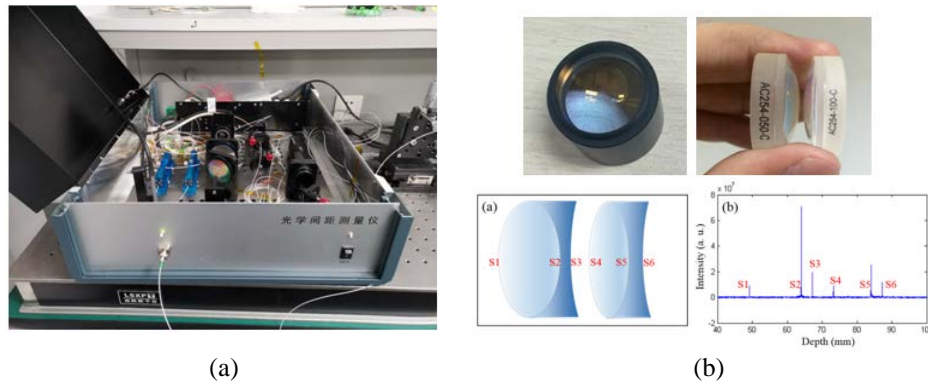


Figure 1: (a) Developed OD-SDOCT system - (b) Typical measurement results of the central optical distances in assembled lenses

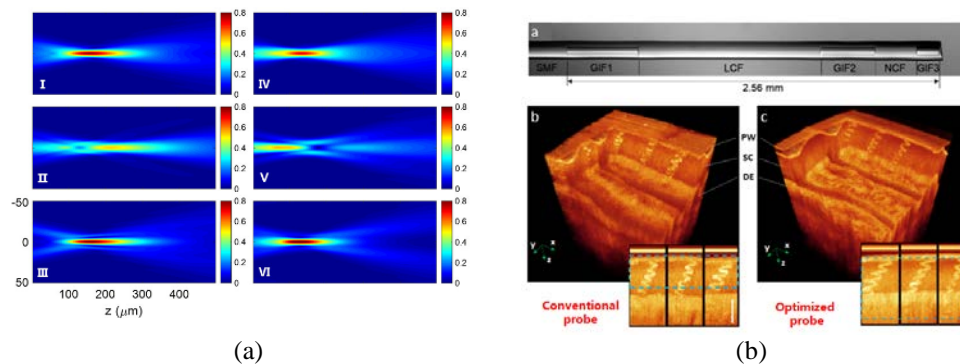


Figure 2: (a) Simulated field intensity of the output beams for six typical cases of the designed probe - (b) Microscope image of the fabricated probe and in vivo 3D OCT images of human skin at the fingertip

References

- [1] C. Wang, Z. Ding, S. Mei, H. Yu, W. Hong, Y. Yan, W. Shen, Ultralong-range phase imaging with orthogonal dispersive spectral domain optical coherence tomography, *Opt. Lett.* 4555-4557, 2012.
- [2] W. Bao, Z. Ding, P. Li, Z. Chen, Y. Shen, C. Wang, Orthogonal dispersive spectral-domain optical coherence tomography, *Opt. Exp.* 10081-10090, 2014.
- [3] W. Bao, Y. Shen, T. Chen, P. Li, Z. Ding, High-speed high-precision and ultralong-range complex spectral domain dimensional metrology, *Opt. Exp.* 11013-11022, 2015.
- [4] J. Qiu, Y. Shen, Z. Shangguan, W. Bao, S. Yang, P. Li, Z. Ding, All-fiber probe for optical coherence tomography with an extended depth of focus by a high-efficient fiber-based filter, *Opt. Comm.* 276-282, 2018.
- [5] J. Qiu, T. Han, Z. Liu, J. Meng, Z. Ding, Uniform focusing with extended depth range and increased working distance for optical coherence tomography by an ultrathin monolith fiber probe, *Opt. Lett.* 976-979, 2020.

MOUSE: ADVANCED APPROACHES TO SKIN *IN VIVO* OPTICAL CLEARINGELINA A. GENINA^{1,2}, ALEXEY N. BASHKATOV^{1,2}, VALERY V. TUCHIN^{1,2,3}, AND VLADIMIR P. ZHAROV^{1,4}¹Saratov State University, Russia²National Research Tomsk State University, Russia³Institute of Precision Mechanics and Control RAS, Russia⁴Arkansas Nanomedicine Center, University of Arkansas for Medical Sciences, USA

eagenina@yandex.ru

Abstract

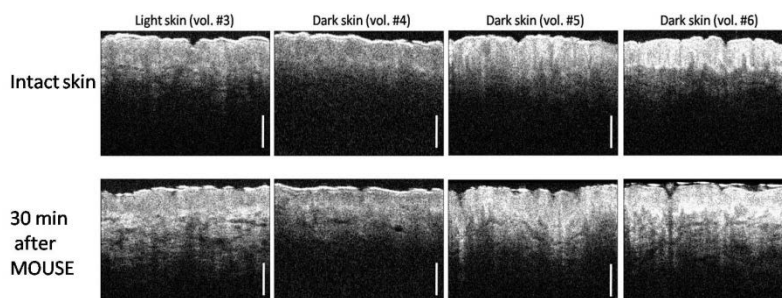
Immersion optical clearing of biological tissue that reduces the influence of light scattering on the quality of optical imaging led to breakthrough in biophotonic studies of tissue properties *ex vivo* [1, 2]. However, applications of these techniques in human skin *in vivo* is challenging due to low efficiency, toxicity concerns, and time consuming procedure. The use of biocompatible optical clearing agents makes it possible to some increase the probing depth of non-invasive optical diagnostic methods [3, 4]. However, the protective epidermal barrier of the skin prevents the penetration of immersion liquids into the deeper layers of the skin.

Based on our discoveries described here, we propose to solve the indicated above problems by combination of physical factors such as microdermabrasion and sonophoresis, which all are approved for application in humans. Our ultimate goal was to clarify the contribution of the Microdermabrasion, Oleic acid and UltraSound Effect (MOUSE) on optical clearing of human skin measured by OCT *in vivo* separately and in various combinations and to compare results obtained for light (II-type) and dark (VI-type) skin.

This study involved healthy volunteers 19-23 years old with II and VI skin types. Microdermabrasion associated with mechanical peeling and massage was performed applied using a commercially available device with sapphire tip and vacuum massager. Sonophoresis was performed using a commercially available ultrasonic therapeutic device. Optical coherence tomography (OCT) allowed to differentiate the contribution of each factors separately and in different combinations.

Results have demonstrated that topical application of MOUSE can provide increasing the optical penetration depth in human skin *in vivo* during short time. After optimization, OCT-signal amplitude increased more than 3-fold with twice improved depth penetration for light skin during 30 minutes that significantly exceed the results obtained earlier (Fig. 1a,b). All optical clearing approaches were tested on skin with VI phototype (deeply pigmented dark brown to black skin according to Fitzpatrick Skin Type Classification Scale). After combined optical clearing 1.3-fold increase in OCT-signal amplitude was achieved for dark skin (Fig. 1a,c).

These results show a high potential of the advanced clearing techniques for broad application in the optical diagnostics of skin and peripheral blood and lymphatic systems. MOUSE has not required a multicomponent composition of the OCA and has not caused dehydration and shrinkage of the skin, which are induced by hyperosmotic hydrophilic agents. Consequently, there is a low risk of side effects. A comparison of the presented results has shown that the use of MOUSE for optical clearing of epidermis has significant advantages compared with separate use of microdermabrasion and sonophoresis for both light and dark skin. MOUSE has allowed significant increasing OCT signal amplitude during only 15-20 min that has been not demonstrated with other approaches. The novelty of this work is also discovering that OCT optical probing depth increases in skin due to only ultrasound impact without optical clearing agent application. Comparison of the MOUSE in light and dark skin has revealed similarity of the optical clearing mechanisms and differences in the magnitude of the effect. The obtained OCT optical probing depth increase of dark skin is a novel result, which is practically and socially relevant.



a

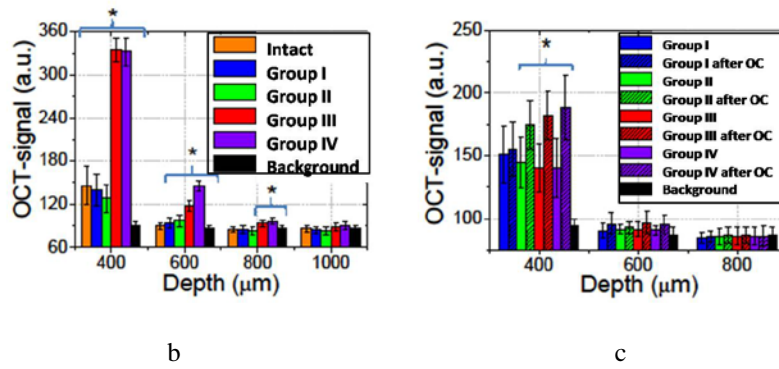


Figure 1: OCT B-scans of light and dark skin before and after MOUSE (a). Results are presented for volunteers ## 3-6. OCT-signal amplitude for light (a) and dark (b) skin before and 30 min after application of oleic acid (OA) on an intact skin surface (Group I); microdermabrasion followed by a single application of OA (Group II); combined application of OA and sonophoresis (Group III); microdermabrasion followed by application of OA and sonophoresis – MOUSE (Group IV). Results are averaged. Braces with asterisks combine groups with statistically significant differences between the OCT and the background signal ($p < 0.05$). Figure is adapted from figures published in Ref. [5]. Bars correspond to 200 μm .

References

- [1] D. Zhu et al, Laser & Photonics Reviews 7, 732–757, 2013.
- [2] P. Matryba et al, Laser Photon. Rev.13, 1800292, 2019.
- [3] I. Costantini et al, Biomed. Opt. Express 10, 5251-5267, 2019.
- [4] Q. Zhao et al, Sci. Rep. 6, 34954, 2016.
- [5] E.A.Genina, et al, IEEE Trans Med Imaging 39, 3198-3206, 2020.

HIGH AFFINITY LIGANDS FOR PRECISE TUMOR DIAGNOSIS

YUEQING GU

Department of Engineering, China Pharmaceutical University, China

cpuyueqing@163.com

Abstract

Selective tumor targeting *in vivo* can be achieved by monoclonal antibodies, which specifically bind to target receptors. However, most antibodies are immunogenic and have long plasma half-lives rendering them suboptimal for molecular imaging. Small peptides and biomolecules are therefore preferred for biological imaging because of their low immunogenicity, reduced barriers to topical delivery, high affinity and selectivity for receptors, and desirable pharmacokinetic properties.

Cyclic RGD peptides are small molecules that bind $\alpha\beta3$ integrin with high affinity. For this reason, a variety of RGD containing peptides has been developed for targeting tumor-induced angiogenic blood vessels or tumor-associated integrin. Conjugation of these peptides to imaging agents or drugs affords bioactive molecules for cancer imaging and targeted therapy, respectively. However, the cyclic RGD structure requires complicated peptide synthesis leading to increase in production cost and difficulty in quality control. Also, recent studies have demonstrated the strong binding affinity of RGD-containing peptides not only to $\alpha\beta3$ integrin receptor but also to $\alpha\beta5$ and $\alpha5\beta1$ integrins. Therefore, efforts to develop alternative small linear peptides with similar or even higher affinity and specificity to $\alpha\beta3$ integrin than cyclic RGD motif peptide have attracted much attention.

Computer-assisted virtual screening is an effective method for drug discovery of small molecules with binding affinity to target receptors. Structure-based pharmacophore strategy has been successfully used to screen small molecule leading compounds in drug development. Molecular docking and dynamic simulation are also considered practical methods to analyze the intermolecular interaction and explain the binding affinity and stability. Therefore, the combination of pharmacophore models with molecular docking will render more efficient hits. Although the compounds obtained from virtual screening have the potential specificity for the targets, it is necessary to confirm the feasibility of this approach by *in vitro* and *in vivo* experiments. In this study, we have integrated structure-based pharmacophore method with molecular docking to screen the linear bioactive peptides for identifying $\alpha\beta3$ integrin. Two novel small linear peptides (RW_r, RW_rNM) were selected with strong molecular interactions with $\alpha\beta3$ integrin. To evaluate the affinity of these two peptides to $\alpha\beta3$, cell lines with different expression levels of $\alpha\beta3$ were cultured with fluorescence dye-labeled RW_r and RW_rNM. Confocal imaging and flow cytometry were used to identify their affinity and specificity to $\alpha\beta3$. Microscale thermophoresis (MST) was performed to quantify affinity of both peptides to $\alpha\beta3$ integrin. Furthermore, the effects of RW_rNM and RW_r on cell migration, angiogenesis, and downstream signaling pathways of $\alpha\beta3$ were investigated. The tumor targeting ability and the therapeutic efficacy of peptide conjugates were further studied.

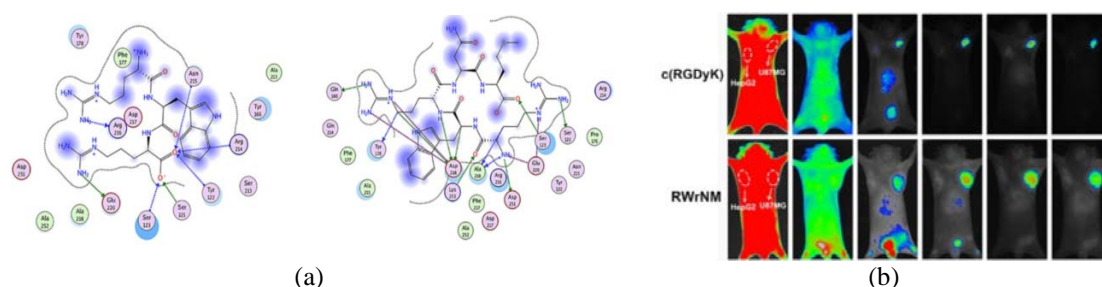


Figure: (a) Binding affinity of the peptides to $\alpha\beta3$ integrin at molecular level. (b) *In vivo* tumor targeting ability of peptides.

OPTIMIZATION OF SPECTRAL AND SPATIAL LIGHT BEAM DISTRIBUTION OF OPTICAL SYSTEMS FOR PHOTODYNAMIC THERAPY

ANDREY BELIKOV AND YULIA SEMYASHKINA

Faculty of Laser Photonics and Optoelectronics, ITMO University, Russia

avbelikov@gmail.com

Abstract

Optical devices are widely applied in science, technology, and medicine. Modern medicine is developing, giving way to the use of optical devices for phototherapy of various diseases. Among the current phototherapy technologies one can highlight photodynamic therapy.

Photodynamic therapy (PDT) is an advanced method of treatment that provides for the penetration of a photoactive dye (photosensitizer) into biological tissue. The photosensitizer is delivered to pathogenic cells, where, effected by light, it triggers a photochemical reaction with the release of singlet oxygen destroying the pathogenic cells. For PDT those photosensitizers are used that effectively absorb light in the wavelength range of 600-700 nm. This range falls within the so-called "therapeutic window" encompassing the most transparent biological tissues resulting from the low absorption of blood in this spectral area [1]. The second generation of e6-chlorin-based photosensitizers are considered the drugs-of-choice. PDT is successfully used in oncology and is now being developed gaining new fields of applications. Including PDT of onychomycosis that is an infectious nail disease of fungal etiology. For effective and safe photodynamic treatment of onychomycosis it is necessary to selectively impact the photosensitizer absorbed by the nail tissue affected by the fungus and develop extremely high-intensity light sources. In that regard it is important to optimize the spectral, temporal and spatial distribution of the light source, including matching the spectrum of its radiation with the absorption spectrum of the photosensitizer, minimizing the procedure time, creating a uniform distribution of radiation on the area of the nail containing the dye affected by the fungus. The result of the interaction of light and biological tissue during photodynamic therapy depends, among other things, on the spatial distribution of light, The optimization of that distribution allows impacting biological tissue effectively and safely for the surrounding tissues, it is being particularly important in the treatment of onychomycosis and in the development of new effective optical devices for the treatment of this disease, as well as for a wide range of medical applications.

The goal of this work is to optimize the spatial distribution of the optical systems' light flux for photodynamic therapy. To achieve this goal, it is necessary to solve the following tasks: Investigate the absorption spectrum of the modern chlorin-containing drugs at different concentrations in an aqueous solution, at different intensities and different timing of light exposure with a wavelength of 656 ± 10 nm. To define requirements for the optimal dynamics of the light exposure for PDT. Development of a computer optical model of onychomycosis. Calculation of light distribution in this model. Establishing correlation between the distribution of light on the surface of the model and in the area containing the photosensitizer. Developing requirements for light distribution on the surface of fingers affected by onychomycosis optimal for PDT.

Spectral Investigation

The absorption spectra of the photosensitizing drugs "Revixan" (Areal Ltd., Russia) and "Chloderm" (DPT Laboratory Ltd, USA) were studied. The spectra of those drugs in the range of 600–700 nm proved to be close to each other that is obviously associated with the use of chlorine e6 as a photodynamic agent in both drugs. The absorption band maximum for both drugs is equal to 654 ± 1 nm. The behavior of the absorption spectra of an aqueous solution of photosensitizing drugs at different intensities and different timing of exposure to light with a wavelength of 656 ± 10 nm was investigated. For photosensitizing drugs illumination, the LED device for PDT "LED Forester 660" (Nela Ltd., Russia) with intensity of radiation up to 180 ± 20 mW/cm² was used. The intensity of radiation on the surface of biological tissue is limited by thermal damage to an organ or tissue (for skin ~ 200 mW/cm²[2]).

One can describe the dependence of the "Revixan" absorption coefficient at a wavelength of 654 nm corresponding to the peak of its absorption band on the intensity of exposure to LED radiation with a wavelength of 656 ± 10 nm with the function:

$$k_{R_{654}}(I) = 1.3 * (I + 0.001)^{-0.18}, \quad (1)$$

where: I – intensity of radiation, W/m², and on the time of exposure with the intensity up to 180 ± 20 mW/cm² with the function:

$$k_{R_{654}}(t) = (t + 0.001)^{-0.08}, \quad (2)$$

where: t - time of exposure to radiation, s.

One can describe the dependence of the "Chloderm" absorption coefficient (at a wavelength of 654 nm corresponding to the peak of its absorption band) on the intensity of exposure to LED radiation with a wavelength of 656 ± 10 nm with the function:

$$k_{Ch_{654}}(I) = 1.34 * (I + 0.001)^{-0.165}, \quad (3)$$

where I – intensity of radiation, W/m^2 , and on the time of exposure with the intensity up to $180 \pm 20 W/cm^2$ with the function:

$$k_{Ch_{654}}(t) = 2 * (t + 0.001)^{-0.12}, \quad (4)$$

where t – time of exposure to radiation, s.

Thus, the effect of LED radiation changes the absorption spectra of chlorin-containing photosensitizing drugs for photodynamic therapy, while an increase in the intensity and time of exposure to LED radiation results in decreasing absorption of those photosensitizers in the range of 600-700 nm and a shift of their peak absorption band being within that range in the IR area. When chlorin-containing photosensitizing drugs are exposed to LED radiation with a wavelength of 656 ± 10 nm and a constant intensity of $180 \pm 20 W/cm^2$, the absorption coefficient at a wavelength corresponding to the absorption peak of drugs changes over time according to

$$k(t) = A * (t + 0.001)^B, \quad (5)$$

where the coefficient A is in the range 1-2; coefficient B - in the range $-0.12 \div -0.08$.

Therefore, the change in the intensity of LED radiation with a wavelength of 656 ± 10 nm over time according to

$$I = (A * (t + 0.001)^B)^{-1}, \quad (6)$$

where coefficient A - stays in the range 1-2; coefficient B - in the range $-0.12 \div -0.08$, provides a constant, during PDT with an initial intensity of $180 \pm 20 W/cm^2$, the rate of absorption of light energy by a chlorin-containing photosensitizing drug.

The results obtained in this work can help to get deeper understanding of the processes occurring during photodynamic therapy of various diseases, including PDT of onychomycosis, to construct the models describing interaction of light with photosensitizers in biological tissue, as well as to develop recommendations on photodynamic therapy scenario that takes into account the process of photobleaching of the photodynamic agent and the dynamics of its absorption at the wavelength of the exciting radiation.

Information on the behavior of the photosensitizer absorption coefficient resulting from the exposure to light or as a result as well as changing photosensitizer concentration while penetrating biological tissue combined with the attenuation of the exciting radiation intensity during its propagation in biological tissue will enable finding adequate light radiation power absorbed by the photosensitizer and choosing the best radiation wavelength, intensity and exposure time necessary for the most effective photodynamic therapy of neoplasms localized at different depths in biological tissue.

Spatial Distribution Modeling

The structural model of a nail affected by onychomycosis is shown in Figure 1. It was the first time when the model takes into account the role of the anterior part of the toe and the proximal nail fold. The proximal nail fold and the anterior part of the toe are covered by skin epidermis. When constructing the model, for the first time, the fact was taken into account that in different parts of the nail the sizes of the layers forming it, as well as their shape, can differ. At the preparation stage for PDT a hardware pedicure is performed while the nail plate is polished, leaving about 50 microns of its thickness. For this reason, the nail plate is divided into two parts: from the anterior of the finger to the proximal nail fold, its thickness amounts to 50 μm , under the nail fold - 300 μm .

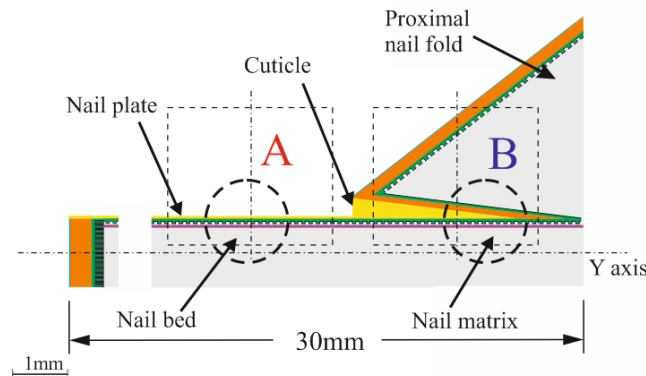


Figure 1: The structural model structure of the nail affected by onychomycosis.

The fungus was modeled by a layer of a photosensitizing drug that is found behind the papillary dermis and completely absorbing all the light incident on it. The optical properties of the layers included in the developed model were selected basing on the analysis of literature data [3-7]. Optical modeling was performed by means of TracePro-Expert 7.0.1 Release program (Lambda Research Corporation, USA). The light source was a platform emitting in the direction of the nail plate oriented parallel to the surface of the nail plate, the radiation wavelength was equal to 660 nm. The distribution of the light intensity of the source could be preset; besides it could be uniform. The intensity of the light radiation from the source is 200 mW/cm^2 . As a result of calculations, it was found that with a uniform distribution of light on the surface of the nail model in the area under the grinded nail plate the density of the light power absorbed by the photosensitizing drug is 155 mW/cm^2 , and in the area under the nail fold - 8 mW/cm^2 , i.e. the distribution of the power absorbed by the drug in this case is not uniform in space (despite the uniform spatial distribution of the source) that can lead to excessive or, on the contrary, insufficient photodynamic effect in different parts of the fungus (drug) localization area. In order to achieve a uniform spatial distribution of the power absorbed by the photosensitizing drug, and therefore the optimal photodynamic effect with an effect of hypothermia, restricted by the intensity of the light source (200 mW/cm^2), two methods are suggest.

First method. A source with an uneven spatial distribution of intensity. Set the intensity of light incident on the surface of area B (see Figure 1) located under the nail fold as high as possible (restricted by the effect of hyperthermia and equal to 200 mW/cm^2), and reduce the intensity of light incident on the surface of area A (see Figure 1) located under grinded nail plate by 19-20 times (up to $10\text{-}10.5 \text{ mW/cm}^2$), while the timing of light exposure on the nail plate and on the nail fold should be equal to each other.

Second method. Source with uneven temporal distribution. Set the intensity of the light incident on the surface of the areas under the grinded nail plate and under the nail fold at the same and maximum rate, but increase the irradiation time for area B under the nail fold by 19-20 times compared to the time of irradiation of the area under the grinded nail plate.

Figure 2 shows the distribution of light intensity created on the surface of the optical model of a nail affected by onychomycosis by a source with an uneven distribution of intensity in space. The borderline between the source light intensity distributions is oriented along the nail cuticle. Within each of those two distributions, light is evenly distributed in space.

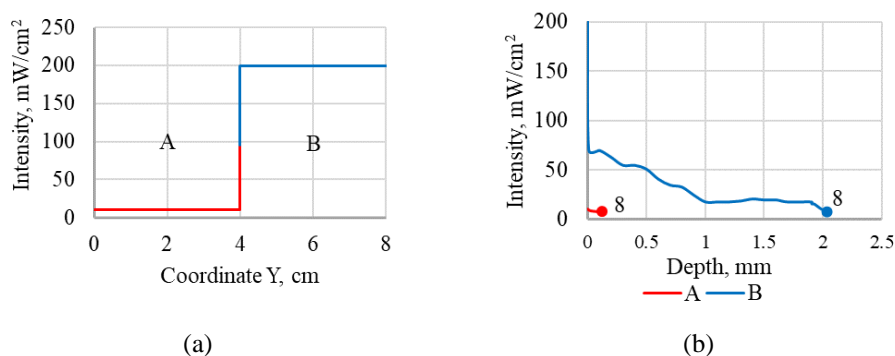


Figure 2: The light intensity distribution on the surface of the optical model of the nail affected by onychomycosis created by a source with an uneven spatial distribution of intensity (a) and absorbed by the photosensitizing drug (b) from this source in the area under the grinded off nail plate (red color) and in the area under the proximal nail fold (blue color).

One can see that with an uneven distribution of light on the surface of a developed nail model in the area under the grinded nail plate, the density of the light power absorbed by the photosensitizing preparation is 8 mW/cm^2 and is equal to the density in the area under the nail fold, i.e. the distribution of the power absorbed by the photosensitizing drug in this case is uniform in space (despite the uneven spatial distribution of the source) that allows for the same photodynamic effect in different parts of the fungus (drug) localization area.

Conclusion

It has been demonstrated that exposure to LED radiation with a wavelength of $656 \pm 10 \text{ nm}$ changes the absorption spectra of chlorin-containing photosensitizing drugs for photodynamic therapy, while an increase in the intensity and time of exposure to LED radiation leads to a decrease in the absorption of these photosensitizers in the range of $600\text{-}700 \text{ nm}$ and a shift of their peak absorption band lying in this range in the IR area.

It was found that in case chlorin-containing photosensitizing drugs are exposed to LED radiation with a wavelength of $656 \pm 10 \text{ nm}$ and a constant intensity of $180 \pm 20 \text{ W/cm}^2$, the absorption coefficient at a wavelength corresponding to the drug absorption peak changes over time according to the formula: $k(t) = A * (t + 0.001)^B$, where the coefficient A is in the range 1-2; coefficient B - in the range $-0.12 \div -0.08$.

The original computer optical model of a nail affected by onychomycosis was described. It has been demonstrated that if the spatial distribution created by LED radiation with a wavelength of $656 \pm 10 \text{ nm}$ on the surface of toes or hands affected by onychomycosis is divide into two areas and if the intensity in each of them areas make different by several times and

if the border line between those areas will be oriented along the cuticle of the nail, then in this case possible forming up a uniform spatial distribution of light intensity in an area affected by onychomycosis and located under the nail.

References

- [1] V.V. Tuchin, Light scattering study of tissues, UFN. 517-539, 1997.
- [2] N.N. Bulgakova, I.A. Shugaylov, Photodynamic therapy (review), Innovative Dentistry. 14-23, 2012.
- [3] Shi J. et al. Human nail stem cells are retained but hypofunctional during aging, Journal of molecular histology. 303-316, 2018.
- [4] Dynamics and Fluctuations in Biomedical Photonics VIII, edited by Valery V. Tuchin, Donald D. Duncan, Kirill V. Larin, Martin J. Leahy, Ruikang K. Wang, Proc. of SPIE. p. 78980Z, 2011.
- [5] Y. Mashita et al., Measurement of the optical properties of nails, APBP 2004. 44-45, 2004.
- [6] T. Lister, P.A. Wright, P.H. Chappell, Optical properties of human skin, J. Biomed. Opt. p. 090901, 2012.
- [7] A.V. Khilov, D.A. Loginova, E.A. Sergeeva, M.A. Shakhova, A.E. Meller, I.V. Turchin, M.Yu. Kirillin Two-Wavelength Fluorescence Monitoring and Planning of Photodynamic Therapy, Modern Technologies in Medicine. 96-105, 2017.

BREAKTHROUGH STRATEGIES OF STIMULATION OF THE CEREBRAL LYMPHATICS DURING SLEEP

OXANA SEMYACHKINA-GLUSHKOVSKAYA^{1,2}, THOMAS PENZEL^{1,3}, JURGEN KURTHS^{1,4}, VALERY TUCHIN^{1,5,6}

¹Saratov State University, Astrakhanskaya str., 83, Saratov, 410012, Russia

²Physics Department, Humboldt University, Newtonstrasse 15, 12489 Berlin, Germany

³Advanced Sleep Research GmbH, Berlin, Germany, Charitéplatz 1, 10117 Berlin, Germany

⁴Potsdam Institute for Climate Impact Research, Telegrafenberg A31, 14473 Potsdam, Germany

⁵Institute of Precision Mechanics and Control, Russian Academy of Science, Saratov, Russia

⁶National Research Tomsk State University, Tomsk, Russia

glushkovskaya@mail.ru

Abstract

There is an intensive growing body of evidence that sleep and the lymphatics play a crucial role in keeping the health of the central nervous system (CNS) via the night activation of drainage of CNS tissues and clearance of metabolites and neurotoxins. The ability to stimulate the brain drainage and clearing function during sleep might be a promising strategy in developing of innovative methods in neurorehabilitation therapy. Here we discuss that sleep is the natural driving factor for activation of the cerebral lymphatics and is a platform for development of innovative optical strategies in stimulation of drainage and cleaning function of the cerebral lymphatics. We strongly believe that this pioneering step will motivate researchers and industrial partners to develop novel promising devices for neurorehabilitation medicine based on the night stimulation of lymphatic functions.

1. Photostimulation of the lymphatic system

The transcranial photostimulation (tPS) is considered as a possible novel nonpharmacological and non-invasive promising strategy for prevention or delay of Alzheimer's disease (AD) [1–7], depression [8–13], Parkinson's disease [14], stroke [15,16], traumatic brain injuries [17,18], post-mastectomy lymphedema [19,20], and post-surgical swelling [21,22]. The PS, known as low-level laser therapy, was first proposed by Endre Mester in 1967 for stimulation of hair growth [23] and in 1971 for wound healing [24]. The PS has broadened to include near-infrared wavelengths 600–1200 nm. The better tissue penetration properties of near-infrared light, together with its good efficacy, made it the most popular wavelength range. The PS-mediated stimulation of lymphatic drainage and clearing function might be one of the mechanisms underlying an important role of PS in neurorehabilitation [25]. Due to a good penetration of PS into the brain cortex, tPS can stimulate the meningeal lymphatic vessels (MLVs). In our recent pilot study on mice with the injected AD model, we have clearly demonstrated that 9 days course of tPS (1267 nm, 32 J/cm² 97) strongly reduces A β plaques in the brain which is associated with improving of the memory and neurocognitive deficit [1]. Based on our data on the real time monitoring of lymphatic clearance of gold nanorods (GNRs) from the cortex, the hippocampus, the right ventricle, and the cisterna magna, we have proposed that the tPS-mediated stimulation of lymphatic drainage might be a possible mechanism underlying the tPS-elimination of A β from the brain. These results open breakthrough strategies for a non-pharmacological therapy of AD and give strong evidence that tPS might be a promising therapeutic target for preventing or delaying AD. We investigated possible mechanisms of tPS-stimulation of lymphatic drainage and clearance [26,27]. Our results demonstrate that already low PS doses (1267 nm, 5 and 10 J/cm²) cause relaxation of the mesenteric LVs and increase their permeability to fluorescent macrophages via a decrease of expression of tight junction and transendothelial resistance. We hypothesized that a PS-mediated increase in the permeability of the lymphatic endothelium might be the mechanism of transport of macromolecules and cells in the narrow cerebral lymphatic vessels (LVs). The increasing of permeability of the lymphatic endothelium is the key factor underlying lipids diffusion and macromolecules from the tissues to LVs, which may help to explain why the adipose tissue is always located adjacent to collecting lymphatics and lymph nodes [28–30]. The transport of macromolecules across the collecting LVs is coupled to water flux and sensitive to lymph pressure [28]. The inherent permeability of LVs is sufficient to broadcast antigens, passing within lymph to the cLNs [29]. Kuan et al. clearly demonstrated that the delivery of soluble antigens such as FITC-conjugated endogenous proteins and E α -GFP is possible due to the permeability of the LVs [29]. This process exposes a large community of endocytic and phagocytic cells, particularly dendritic cells and macrophages. Physiological mechanisms underlying the lymphatic permeability to macromolecules remain, however, unknown. The possible role of Lymphatic vessel endothelial hyaluronan receptor 1 (Lyve-1) and Chemokine C-C motif ligand 21 (CCL21) might be involved in the regulation of migration of immune cells through the lymphatic endothelium. The Lyve-1 is a transmembrane receptor of hyaluronan, which regulates cell migration in the course of wound healing, inflammation, and embryonic morphogenesis [31]. This protein is expressed primarily on both the luminal and abluminal surface of the lymphatic endothelium [31,32] and plays an important role in hyaluronan transport providing for migration of immune

cells [33]. The CCL21 is secreted by the lymphatic endothelial cells and is involved in activation of T-lymphocyte movement, migration of the lymphocytes to other organs, and dendritic cells into the lymph nodes [34]. Nitric oxide (NO) can be another modulating factor of lymph flow [35–40]. There are multiple sources of NO that could influence on the LVs functions: 1) NO production from the endothelial nitric synthase in the lymphatic endothelium; 2) NO generation from the inducible nitric synthase in immune cells; 3) NO release from neural nitric synthase in the parenchyma or the perivascular lymphatic nerves [38,40–43], 4) countercurrent exchange of NO from adjacent arteries or veins. The predominant NO production in the LVs occurs in the valve-bulb region [44,45]. The high-shear force of lymph flowing through the open valve leaflets contributes to elevating of NO levels near the valve. The NO-mediated modulation of valves closing and opening coordinates the flow of lymph in the LVs [46]. In sum, the data above open new strategies for an alternative non-pharmacological therapy of brain diseases via PS modulation of lymphatic mechanisms of drainage and clearance of CNS tissues.

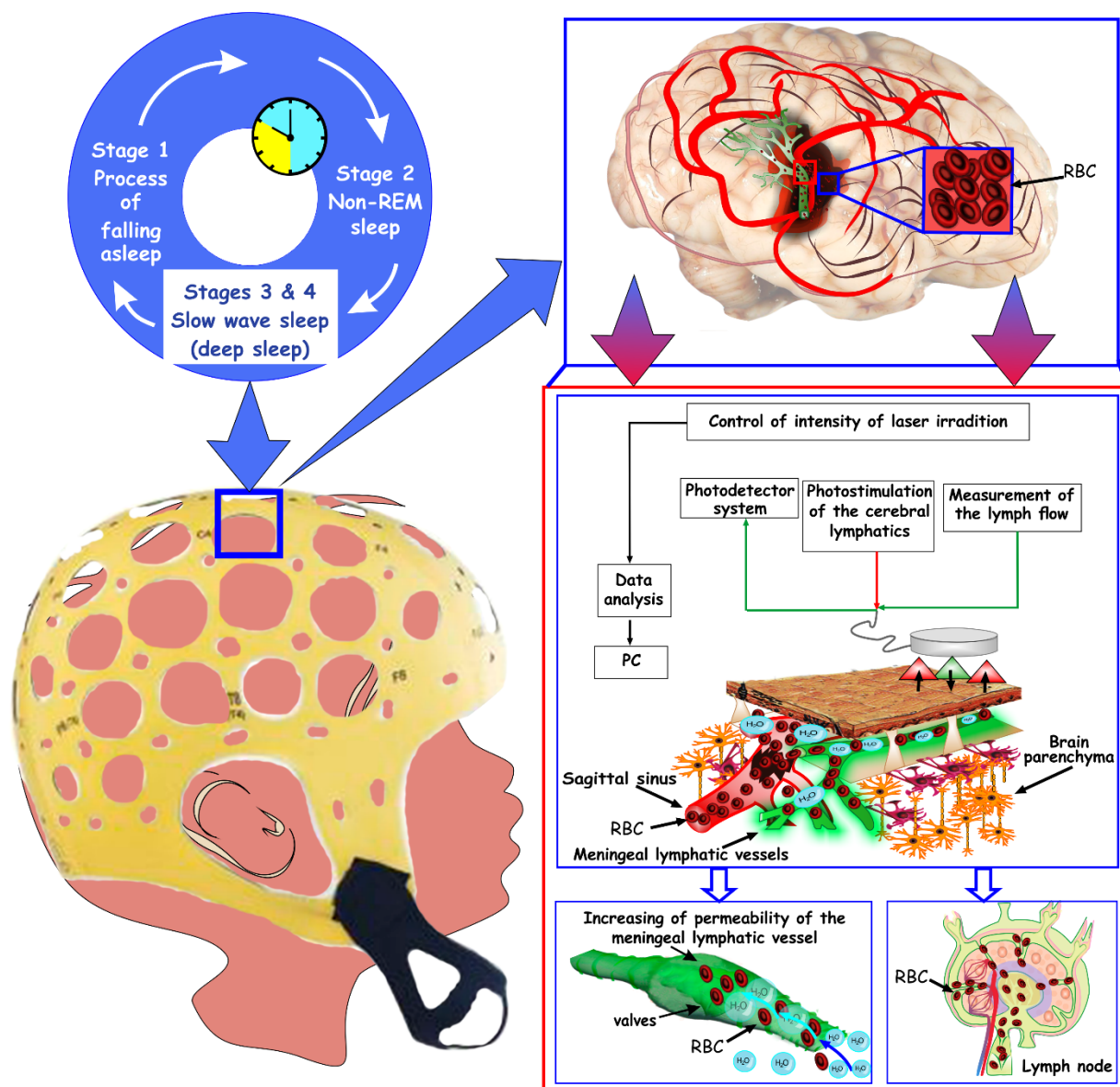


Figure 1: Schematic illustration of possible PS-stimulation of the lymphatic clearance of RBCs from the brain after ICH. The PS applied during deep sleep (SWA) increases the drainage and clearing functions of the MLVs, which provide the transport of RBCs into the dCLNs. Two systems of photo-detection and measurement of the lymph flow (see Section “Measurement of the lymph flow”) control the intensity of PS and the lymphatic response to PS that is automatically analyzed on PC.

2. Potential stimulatory effects of deep sleep on drainage and clearance of the brain.

Sleep can be the natural driving factor for activation of the drainage and clearance of the brain via the lymphatics. The functions of sleep have been speculated already in ancient works such as “Aristotle’s Theory of ‘Sleep and Dreams’” [47]. However, only recently researchers have discovered that sleep has a crucial function of clearance of metabolites and neurotoxic wastes from the brain [48,49]. The clearance of toxic proteins such as beta-amyloid ($A\beta$) [50] and tau [51] from the brain strongly depends on sleep and neural activity [49,52–54]. Notice that not all stages of sleep are involved in the drainage and clearing functions of the brain. The electrical brain activity measured by the electroencephalography (EEG) during wakefulness is characterized by a small amplitude pattern. During most part of sleep, called non-rapid eye

movement (NREM) sleep, which accounts 80% of total time of sleep, EEG exhibits a large amplitude oscillatory pattern with a slow wave activity (SWA, one second long) periodicity. This SWA, known as deep sleep, plays a crucial role in the restorative functions and quality of sleep [55,56]. The deep sleep or SWA is actively discussed in recent publications as the main mechanisms of activation of the drainage and clearing functions of the brain. Indeed, Xie et al. demonstrated that cerebral spinal fluid (CSF) tracer influx into the mouse brain is largely reduced by 95% in the awake state [49]. However, during deep sleep tracer fast moves along the interstitial space and the parenchymal spaces that are increased by 60% compared with the awakesness. Based on the studies with humans Fultz et al. reported the high CSF and hemodynamic oscillation during SWA illustrating a potential bridge between NREM and activation of the drainage function of the brain [48]. These findings hint a potential bridge between deep sleep and activation of the repair and restorative functions of the cerebral lymphatics. Many studies have shown that the methods for an enhance of SWA demonstrate the efficacy for therapy of such serious neurodegenerative diseases such as AD [57], schizophrenia [58], and also in normal aging process [59]. The effectiveness of SWA enhancement for improvement of verbal declarative memory [60], object location memory [61], and picture memory [62] has been shown in several human studies.

Taken together the facts about the crucial function of deep sleep (SWA) in the drainage and clearing functions of the brain as well as about PS-mediated effects on MLVs, we hypothesize that PS-stimulation of the lymphatic drainage and clearance during deep sleep might be a promising tool for clearance of toxins such as A β , red blood cells (RBSs), and waste products from the brain (see Figure 1).

This work was supported by RF Governmental Grant № 075-15-2019-1885, Grant from RSF № 20-15-00090 and 19-15-00201, Grant from RFBR 19-515-55016 China a, 20-015-00308-a.

References

- [1] Zinchenko, E. et al. *Biomedical optics express* 2019, 10, 4003–4017.
- [2] Lu, Y. et al. *Neurobiology of aging* 2017, 49, 165–182.
- [3] Grillo, S. et al. *Journal of Photochemistry and Photobiology B: Biology* 2013, 123, 13–22.
- [4] Purushothuman, S. et al. *Neuroscience letters* 2015, 155–159.
- [5] Luz Eltchechem, C. et al. *Lasers in medical science* 2017, 32, 749–756.
- [6] Oron, A. et al. *Photomedicine and laser surgery* 2016, 34, 627–630.
- [7] Farfara, D. et al. *Journal of Molecular Neuroscience* 2015, 55, 430–436.
- [8] Chang, J. et al. *Neuropsychiatry* 2018, 8, 477–483.
- [9] Hamblin, M.R. *Journal of neuroscience research* 2018, 96, 731–743.
- [10] Salehpour, F. et al. *Molecular neurobiology* 2018, 55, 6601–6636.
- [11] Cassano, P. et al. *Psychiatry journal*, 2015:352979.
- [12] Xu, Z. *Molecular neurobiology* 2017, 54, 4551–4559.
- [13] Mohammed, H.S. *Lasers in medical science* 2016, 31, 1651–1656.
- [14] Purushothuman, S. et al. *Brain research* 2013, 1535, 61–70.
- [15] Huisa, B.N. et al. *Journal of Stroke* 2013, 8, 315–320.
- [16] Lapchak, P.A. et al. Transcranial near-infrared laser therapy for stroke: how to recover from futility 583 in the NEST-3 clinical trial. In *Brain Edema XVI*; Springer, 2016; pp. 7–12.
- [17] Xuan, W. et al. *Journal of biophotonics* 2015, 8, 502–511.
- [18] Morries, L.D. et al. *Neuropsychiatric disease and treatment* 2015, 11, 2159.
- [19] Smoot, B. et al. *Journal of Cancer Survivorship* 2015, 9, 287–304.
- [20] Dirican, A. et al. *Supportive care in cancer* 2011, 19, 685–690.
- [21] Landucci, A. et al. *International journal of oral and maxillofacial surgery* 2016, 45, 392–398.
- [22] Markovic, A. et al. *International journal of oral and maxillofacial surgery* 2007, 36, 226–229.
- [23] Mester, E. et al. *Kiserl Orvostud* 1967, 19, 628.
- [24] Mester, E. et al. *The American Journal of Surgery* 1971, 122, 532–535.
- [25] Hamblin, M.R. *Low-Level Light Therapy*; Society of Photo-Optical Instrumentation Engineers (SPIE), 2018.
- [26] Semyachkina-glushkovskaya, O. et al. *Biomedical Optics Express* 2020, 11, 725–734.
- [27] Semyachkina-Glushkovskaya, O. et al. *Translational Biophotonics*, n/a, e201900036, [<https://www.onlinelibrary.wiley.com/doi/pdf/10.1002/tbio.201900036>]. doi:10.1002/tbio.201900036.
- [28] Scallan, J.P. et al. *The Journal of physiology* 2010, 588, 243–254.
- [29] Kuan, E.L. et al. *The Journal of Immunology* 2015, 194, 5200–5210.
- [30] Harvey, N.L. *Annals of the New York Academy of Sciences* 2008, 1131, 82–88.
- [31] Banerji, S. et al. *The Journal of cell biology* 1999, 144, 789–801.
- [32] Jackson, D.G. *Trends in cardiovascular medicine* 2003, 13, 1–7.
- [33] Jackson, D.G. et al. *Trends in immunology* 2001, 22, 317–321.
- [34] Liao, S. et al. *Seminars in cell & developmental biology*. Elsevier, 2015, Vol. 38, pp. 83–89.
- [35] Gashev, A.A. et al. *The Journal of physiology* 2002, 540, 1023–1037.
- [36] Elias, R. et al. *Journal of applied physiology* 1990, 68, 199–208.
- [37] Ferguson, M.K. et al. *Microvascular research* 1994, 47, 308–317.
- [38] Shirasawa, Y. et al. *American Journal of Physiology-Gastrointestinal and Liver Physiology* 2000, 278, G551–G556.
- [39] Von der Weid, P. et al. *The Journal of physiology* 1996, 493, 563–575.
- [40] Yokoyama, S. et al. *American Journal of Physiology-Heart and Circulatory Physiology* 1993, 264, H1460–H1464.

- [41] Gasheva, O.Y. et al. *The Journal of physiology* 2006, 821–832.
- [42] Hagendoorn, J. et al. *Circulation research* 2004, 95, 204–209.
- [43] Liao, S. et al. *Proceedings of the National Academy of Sciences* 2011, 108, 18784–18789.
- [44] Bohlen, H.G. et al. *American Journal of Physiology-Heart and Circulatory Physiology* 2009, 297, H1319–H1328.
- [45] Bohlen, H.G. et al. *American Journal of Physiology-Heart and Circulatory Physiology* 2009, 297, H1337–H1346.
- [46] Bohlen, H.G. et al. *American Journal of Physiology-Heart and Circulatory Physiology* 2011, 301, H1897–H1906.
- [47] Papachristou, C.S. *Electronic Journal of Philosophy* 2014, 17, 1–47.
- [48] Fultz, N.E. et al. *Science* 2019, 366, 628–631.
- [49] Xie, L. et al. *Science* 2013, 342, 373–377.
- [50] Cirrito, J.R. et al. *Neuron* 2005, 48, 913–922.
- [51] Yamada, K. et al. *Journal of Neuroscience* 2011, 31, 13110–13117.
- [52] Holth, J.K. et al. *Science* 2019, 363, 880–884.
- [53] Shokri-Kojori, E. et al. *Proceedings of the National Academy of Sciences USA* 2018, 115, 4483–4488.
- [54] Kang, J.E. et al. *Science* 2009, 326, 1005–1007.
- [55] Huber, R. et al. *Nature neuroscience* 2013, 16, 1553.
- [56] Keklund, G. et al. *Journal of sleep research* 1997, 6, 217–220.
- [57] Moe, K.E. et al. *Journal of sleep research* 1995, 4, 15–20.
- [58] Göder, R. et al. *Journal of psychiatric research* 2004, 38, 591–599.
- [59] Scullin, M.K. *Psychology and aging* 2013, 28, 105.
- [60] Ngo, H.V.V. et al. *Neuron* 2013, 78, 545–553.
- [61] Prehn-Kristensen, A. et al. *Brain stimulation* 2014, 7, 793–799.
- [62] Ladenbauer, J. et al. *Neuroimage* 2016, 142, 311–323.

TISSUE OPTICAL CLEARING: FROM *IN VITRO* TO *IN VIVO*DAN ZHU^{1,2}¹*Britton Chance Center for Biomedical Photonics, Wuhan National Laboratory for Optoelectronics, Huazhong University of Science and Technology, China*²*MoE Key Laboratory for Biomedical Photonics, Huazhong University of Science and Technology, China*

dawnzh@mail.hust.edu.cn

Abstract

Biomedical photonics is currently one of the fastest growing fields of life sciences, which allows structural and functional analysis of tissues with high resolution and contrast unattainable by any other method [1-3]. However, the high scattering of turbid biological tissues limits the penetration of light, leading to strongly decreased imaging resolution and contrast as light propagates deeper into the tissue [4, 5]. Fortunately, novel tissue optical clearing technique could reduce the scattering of tissue and make it transparent for higher optical imaging quality [6-9]. This presentation will introduce the recently developed *in vitro* optical clearing methods for whole organs imaging, including FDISCO and MACS [10, 11]. And then I will demonstrate *in vivo* skull/skin optical clearing window for imaging structural and functional of cutaneous / cortical vascular and cells, also manipulating cortical vasculature [12-14].

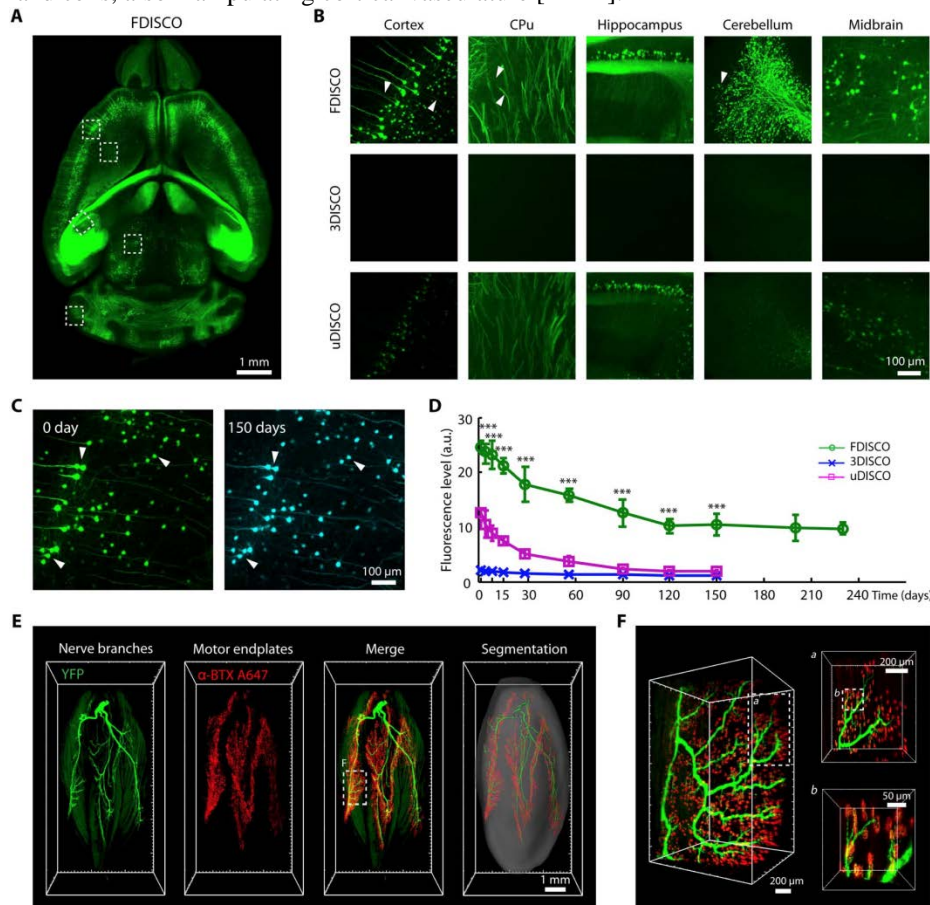


Figure 1: LSFM imaging of neural structures in the mouse brain and gastrocnemius muscle after FDISCO clearing. (A) Image of the whole brain (*Thy1-GFP-M*) cleared by FDISCO. (B) Comparison of the high-magnification images of the cleared brains assessed immediately after FDISCO, 3DISCO, and uDISCO clearing. The white arrowheads mark the tiny nerve fibers detected. For different clearing methods, the same imaging parameters and image processing methods were used for the same regions. (C) Images of cortical neurons in the FDISCO-cleared brain taken at 0 and 150 days after clearing, respectively. The neurons (e.g., white arrowheads) could still be viewed well after 150 days. (D) Fluorescence level quantification of cleared brains over time after FDISCO, 3DISCO, and uDISCO clearing ($n = 4, 3,$ and $3,$ respectively). (E) 3D reconstruction and segmentation of nerve branches (green) and motor endplates (red) of the gastrocnemius muscle (*Thy1-YFP-16*) cleared by FDISCO. (F) High-magnification images of the dashed boxed region in (E). [10]

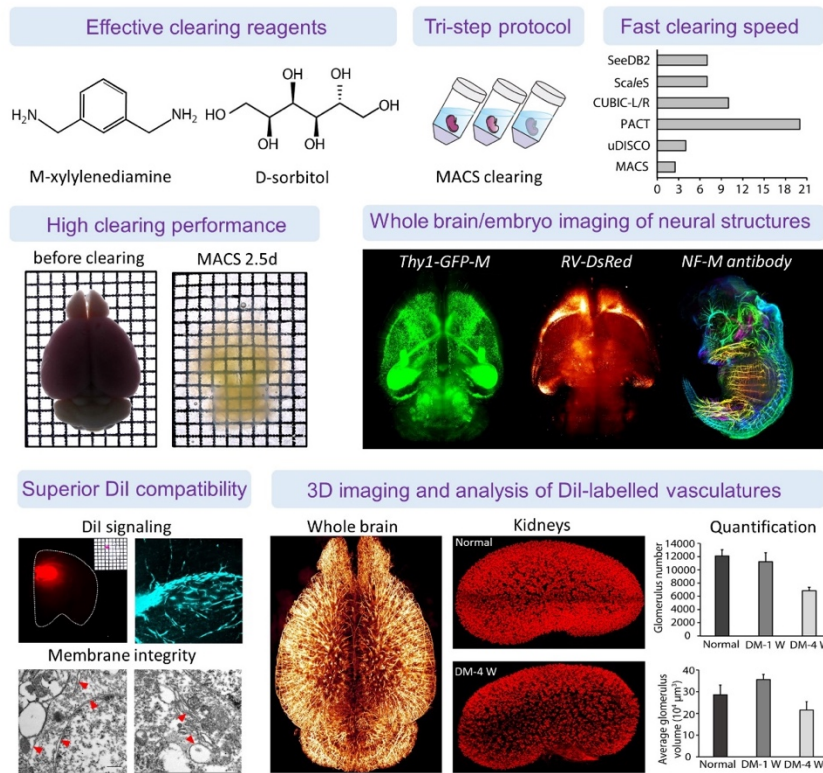


Figure 2: MACS for imaging various organs and embryo of neural structures and function [11].

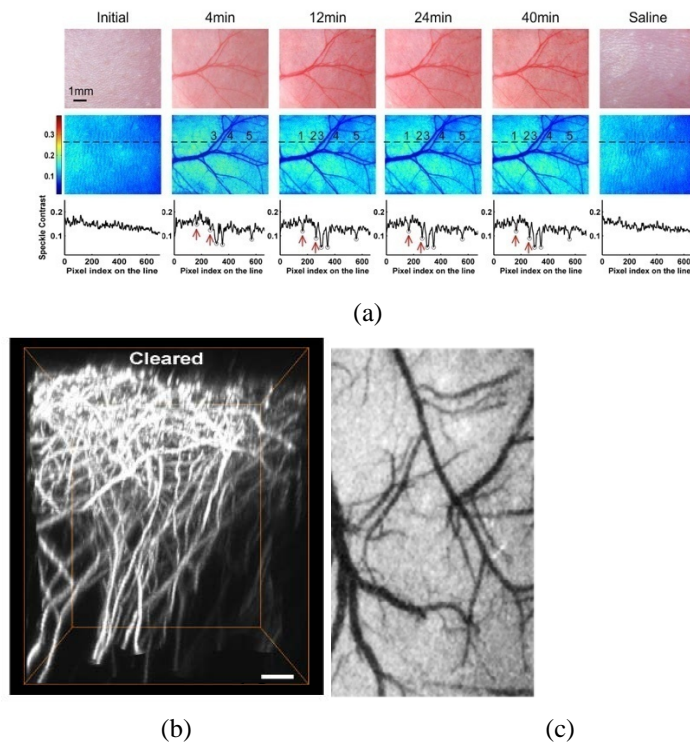


Figure 3: (a) In vivo skin optical clearing for blood flow imaging[15]; (b) in vivo skull optical clearing for cortical neural imaging and (c) cortical vascular functional imaging [12, 13, 15].

References

- [1] K. H. Wang et al., In vivo two-photon imaging reveals a role of arc in enhancing orientation specificity in visual cortex, Cell,126(2), 389-402, 2006.
- [2] N. Wagner et al., Instantaneous isotropic volumetric imaging of fast biological processes, Nature Methods,K. H. Wang et al., In vivo two-photon imaging reveals a role of arc in enhancing orientation specificity in visual cortex, Cell 126(2), 389-402, 2006.
- [2] N. Wagner et al., Instantaneous isotropic volumetric imaging of fast biological processes, Nature Methods 16(6), 497, 2019.
- [3] R. Prevedel et al., Fast volumetric calcium imaging across multiple cortical layers using sculpted light, Nature Methods 13(12), 1021-1028, 2016.

- [4] M. Kneipp et al., Effects of the murine skull in optoacoustic brain microscopy, *Journal of Biophotonics* 9(1-2), 117-123, 2016.
- [5] X. F. Fan, W. T. Zheng, and D. J. Singh, Light scattering and surface plasmons on small spherical particles, *Light-Science & Applications* 3, e179, 2014.
- [6] T. Yu et al., Optical clearing for multiscale biological tissues, *Journal of Biophotonics* 11(2), e201700187, 2018.
- [7] R. Cai et al., Panoptic imaging of transparent mice reveals whole-body neuronal projections and skull–meninges connections, *Nature Neuroscience* 22(2), 317-327, 2019.
- [8] M. Belle et al., Tridimensional visualization and analysis of early human development, *Cell* 169(1), 161-173 e112, 2017.
- [9] H. M. Lai et al., Next generation histology methods for three-dimensional imaging of fresh and archival human brain tissues, *Nature Communications* 9(1), 2018.
- [10] Y. Qi et al., FDISCO: Advanced solvent-based clearing method for imaging whole organs, *Science Advances* 5(1), eaau8355-eaau8355, 2019.
- [11] J. T. Zhu et al., MACS: Rapid Aqueous Clearing System for 3D Mapping of Intact Organs, *Advanced Science* 7(8), 2020.
- [12] Y. J. Zhao et al., Skull optical clearing window for in vivo imaging of the mouse cortex at synaptic resolution, *Light-Science & Applications* 7(2), 17153, 2018.
- [13] C. Zhang et al., Age differences in photodynamic therapy-mediated opening of the blood-brain barrier through the optical clearing skull window in mice, *Lasers in Surgery and Medicine* 51(7), 625-633, 2019.
- [14] W. Feng et al., Comparison of cerebral and cutaneous microvascular dysfunction with the development of type 1 diabetes, *Theranostics* 9(20), 5854-5868, 2019.
- [15] D. Zhu et al., Imaging dermal blood flow through the intact rat skin with an optical clearing method, *J. Biomed. Opt.* 15(2), 026008, 2010.
- 16(6), 497, 2019.
- [3] R. Prevedel et al., Fast volumetric calcium imaging across multiple cortical layers using sculpted light, *Nature Methods*,13(12), 1021-1028, 2016.
- [4] M. Kneipp et al., Effects of the murine skull in optoacoustic brain microscopy, *Journal of Biophotonics*,9(1-2), 117-123, 2016.
- [5] X. F. Fan, W. T. Zheng, and D. J. Singh, Light scattering and surface plasmons on small spherical particles, *Light-Science & Applications*,3, e179, 2014.
- [6] T. Yu et al., Optical clearing for multiscale biological tissues, *Journal of Biophotonics*,11(2), e201700187, 2018.
- [7] R. Cai et al., Panoptic imaging of transparent mice reveals whole-body neuronal projections and skull–meninges connections, *Nature Neuroscience*,22(2), 317-327, 2019.
- [8] M. Belle et al., Tridimensional Visualization and Analysis of Early Human Development, *Cell*,169(1), 161-173 e112, 2017.
- [9] H. M. Lai et al., Next generation histology methods for three-dimensional imaging of fresh and archival human brain tissues, *Nature Communications*,9(1), 2018.
- [10] Y. Qi et al., FDISCO: Advanced solvent-based clearing method for imaging whole organs, *Science advances*,5(1), eaau8355-eaau8355, 2019.
- [11] J. T. Zhu et al., MACS: Rapid Aqueous Clearing System for 3D Mapping of Intact Organs, *Advanced Science*,7(8), 2020.
- [12] Y. J. Zhao et al., Skull optical clearing window for in vivo imaging of the mouse cortex at synaptic resolution, *Light-Science & Applications*,7(2), 17153, 2018.
- [13] C. Zhang et al., Age differences in photodynamic therapy-mediated opening of the blood-brain barrier through the optical clearing skull window in mice, *Lasers in Surgery and Medicine*,51(7), 625-633, 2019.
- [14] W. Feng et al., Comparison of cerebral and cutaneous microvascular dysfunction with the development of type 1 diabetes, *Theranostics*,9(20), 5854-5868, 2019.
- [15] D. Zhu et al., Imaging dermal blood flow through the intact rat skin with an optical clearing method, *J Biomed Opt*,15(2), 026008, 2010.

A SUPERSTABLE HOMOGENEOUS LIPIODOL-ICG FORMULATION FOR LOCOREGIONAL HEPATOCELLULAR CARCINOMA TREATMENT

HU CHEN, HONGWEI CHENG AND GANG LIU*

State Key Laboratory of Molecular Vaccinology and Molecular Diagnostics & Center for Molecular Imaging and Translational Medicine, School of Public Health, Xiamen University, Xiamen 361102, China

gangliu.cmitm@xmu.edu.cn

Abstract

Accurate identification of surgical margins for malignancy remains a challenge in the surgical therapy of cancer, and this encountered interoperative difficulties which directly contribute to the prognosis of patients. In recent years, indocyanine green (ICG) has been approved and applied in clinical settings for lesions detection, especially for the precise surgical resection. However, rapid clearance and poor stability greatly limit its clinical practicality. Herein, a super-stable homogeneous iodinated formulation technology (SHIFT) is designed to realize sufficient dispersion of ICG into lipiodol (SHIFTs) for fluorescence-guided transcatheter embolization (TAE). Particularly, SHIFTs is prepared in a green physical mixture *via* a carrier-free manner, which possesses controlled morphology, long-term stability, and improved optical characteristics of ICG (fluorescence/photoacoustic/photothermal activities). Furthermore, the viscosity of the synthetic solvent is comparable to lipiodol, and further assessment demonstrated the same efficacy in computed tomography. The performance of SHIFTs in the fluorescence navigation was further evaluated *in vivo* by TAE therapy to the rabbit VX2 tumor model for a two-week monitor. The integration of near-infrared fluorescence surgery navigation and TAE could effectively guarantee the precise resection for hepatocellular carcinoma. This SHIFT system (Figure 1) provides good potentials for ameliorating the dilemma of precise fluorescent navigation for surgical resection after arterial embolization in clinical practice[1,2].

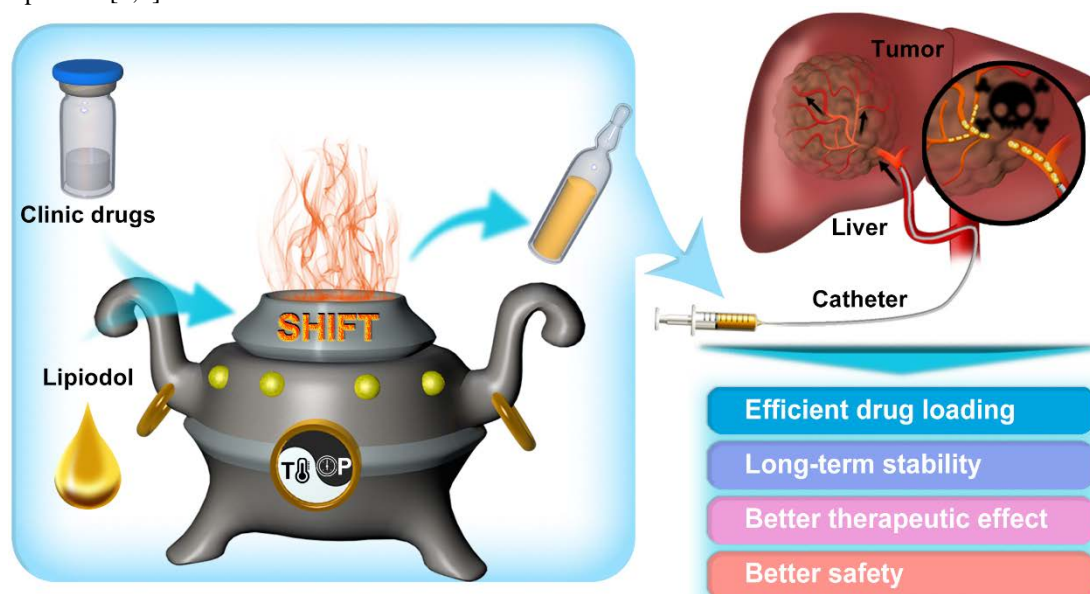


Figure: Schematic illustration of SHIFT as a revolutionary strategy for TACE. The clinic drugs and lipiodol are introduced to develop formulations with SHIFT at a controlled temperature and pressure, overcoming current challenges in the HCC treatment with TACE^[2].

References

- [1] H. Chen, H. Cheng, Q. Dai, et al. A superstable homogeneous lipiodol-ICG formulation for locoregional hepatocellular carcinoma treatment, *J Control Release*. 635-643, 2020.
- [2] H. Cheng, X. Yang, and G. Liu. Superstable homogeneous iodinated formulation technology: Revolutionizing transcatheter arterial chemoembolization, *Sci Bull*. 1685-1687, 2020.

MINING POLARIZATION FEATURES FROM A MUELLER MATRIX

DONG YANG¹, JIACHENWAN² AND HUI MA^{1,3}¹Center for Precision Medicine and Healthcare, Tsinghua-Berkeley Shenzhen Institute, Tsinghua University, China²Department of Applied Physics, New York University, Tandon School of Engineering, USA³Department of Physics, Tsinghua University, China

mahui@tsinghua.edu.cn

Abstract

Recently, polarization technique has found more and more application prospects in the field of biomedicine, with the emergence of new light sources, polarization devices, and detectors, together with a rapid development in data processing and feature mining capability, and a prominent increase in polarization data measurement and interpretation methods. Mueller matrix polarimetry has obvious advantages in exploring the characteristics of complex biomedical specimens [1-4]. Mueller matrix polarization analysis can be realized on other optical technologies by properly adding the polarization state generator and analyzer to the existing optical path in common optical devices, such as Mueller matrix microscopes and endoscopes [5,6]. In addition, Mueller matrix polarization method is more sensitive to the scattering of sub-wavelength microstructure. Compared with the traditional non-polarization optical method, Mueller matrix polarimetry can provide more information to characterize the samples, including the anisotropic optical properties, such as birefringence and diattenuation, as well as the distinctive features of various scattering particles and microstructures. At present, the main challenge of the application of Mueller matrix imaging methods in biomedical research is: how to analyze the obtained polarization data, that is, how to separate and derive specific polarization parameters to characterize target structures and meet the requirements in biomedical detection [7]. In order to break through this bottleneck, our research group has tried to develop a series of polarization feature extraction methods based on machine learning and shown preliminary application prospects in cancer pathological diagnosis.

The process of digitizing the Whole-Slide Images (WSI) of pathological tissues has led to the advent of Machine Learning (ML) tools in digital pathology to help with various tasks [8], including object recognition problems, and predicting disease diagnosis and prognosis of treatment response on patterns in the standard pathological image. Combined with polarimetry technique and data mining methods, we proposed a series of new methods that can derive new polarimetry feature parameters (PFPs) as linear or nonlinear combinations of polarimetry basis parameters (PBPs) to quantitatively and automatically identify the target microstructures in pathological sections, which can be used as a powerful tool in histopathological digitalization and computer-aided diagnosis [9].

In our research work, we took microscopic Mueller matrix images of H&E pathological sections of several typical breast tissues: healthy breast tissue, breast fibroma, breast ductal carcinoma, and breast mucinous carcinoma. Then sets of polarization parameters from Mueller matrix polar decomposition (MMPD) [10] and from our previous studies [7,11,12] were used as the PBPs for input data of training models. Then, a supervised learning method based on linear discriminant analysis (LDA) is used to derive new PFPs based on the polarization characteristics of the target microstructure, which are linear combinations of PBPs. Here, we obtained 12 PFPs to describe the three cancer-related pathological features in each typical breast pathological tissue, i.e. cell nuclei, aligned collagen, and disorganized collagen, as shown in Fig. 1. The training and testing of PFPs were completed in 224 regions of interests (ROIs). By the validation of the PFPs performance with the corresponding H&E images as ground truth, it can be concluded that: (1) the performance of PFPs in identifying the carcinogenesis related microstructures is satisfactory (AUC 0.87-0.94, accuracy 0.82-0.91, precision 0.81-0.95, and recall 0.80-0.98), which has the potential to automate the diagnosis process and predict patient survival and prognosis; (2) PFP is the simplified linear function of the PBPs with physical meanings, providing quantitative characterization for target pathological feature and allowing in-depth analysis of physical interpretation; (3) Benefitting from the advantages of polarization imaging (sensitive to sub-wavelength microstructures and less sensitive to imaging resolution), the outputs PFPs with high sensitivity has the potential to rapidly scan and quantitatively analyze the whole pathological section in the low-resolution and wide-field systems.

On the basis of the previous work, in order to quantitatively characterize more specific microstructures, we designed a neuron network according to the target microstructure characteristics and the corresponding polarization properties, output more complex nonlinear PFPs. Here, we took advantage of Bayesian decision theory and Conditional probability model to find the nonlinear combination from PBPs constrained under the increasing given conditions which correspond to more specific microstructures in breast pathology. The algorithm architecture for deriving nonlinear PFP is shown in Fig. 2. In the previous work, we derived PFP that can characterize all types of cell nuclei in breast tissue, as the simplest linear combination of PBP, denoted as $P(\text{Cell})$ here. In order to further extract the PFP that can characterize the cancerous cell nuclei, we used the Lasso regression method to extract an interim PFP as the linear combination of PBP under the given condition that all pixels are known to be cell denoted as $P(\text{Cancer cell} | \text{Cell})$, aiming to distinguish normal

cell and cancerous cell. According to Bayesian theory, $P(\text{Cell})$ and $P(\text{Cancer cell} | \text{Cell})$ can be multiplied to get a final nonlinear PFP, namely $P(\text{Cancer cell})$, which can quantitatively characterize cancerous cell nuclei from complex breast tissue. Similarly, by continuing to add neurons (each neuron is a conditional probability model), we can separately extract two nonlinear PFPs which has great potential to quantitatively characterize highly differentiated cancerous cancer cells and low-differentiated cancer cells in breast tissues.

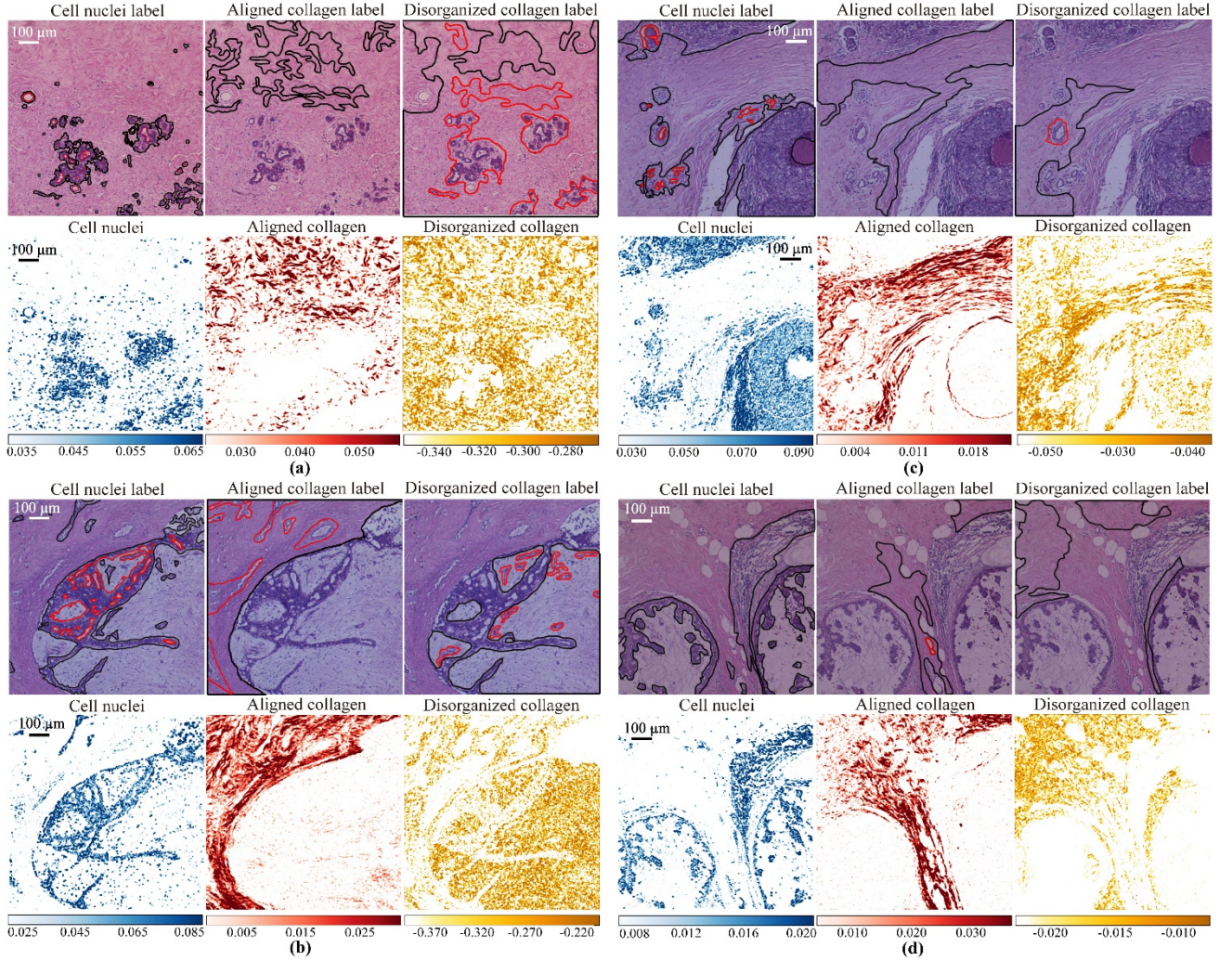


Figure 1: Quantitative characterization of cell nuclei (blue pixels), aligned collagen (red pixels), and disorganized collagen (orange pixels) using the PFPs in H&E pathological sections of different breast tissues: (a) healthy breast tissue; (b) breast fibroma; (c) breast ductal carcinoma; (d) breast mucinous carcinoma. The areas inside the black solid line and outside the red solid line in H&E images are the target microstructural features labelled by the breast pathologist. The image size is 800×800 pixels [9].

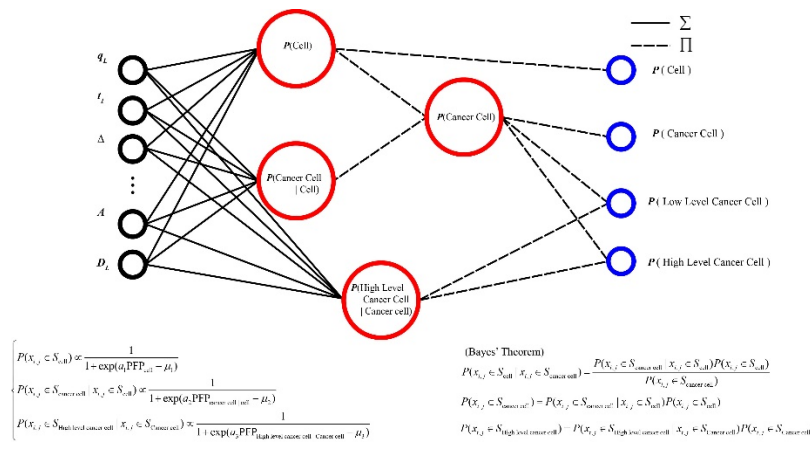


Figure 2: Algorithm architecture for deriving nonlinear PFPs to characterize more specific microstructure feature in breast pathological tissues.

Figure 3 summarizes the characterization results of these nonlinear PFPs derived by the proposed method. The cell nuclei with different pathological states in WSIs were labelled by pathologists under 40× objective manually as ground truth, whereas, PFPs of breast pathological tissues, as the input data of designed ML model, were obtained under 4× objective. From Fig. 3, we can observe that the performance of these PFPs is satisfactory, which has the potential to quantitatively characterize more and more specific microstructures in breast tissues. Each neuron is a probability model composed of PBP according to the pathological structure, which has certain physical interpretability. In addition, in the low-resolution and wide-field systems, the PFPs are more sensitive than human vision to the cancer cells with different degrees of differentiation, and may provide quantitative evaluation for breast cancer diagnosis. This technique paves the way for cancer primary screening in clinical practice.

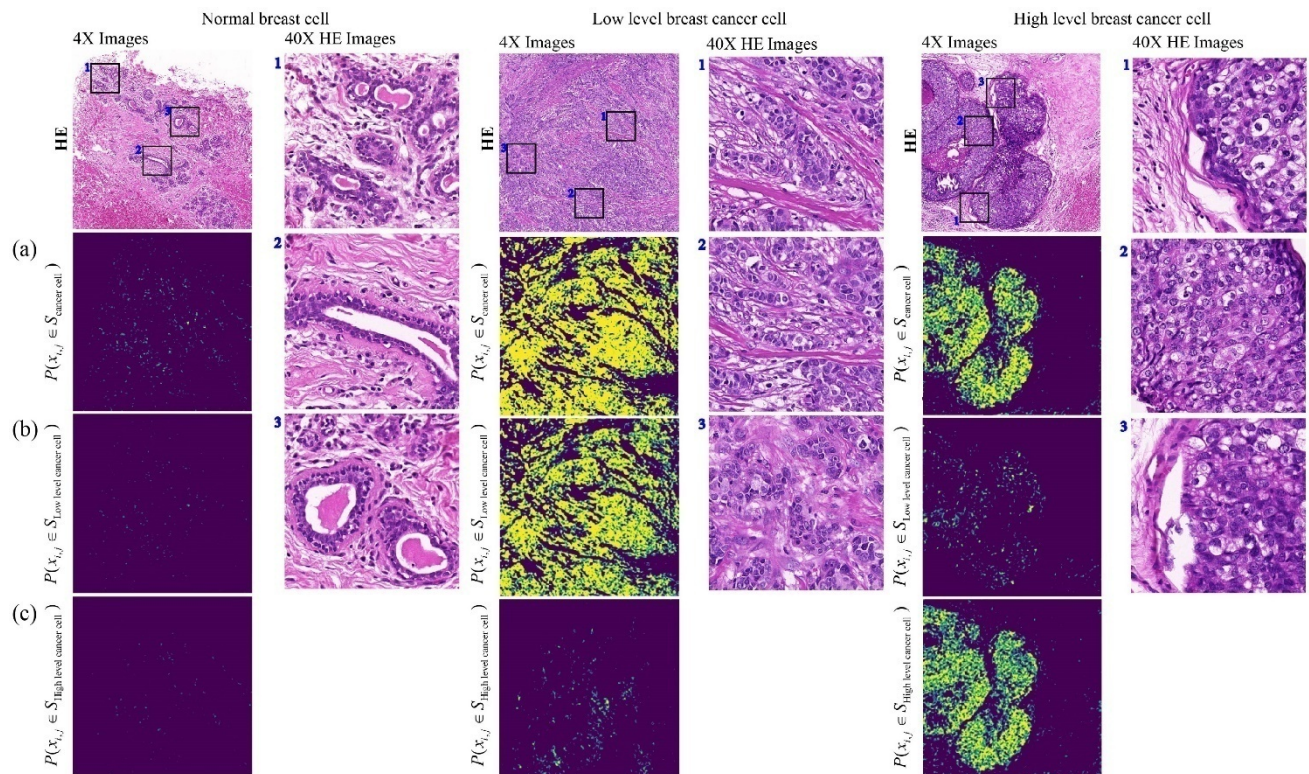


Figure 3: For different breast pathological cells-normal breast cell, low level breast cancer cell, and high level breast cell, the characterization results of nonlinear PFPs: (a) $P(\text{Cancer cell})$; (b) $P(\text{Low level cancer cell})$; (c) $P(\text{High level cancer cell})$.

References

- [1] V.V. Tuchin, Polarized light interaction with tissues, *J. Biomed. Opt.*, vol. 21, no. 7, pp. 071114-1–071114-37, 2016.
- [2] B. Kunnen, C. Macdonald, A. Doronin, S. Jacques, M. Eccles, and I. Meglinski, Application of circularly polarized light for non-invasive diagnosis of cancerous tissues and turbid tissue-like scattering media, *J. Biophotonics*, vol. 8, no. 4, pp. 317–323, 2015.
- [3] N. Ghosh and I. A. Vitkin, Tissue polarimetry: Concepts, challenges, applications, and outlook, *J. Biomed. Opt.*, vol. 16, no. 11, pp. 110801- 1–110801-29, 2011.
- [4] V. V. Tuchin, L. Wang, and D. A. Zimnyakov. *Optical polarization in biomedical applications*. Berlin, Germany: Springer-Verlag, 2006.
- [5] Y. Wang *et al.*, Differentiating characteristic microstructural features of cancerous tissues using Mueller matrix microscope, *Micron*, vol. 79, pp. 8–15, 2015.
- [6] J. Qi and D. S. Elson, Mueller polarimetric imaging for surgical and diagnostic applications: A review, *J. Biophotonics*, vol. 10, no. 8, pp. 950–982, 2017.
- [7] H. He *et al.*, Emerging New Tool for characterizing the microstructural feature of complex biological specimen, *J. Lightwave Technol.*, vol. 37, no. 11, pp. 2534–2548, 2019.
- [8] K. Bera *et al.*, Artificial intelligence in digital pathology-new tools for diagnosis and precision oncology, *Nat. Rev. Clin. Oncol.*, vol. 16, no. 3, pp. 703–715, 2019.
- [9] Y. Dong *et al.*, Deriving polarimetry feature parameters to characterize microstructural features in histological sections of breast tissues, *IEEE Trans. Biomed. Eng.*, doi:10.1109/TBME.2020.3019755, 2020.
- [10] S. Y. Lu and R. A. Chipman, Interpretation of Mueller matrices based on polar decomposition, *J. Opt. Soc. Amer. A*, vol. 13, no. 5, pp. 1106–1113, 1996.
- [11] P. Li, D. Lv, H. He, and H. Ma, Separating azimuthal orientation dependence in polarization measurements of anisotropic media, *Opt. Express*, vol. 26, no. 4, pp. 3791–3800, 2018.
- [12] H. He *et al.*, A possible quantitative Mueller matrix transformation technique for anisotropic scattering media, *Photon. Lasers Med.*, vol. 2, no. 2, pp. 129–137, 2013.

GAP-ENHANCED RESONANCE RAMAN TAGS FOR BIOIMAGING

JIAN YE

School of Biomedical Engineering, Shanghai Jiao Tong University, P.R. China

yejian78@sjtu.edu.cn

Abstract

Gap-enhanced Raman tags (GERTs) are emerging probes of surface-enhanced Raman scattering (SERS) spectroscopy that have found promising analytical, bioimaging, and theranostic applications [1-5]. Because of their internal location, Raman reporter molecules are protected from unwanted external environments and particle aggregation and demonstrate superior SERS responses owing to the strongly enhanced electromagnetic fields in the gaps between metal core-shell structures. However, long-term live-cell Raman bioimaging is limited due to the photodamage from a relatively long exposure time and a high laser power, which are needed for acquiring detectable Raman signals.

In this talk, we will briefly discuss recent progress in the synthesis, simulation, and experimental studies of the optical properties and biomedical applications of novel spherically symmetrical and anisotropic GERTs fabricated with common plasmonic metals—gold (Au) and silver (Ag). Next, we attempt to resolve this photodamage issue by developing ultrabright gap-enhanced resonance Raman tags (GERRTs), consisting of the petal-like Au core and Ag shell with near-infrared resonant reporters of IR-780 embedded in between, for long-term and high-speed live-cell imaging [6]. GERRTs exhibit the ultrahigh Raman intensity down to a single-nanoparticle level in the aqueous solution and solid state upon 785 nm excitation, allowing for high-resolution time-lapse live-cell Raman imaging with an exposure time of 1 ms per pixel and a laser power of 50 μ W. Under this measurement condition, we can possibly capture dynamic cellular processes with a high temporal resolution, and track living cells for long periods of time owing to the reduced photodamage to cells. These nanotags open new opportunities for ultrasensitive, low-phototoxic, and long-term live-cell imaging.

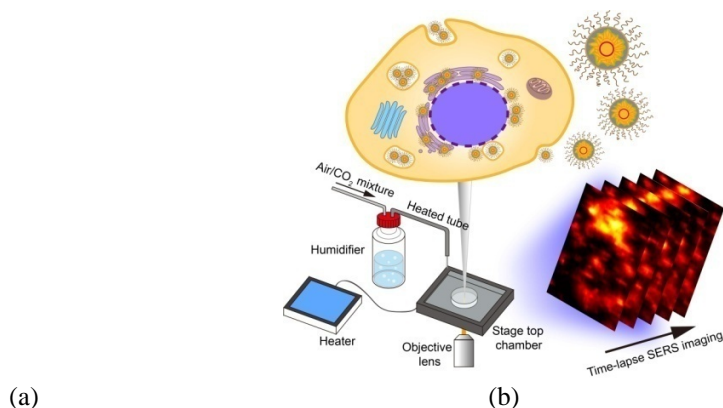


Figure: (a) Scheme of a GERRT, and (b) GERRTs-based live cell bioimaging;

References

- [1] L. Lin, M. Zapata, M. Xiong, Z. Liu, S. Wang, H. Xu, A. G. Borisov, H. Gu, P. Nordlander, J. Aizpurua, J. Ye. Nanooptics of plasmonic nanomatryoshkas: shrinking the size of a core-shell junction to subnanometer, *Nano Letters*, 15, 6419-6428, 2015
- [2] Z. Bao, Y. Zhang, Z. Tan, X. Yin, W. Di, J. Ye. Gap-enhanced Raman tags for high-contrast sentinel lymph node imaging, *Biomaterials*, 163, 105-115, 2018.
- [3] Y. Qiu, Y. Zhang, M. Li, G. Chen, C. Fan, K. Cui, J. Wan, A. Han, J. Ye, Z. Xiao, Intraoperative Detection and Eradication of Residual Microtumors with Gap-Enhanced Raman Tags, *ACS Nano*, 12, 7974-7985, 2018.
- [4] Y. Zhang, Y. Gu, J. He, B. D. Thackray, J. Ye. Ultrabright gap-enhanced Raman tags for high-speed bioimaging, *Nature Communications*, 10, 3905, 2019.
- [5] Y. Gu, C. He, Y. Zhang, L. Lin, B. D. Thackray, J. Ye. Gap-enhanced Raman tags for physically unclonable anticounterfeiting labels, *Nature Communications*, 11, 516, 2020.
- [6] Y. Gu, X. Bi, J. Ye. Gap-enhanced resonance Raman tags for live-cell imaging, *J. of Mater. Chem. B*, 8, 6944-6955, 2020

DYNAMIC-RANGE COMPRESSION AND CONTRAST ENHANCEMENT IN SWEEP SOURCE OPTICAL COHERENCE TOMOGRAPHY

SHANSHAN LIANG¹, XINYU LI¹, YAO QIN¹ AND JUN ZHANG¹

¹*School of Electronics and Information Technology, Sun Yat-Sen University, China*

zhangj266@mail.sysu.edu.cn

Abstract

Optical coherence tomography(OCT) has been widely used in clinical applications. Using the Fourier domain technique based on a high speed wavelength swept source, swept source OCT (SSOCT) has increasingly gained attention for its relatively simple system structure and high imaging speed [1].In spite of all the advantages of SSOCT, there are still some impediments that hinder the application in clinic. Since the light strongly attenuates in biological tissues, the image quality of optical coherence tomography (OCT) decreases rapidly with imaging depth. Numerical methods have been reported to compensate for the signal decay based on analysis of OCT signals [2-5] to increase the contrast and quality of deep tissue image. However, considering that the commonly used analog to digital converter of an SSOCT system is hard to fulfil the wide range of the backscattered OCT signal [6], weak light signal from deep tissue might be embedded in the quantization noise of the analog to digital converter. Hence, the numerical methods cannot digitally recover the weak signals submerged in the background noise.

In this paper, we designed and used a frequency gain compensation amplifier to amplify the electrical signal from a photodetector and compensate for the signal attenuation in swept source OCT. With this amplifier, we can compress the dynamic range of the detected signal for superior analog to digital conversion and image display capability.

As illustrated in Fig. 1(A), (C) and (E), the signal intensity and the contrast of the OCT image decay with increasing depth resulting in low visibility in deep tissue. While the OCT images after compensation present an improved visibility of the deep structure and a more uniform contrast through the image as shown in Fig. 1(B), (D), and (F), demonstrating that this cost-efficient technique can effectively enhance the contrast of the deep tissue image.

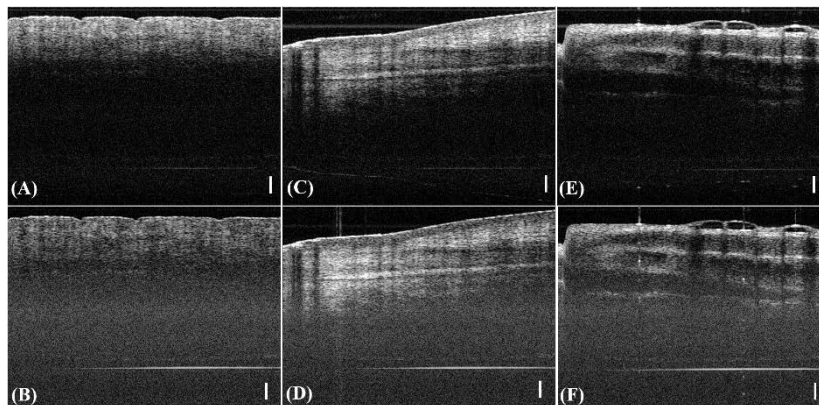


Figure: OCT images of human skin without (A) and with (B) compensation, a fingernail without (C) and with (D) compensation, a pig trachea without (E) and with (F) compensation. (scale bar: 500 μm)

References

- [1] Huo T, Wang C, Zhang X, et al., Ultrahigh-speed optical coherence tomography utilizing all-optical 40 MHz swept-source, *Journal of Biomedical Optics*, 20(3):030503, 2015.
- [2] Chang S, Flueraru C, Mao Y, et al. Attenuation compensation for optical coherence tomography imaging, *Optics Communications*, 282(23):4503-4507, 2009.
- [3] Girard M J A, Strouthidis N G, Ethier C R, et al., Shadow Removal and Contrast Enhancement in Optical Coherence Tomography Images of the Human Optic Nerve Head, *Investigative Ophthalmology & Visual Science*, 52(10):7738, 2011.
- [4] Hojjatoleslami A, Avanaki M R N., OCT skin image enhancement through attenuation compensation, *Applied Optics*, 51(21):4927-4935, 2012.
- [5] Lars, Thrane, Michael, et al., Extraction of optical scattering parameters and attenuation compensation in optical coherence tomography images of multilayered tissue structures, *Optics letters*, 29(14): 1641-1643, 2004.
- [6] Li X, Liang S, Zhang J., Correction of saturation effects in endoscopic swept-source optical coherence tomography based on dual-channel detection, *Journal of Biomedical Optics*, 23(3):1, 2018.

MULTISCALE PHOTOACOUSTIC MICROSCOPY

LEI XI

Department of Biomedical Engineering, Southern University of Science and Technology, Shenzhen, China

xilei@sustc.edu.cn

Abstract

Photoacoustic microscopy (PAM), benefiting from rich optical contrast, scalable acoustic resolution and deep penetration depth, is of great importance for the fields of biology and medicine. The introduction of new scanning devices/mechanisms and fast pulsed lasers enables high spatiotemporal resolution and compact configuration. However, limited by the size and performance of reported optical/acoustic scanners, existing PAMs are bulky, heavy, and suffer from low imaging quality/speed. In this talk, I will present a multiscale photoacoustic microscopic platform consisting of large-field-of-view PAM, portable PAM, handheld PAM and endoscopic PAM, which are capable of meeting various requirements of both fundamental and clinical studies.

References

- [1] Q. Chen, H. Xie, L. Xi, Wearable Optical Resolution Photoacoustic Microscopy, *J. of Biophotonics* 12, e201900066, 2019.
- [2] Q. Chen, H. Guo, T. Jin, W. Qi, H. Xie, L. Xi, Ultracompact high-resolution photoacoustic microscopy, *Opt. Lett.* 43, 1615-1618, 2018.
- [3] W. Qin, T. Jin, H. Guo, L. Xi, Large-field-of-view optical resolution photoacoustic microscopy, *Opt. Express*, 26, 4271-4278, 2018.
- [4] H. Guo, C. Song, H. Xie, L. Xi, Photoacoustic endomicroscopy based on a MEMS scanning mirror, *Opt. Lett.*, 42, 4615-4618, 2017.
- [5] T. Jin, H. Guo, H. Jiang, B. Ke, L. Xi, Portable optical resolution photoacoustic microscopy (pORPAM) for human oral imaging, *Opt. Lett.*, 42, 4434-4437, 2018.

OPTICAL MICROENDOSCOPY AND ITS APPLICATIONS

LING FU^{1,2}¹ Britton Chance Center for Biomedical Photonics, Wuhan National Laboratory for Optoelectronics-Huazhong University of Science and Technology, China² MoE Key Laboratory for Biomedical Photonics, School of Engineering Sciences, Huazhong University of Science and Technology, China

lfu@hust.edu.cn

Abstract

Optical microscope is one of the most basic optical instruments and has been successfully applied to many fields. The related research has won three Nobel Prizes in modern times, covering physics and chemistry. How to use novel optical microscopy to carry out high-resolution visual monitoring inside living organisms has always been a goal pursued by optical imaging and biomedical researchers. In this talk, the recent development of optical microendoscopy in my group will be presented. The talk will introduce two unique core devices: PZT-based fiber scanner and micro-objective lens used in optical fiber confocal microscope, and explain the principles of them, as well as the first domestic medical confocal endoscopic instrument that can realize real-time visualization of mucosal cells of the human digestive tract; present the applications of microendoscopy. The developed instrument has been applied to the clinical diagnosis and treatment of gastric diseases, and its technical transformation has been applied to study brain functions (rewards, memory circuit for place navigation, etc.) shown in Fig. 1.

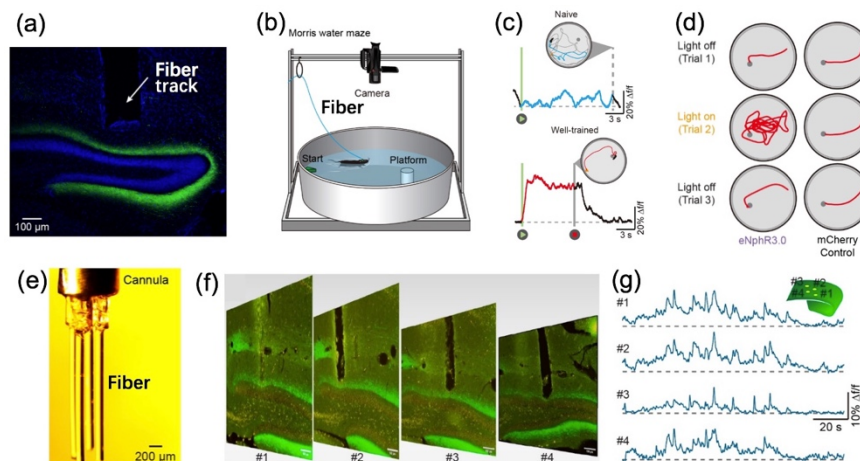


Figure 1: A high sensitivity fiber photometry for axon terminal calcium signal recording. (a) The GCaMP5G virus labeled the MECII-DG circuit and measured calcium signals with optical fibers above its axon terminals; (b) Schematic of the Morris water maze navigation task; (c) During the learning process of water maze task, the calcium signal amplitude of mouse MECII-DG circuit increased and finally presented continuous activity; (d) Impairment of place navigation by photoinhibition of the MECII-DG projection activity; (e) Photograph showing the four-channel fiber probe which was arrayed into a form of square; (f) Post hoc histology after multichannel fiber recording showing the recording positions of four fibers in MECII-DG axon terminals; (g) Example showing Ca^{2+} signals of four individual channels in MECII-DG projection during freely exploring.

References

- [1] Ying Wang[#], Zhi Li[#], Xiaobao Liang, Ling Fu^{*}, Four-plate piezoelectric actuator driving a large-diameter special optical fiber for nonlinear optical microendoscopy, *Optics Express*, 2016, 24(17): 19949-19960
- [2] Li Yang, Jiafu Wang, Geng Tian, Jing Yuan, Qian Liu, Ling Fu^{*}, Five-lens, easy-to-implement miniature objective for a fluorescence confocal microendoscope, *Optics Express*, 2016, 24(1): 473-484
- [3] Jiafu Wang, Min Yang, Li Yang, Yun Zhang, Jing Yuan, Qian Liu, Xiaohua Hou, Ling Fu^{*}, A confocal endoscope for cellular imaging, *Engineering*, 2015, 1(3): 351-360
- [4] Han Qin[#], Ling Fu^{#, *}, Bo Hu[#], Xiang Liao, Jian Lu, Wenjing He, Shanshan Liang, Kuan Zhang, Ruijie Li, Jiwei Yao, Junan Yan, Hao Chen, Hongbo Jia, Benedikt Zott, Arthur Konnerth^{*}, and Xiaowei Chen^{*}, A Visual-Cue-Dependent Memory Circuit for Place Navigation, *Neuron*, 2018, 99:1-9
- [5] Han Qin, Jian Lu, Wenjun Jin, Xiaowei Chen, Ling Fu^{*}, Multichannel fiber photometry for mapping axonal terminal activity in a restricted brain region in freely moving mice, *Neurophotonics*, 2019, 6(3): 03501

BIOMEDICAL APPLICATIONS OF NONLINEAR OPTICAL MICROIMAGING TECHNIQUES

SHIQI WANG¹, FANGRUI LIN¹, SHENG REN¹, YIHUA ZHAO¹ AND LIWEI LIU^{1*}

1Key Laboratory of Optoelectronic Devices and Systems of Ministry of Education & Guangdong Province, College of Physics and Optoelectronic Engineering, Shenzhen University, China.

*E-mail: liulw@szu.edu.cn

Abstract

Optical microscopy imaging technology is a research hotspot in the field of biomedical photonics. In the past two decades, optical microscopy imaging technology has developed very rapidly, constantly breaking through the traditional limits, and increasingly used in the research on subcellular, cellular, tissue and in vivo imaging research, providing a unique perspective for real-time dynamic observation of life systems and solving many key scientific issues in the field of "biomedical photonics".

Our research group has carried out many years of basic application research of nonlinear optical microscopy imaging technology in biomedicine, covering Two-photon Excitation Fluorescence(TPF), Second-Harmonic Generation(SHG), and Stimulated Raman Scattering(SRS) at different levels of molecules, cells, tissues, and living bodies. These optical imaging technologies provide powerful technical support for the monitoring of the microenvironment during tumor treatment. With the help of mature optical microscopic imaging technology, the clinical progress of qualitative and quantitative analysis of the microenvironment during tumor treatment can be promoted.

Tumor microenvironment refers to the internal and external environment in which tumors occur, grow and metastasize. The relationship between tumor microenvironment and tumor is called "seed and soil". In the process of tumor diagnosis and treatment, tumor microenvironment plays a vital role. Therefore, imaging monitoring of the tumor microenvironment has become an assessment method in the process of tumor treatment.

This report mainly introduces the research work of non-linear optical microscopy imaging technology in tumor microenvironment imaging carried out by our team recently, including tumor metastasis path, intracellular calcium ion regulation, etc.

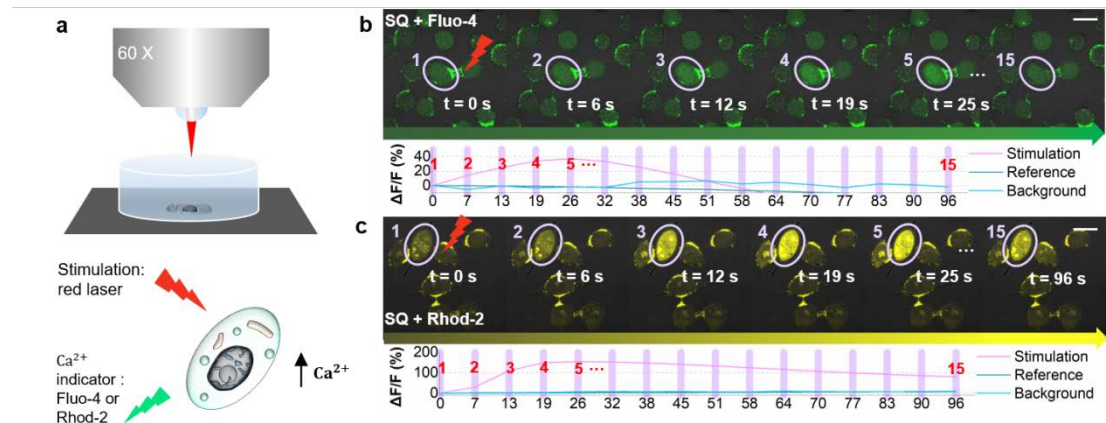


Figure 1: Specific laser and dye were required for LIDSICA. (a) Cells in a Petri dish were stimulated by a 640 nm laser, and the Ca^{2+} levels were indicated by a 488 nm (for Fluo-4) or 561 nm (for Rhod-2) laser via a 60 \times objective. (b, c) OV3 cells stimulated 15 \times in 100 s showed a Ca^{2+} rise of $\sim 37\%$ (green, indicated by Fluo-4) (b) or of $\sim 155\%$ (yellow, indicated by Rhod-2 in another cell) (c).

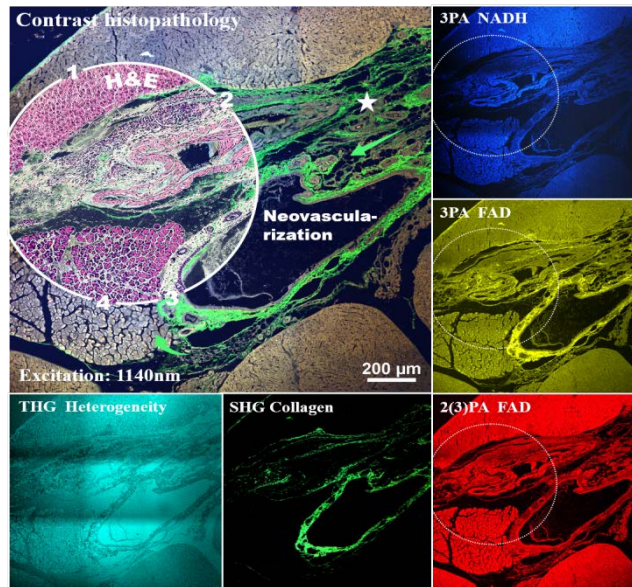
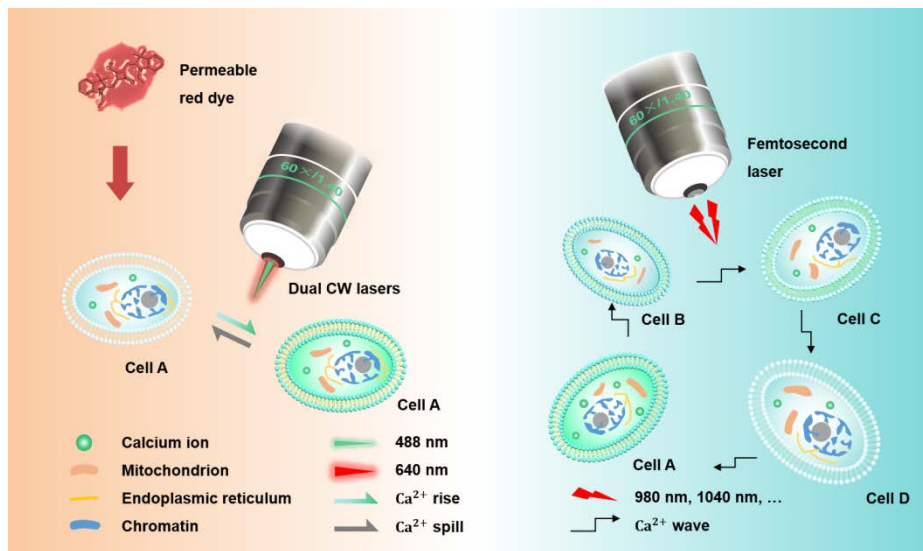


Figure2: Comparison between stain-free MAMG microscopy and H&E histopathology in a cancer colony followed by cancer-associated angiogenesis (star) as backup.

References

- [1] Fangrui Lin, Pintu DAS, Yihua Zhao, Binglin Shen, Rui Hu, Feifan Zhou, Liwei Liu, Junle Qu, Monitoring the endocytosis of bovine serum albumin based on the fluorescence lifetime of smallsquaraine dye in living cells, Biomed. Opt. Express. 149-159, 2020.
- [2] Binglin Shen, Shiqi Wang, Ganapathi Bharathi, Yangping Li, Fangrui Lin, Rui Hu, Liwei Liu, Junle Qu, Rapid and Targeted Photoactivation of Ca^{2+} Channels Mediated by Squaraine To Regulate Intracellular and Intercellular Signaling Processes, Anal. Chem., 8497-8505, 2020.
- [3] Binglin Shen, Liwei Liu, Junshuai Yan, Shiqi Wang, Feifan Zhou, Yihua Zhao, Rui Hu, Junle Qu, Large-field stain-free histopathology of metastatic colonization by multimodal optical methods, Theranostics 2020, Vol. 10, Issue 4.



LASER-INDUCED LOCAL VASCULAR RESPONSES

DMITRY POSTNOV AND ELENA LITVINENKO

Dept. Optics and Biophotonics, Saratov State University, Russia

postnov@info.sgu.ru

Abstract

It is well known that low-intensity laser irradiation of living tissues evokes a number of responses [1]. However, the specific mechanisms of action of a focused laser beam on individual cells and their small ensembles have been much less studied. One of pioneering work is [2] where actions of an argon laser of 514nm on mouse vessels were studied. In [3] the responses of aorta of white rabbits an exmeric laser irradiation was found dependant on specific treatment (norepinephrine versus nitroglycerin). In [4] both vasodilation of the vessels under study and an increase in the blood flow velocity were observed in response to the irradiation by He–Ne laser with a wavelength of 630nm, depending on the location of the vessel. A review [5] listed a group of studies showing that laser exposure to blood inside a vessel can stimulate a short-term release of nitric oxide (NO) by red blood cells, which in turn has a vasodilating effect.

We present the results of the experimental studies on the effect of a highly localized laser irradiation on the activity of cells in the vascular wall of blood and lymph vessels. The initial goal of our work was to propose a new method of localized and reversible (non-destructive) action on the microcirculatory network in order to study what changes will be observed in neighboring vessels. The experimental setup (Fig 1, a) allowed the dose-controlled irradiation of small portion of a vessel consisted of a few cells of the vascular wall and the lumen of the vessel itself. The intensity of irradiation was empirically adjusted so as to achieve a pronounced vasomotor reaction, but not damage the vessel itself by heating. We studied the reactions of blood vessels in the chorioallantoic membrane of chick embryos grown both in ovo and ex ovo. The study of the reactions of the lymphatic vessels was carried out on the mesentery of the rat.

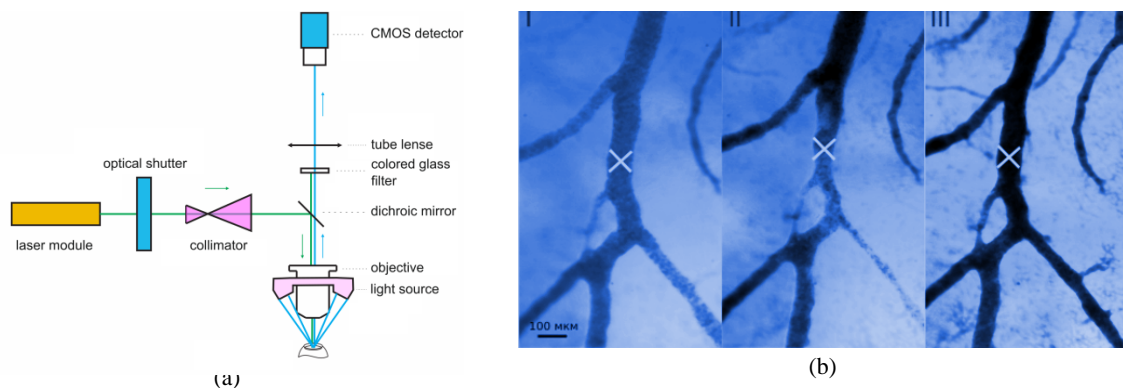


Figure 1: The experimental setup (a) and the representative response (reversible constriction) of small arterial vessel to the focal irradiation by the 405 nm laser

The main result of our studies is that the correctly selected irradiation dose always triggers a vasomotor response. The details depends on the wavelength of the laser used, but this dependence can also be explained by the different degree of absorption of radiation by tissues, that is, the type of reaction may be regarded dose-

dependent. The fact that laser irradiation stimulates the contractile activity of the lymph vessels suggests that the reactions of the vascular wall cells play an important role in the observed effects. The practical application of the developed method to the study of the network blood flow allowed us to visualize complex interrelated reactions in several (up to 5) neighboring vessels of the network. The research was supported by RFBR grant #19-515-55016.

References

- [1] Avci, P., Gupta, A., Sadasivam, M., Vecchio, D., Pam, Z., Pam, N., and Hamblin, M., "Low-level laser (light) therapy (llt) in skin: stimulating, healing, restoring," *Semin Cutan Med Surg.* 32(1), 41–52 (2013).
- [2] Barkovskii, V. S., Kozlov, V. I., Saprykin, P. I., and Nikol'skaya, G. M., "Response of microvessels of the subcutaneous areolar tissue to argon laser irradiation," *Bulletin of Experimental Biology and Medicine* 85(6), 731–734 (1978).
- [3] Mosseri, M., Pickering, J., Chokshi, S., Gal, D., and Isner, J., "Excimer laser-induced vasoreactivity," *European Heart Journal* 14(10), 1394 (1993).
- [4] Chertok, V., Kotsyuba, A., and Bespalova, E., "Features of the reaction of the vessels of the microcirculatory bed of some organs to the action of a helium-neon laser (in russian)," *Pacific Medical Journal* 3(29), 48–52 (2007).
- [5] Hamblin, M. and Demidova, T., "Mechanisms of low level light therapy," *Proc. SPIE* 6140, 614001 (2006).

BREAK THE UNBROKEN LIMITS TOWARD SUPER-RESOLUTION MICROSCOPY

QIUQIANG ZHAN

Centre for Optical and Electromagnetic Research, South China Academy of Advanced Optoelectronics, South China Normal University, Guangzhou 510006, P. R. China

*E-mail: zhanqiuqiang@m.scnu.edu.cn

Abstract

The resolution of an optical imaging system, a microscope, is always theoretically limited due to the physics of diffraction [1]. Memorial to Ernst Karl Abbe, who approximated the diffraction limit of a microscope as, $d=\lambda/2n\sin\theta$, where d is the resolvable feature size, λ is the wavelength of light, n is the index of refraction of the medium being imaged in, and the term “ $n\sin\theta$ ” representing the numerical aperture[1]. Theoretically, the full width at half maximum (FWHM) of the point spread function (PSF) for the N -photon microscopic imaging could be described by the formula $d=\lambda/(2n\sin\theta N^{1/2})$, ($N\geq 2$), which, in principle, helps to improve the resolution. It is challenging to resolve the contradiction of high-order nonlinearity and required short excitation wavelength. Lanthanide-doped photon upconversion nanoparticles (UCNPs) are capable of converting low-intensity near-infrared light to UV and visible emission through the synergistic effects of light excitation and mutual interactions between doped ions[2]. To overcome these problems, we propose visible-to-visible four-photon ultrahigh resolution microscopic imaging by using a common cost-effective 730-nm laser diode to excite the prepared Nd^{3+} -sensitized upconversion nanoparticles with the obtained lateral resolution as high as 161-nm[3]. The stimulated emission depletion (STED) microscopy that has broken the diffraction limit of optical microscopic imaging has become crucial methods for molecularly-resolved imaging in the life sciences and beyond [4,5], with the resolution governed by $d=\lambda/(2n\sin\theta(1+I_{\text{sat}})^{1/2})$. In 2015, as shown in (Fig.1), we firstly demonstrated the potential of UCNPs for multi-photon super-resolution microscopy [1]. In 2017, our group has developed a novel low-power CW laser enabled STED mechanism using optimized lanthanide upconversion nanoparticles [7]. We have experimentally achieved highly efficient, absolutely non-bleaching cytoskeleton STED imaging at subcellular scale. These findings have great potential in super-resolution microscopy [8]. Can we break the theoretical limit of I_{sat} , like breaking the diffraction limit? Yes, very recently we have successfully broken the limit of I_{sat} by two orders using new depletion mechanism for further pull down the laser power for super-resolution.

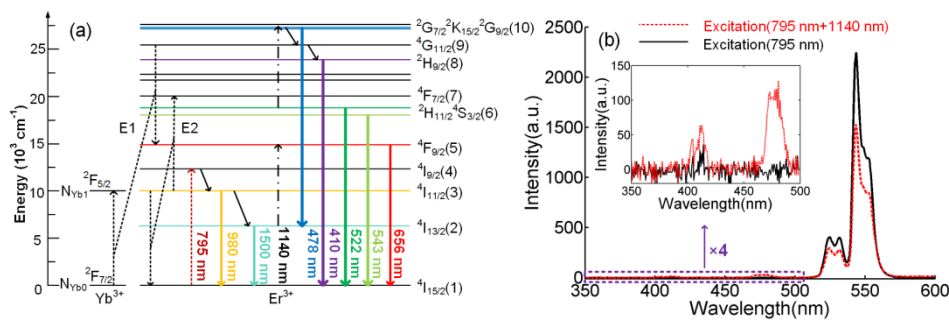


Figure 1: (a) Proposed mechanism of luminescence generation of 795-nm laser excited $\text{NaYF}_4:\text{Yb}^{3+}/\text{Er}^{3+}$ UCNPs with/without 1140-nm irradiation. (b) Luminescence intensity of $\text{NaYF}_4:\text{Yb}^{3+}/\text{Er}^{3+}$ UCNPs under 795-nm CW excitation with/without 1140-nm irradiation. Inset figure: the amplified luminescence spectra from 350 nm to 500 nm [6].

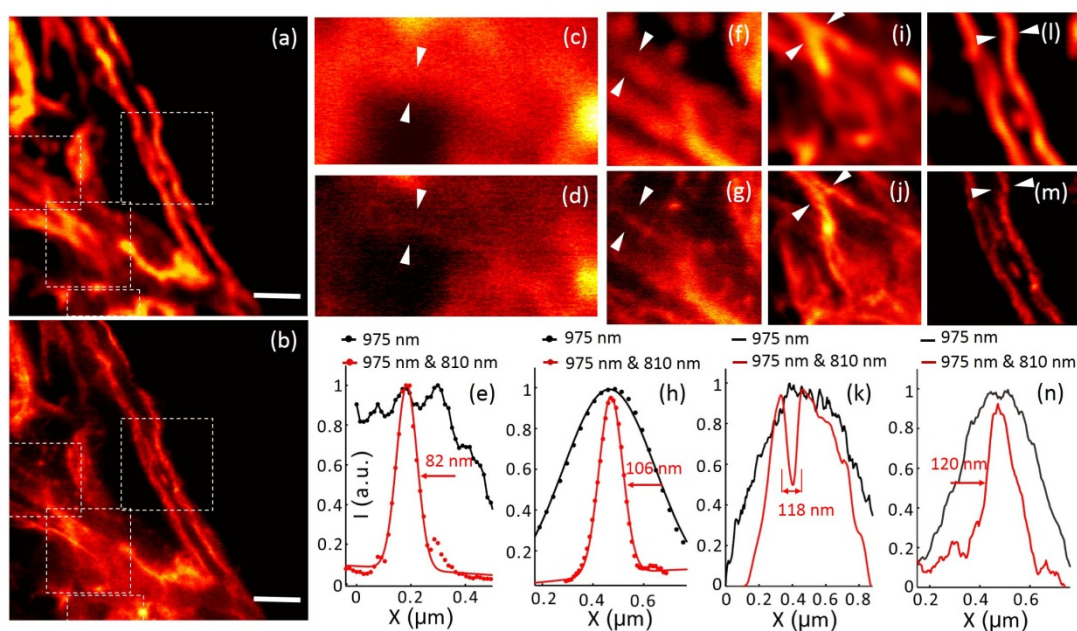


Figure 2: Immunofluorescence labeling of cellular cytoskeleton protein desmin with antibody conjugated UCNPs and super-resolution imaging. (a) The multiphoton imaging under 975 nm excitation of some cytoskeleton structures and desmin proteins in HeLa cancer cells incubated with anti-desmin primary antibody and immunostained with UCNPs (~11.8 nm in diameter) bioconjugated with goat Anti-rabbit IgG secondary antibody. (b) The same region with (a) imaged in the super-resolution mode (975 nm excitation and the 810 nm STED laser beam). Scale bars: 2 μm . (c-n) Magnified areas selected from a, b (marked by white dotted squares) and line profile analyses; Images in c, f, i and l are taken from the white dotted squares in a; Images in d, g, j and m are taken from the white dotted squares in b. (e, h, k, n) Line profiles analyses of several areas indicated by arrow heads in c and d, f and g, i and j, and l and m, respectively[7].

References

- [1] Abbe, E., Beiträge zur Theorie des Mikroskops und der mikroskopischen Wahrnehmung. *Archiv für Mikroskopische Anatomie* 1873,9, 413-468.
- [2] Xu, C. T.; Zhan, Q.; Liu, H.; Somesfalean, G.; Qian, J.; He, S.; Andersson-Engels, S., Upconverting nanoparticles for pre-clinical diffuse optical imaging, microscopy and sensing: Current trends and future challenges. *Laser & Photonics Reviews* 2013,7, 663-697.
- [3] Wang, B.; Zhan, Q.; Zhao, Y.; Wu, R.; Liu, J.; He, S., Visible-to-visible four-photon ultrahigh resolution microscopic imaging with 730-nm diode laser excited nanocrystals. *Opt Express* 2016,24, A302-A311.
- [4] Hell, S. W.; Wichmann, J., Breaking the diffraction resolution limit by stimulated emission: stimulated-emission-depletion fluorescence microscopy. *Opt. Lett.* 1994,19, 780-782.
- [5] Willig, K. I.; Rizzoli, S. O.; Westphal, V.; Jahn, R.; Hell, S. W., STED microscopy reveals that synaptotagmin remains clustered after synaptic vesicle exocytosis. *Nature* 2006,440, 935-939.
- [6] Wu, R.; Zhan, Q.; Liu, H.; Wen, X.; Wang, B.; He, S., Optical depletion mechanism of upconverting luminescence and its potential for multi-photon STED-like microscopy. *Opt Express* 2015,23, 32401-32412.
- [7] Zhan, Q.; Liu, H.; Wang, B.; Wu, Q.; Pu, R.; Zhou, C.; Huang, B.; Peng, X.; Ågren, H.; He, S., Achieving high-efficiency emission depletion nanoscopy by employing cross relaxation in upconversion nanoparticles. *Nature Communications* 2017,8, 1058.
- [8] Peng, X.; Huang, B.; Pu, R.; Liu, H.; Zhang, T.; Widengren, J.; Zhan, Q.; Ågren, H., Fast upconversion super-resolution microscopy with 10 μs per pixel dwell times. *Nanoscale* 2019,11, 1563-1569.

MEDICAL APPLICATIONS OF IR AND THZ LASER MOLECULAR IMAGING AND MACHINE LEARNING

YU.V.KISTENEV^{1,3}, A.V.BORISOV^{1,3}, A.I.KNYAZKOVA^{1,2}, D.A.VRAZHNOV^{1,2}, V.E SKIBA¹,
V.V. PRISCHEPA¹, A.CUISSET⁴

¹National Research Tomsk State University, Tomsk, Russia

²Institute of Strength Physics and Materials Science SB RAS, Tomsk, Russia

³Siberian State Medical University, Tomsk, Russia

⁴Université du Littoral Côte d'Opale, Dunkerque, France

Abstract

The problem of relevant information extracting from 2D and 3D laser molecular imaging experimental data, which can be used for medical diagnosis, is of great importance. Due to the high dimension of molecular imaging data, methods of mathematical statistics become inefficient. To overcome this problem, we use a machine learning approach. A typical machine learning pipeline is shown in Fig.1.

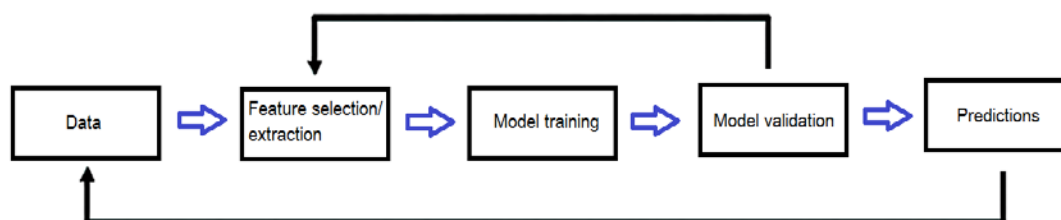


Figure 1: A typical machine learning pipeline.

The peculiarities of molecular imaging in IR and THz spectral ranges, methods of extracting of informative features from experimental data, and creating of prognostic models for medical diagnosis using machine learning methods will be discussed for three fields of applications: diagnostics using breath air or biofluids spectral analysis, and noninvasive tissue spectroscopy and visualization.

This work was performed under the Government statement of work for ISPMS Project No. III.23.2.10, and with partial financial support from the Russian Foundation for Basic Research, Grant No. №17-00-00275 (17-00-00186).

REFRACTIVE PROPERTIES OF BLOOD SERUM OF RATS WITH EXPERIMENTAL LIVER CANCER

EKATERINA N. LAZAREVA^{1,2}, POLINA A. DYACHENKO^{1,2}, MAXIM M. NAZAROV³, ALLA B. BUCHARSKAYA⁴, VALERY V. TUCHIN^{1,2,5,6}, ALEXANDER P. SHKURINOV^{7,8}

¹Saratov State University, Saratov, Russia

²National Research Tomsk State University, Tomsk, Russia

³National Research Center "Kurchatov Institute", Moscow, Russia

⁴Saratov State Medical University, Saratov, Russia

⁵ITMO University, St. Petersburg, Russia

⁶Institute of Precision Mechanics and Control, Russian Academy of Sciences, Saratov, Russia

⁷Department of Physics and International Laser Center, M.V. Lomonosov Moscow State University, Russia

⁸Crystallography and Photonics Federal Research Center, Russian Academy of Sciences, Moscow, Russia

lazarevaen@list.ru

Abstract

Currently, optical methods are widely used in medicine. They are easy to use and minimally invasive. However, their application and improvement require the most accurate information on the optical properties of tissues and their components. The refractive index (RI) is one of the major parameters, which characterizes how light interacts with biological tissue. In addition, the RI could be different for healthy and pathological tissues, which makes it possible to use RI as a biological marker.[1, 2].

We studied the refractometric properties of rat serum in the development of liver cancer in the visible, NIR and THz ranges. Studies were performed on laboratory animals for three groups: control, 14 days and 28 days after transplantation of the tumor into the area of the scapulae. The refractive index in the visible and NIR regions was measured using multi-wavelength Abbe refractometer DR-M2/1550 (Atago, Japan). Measurements for the THz region were performed on the terahertz (THz) time-domain spectrometer. The dispersion dependence for the visible, NIR, and THz regions is presented in Fig. 1.

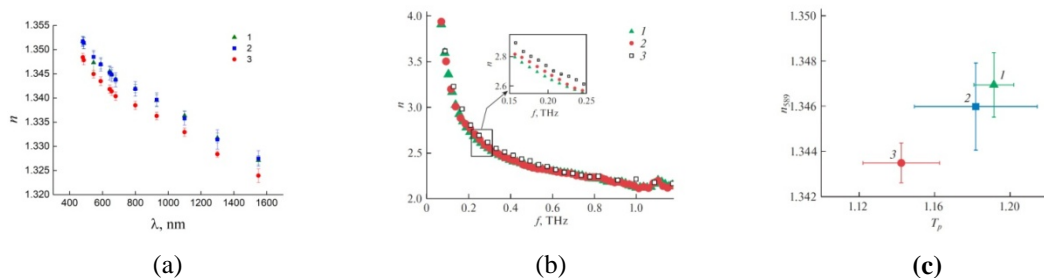


Figure 1: Dispersion of serum samples: A - for visible and NIR spectral ranges, B – for THz spectral range; C - The correlation between the refractive index at a wavelength of 589 nm and the normalized (to water) amplitude of the THz transmittance of T_p of the blood serum. (1 is control group (triangles), 2 is group after 14 days (squares), 3 is group after 28 days (circles)).

The decrease in the RI in the visible region during the development of oncologic disease in animals is due to a decrease in protein concentration, since the concentration of protein in the blood is linearly related to the refractive index. The high correlation between the data in the THz and visible regions, for example, makes it possible to reconstruct the dispersion dependence in the THz region from known values of the refractive index in the visible region and from the absorption coefficient in the THz region using the Kramers–Kronig relations.

Acknowledgements: The studies were funded by RFBR project № 17-00-00275 (17-00-00270, 17-00-00272).

References

- [1] V.V. Tuchin, “Tissue Optics: Light Scattering Methods and Instruments for Medical Diagnosis”, 3rd Ed., Bellingham, SPIE Press, 2015.
- [2] M.M. Nazarov, O.P. Cherkasova and A.P. Shkurinov, “Study of the dielectric function of aqueous solutions of glucose and albumin by THz time-domain spectroscopy”, *Quantum Electronics*, vol. 46(6), pp. 488-495, 2016.

NANOMEDICINE IN CANCER PHOTOIMMUNOTHERAPY**XIAO-LONG LIU^{1,2}, MING WU^{1,2}, DA ZHANG^{1,2} AND ZHIXIONG CAI^{1,2}**¹ *Mengchao Hepatobiliary Hospital of Fujian Medical University, P. R. China*² *Department of Translational Medicine, Xiamen Institute of Rare Earth Materials, Chinese Academy of Sciences,**P. R. China*xiaoloong.liu@gmail.com**Abstract**

Cancer immunotherapy has become one of the most promising therapeutic approach for cancer treatment through harnessing and boosting the patient's own immune system to eliminate both the primary and metastatic tumor cells [1]. Although it has achieved great success in clinic recently, the objective response rate (ORR) of immunotherapy including checkpoint inhibitors such as PD-1 or PD-L1 antibodies and chimeric antigen receptor T-cell (CAR-T) therapy in most solid tumors, is still extremely limited due to that most solid tumors are featured as cold tumor, characterized as tumor heterogeneity [2], hypoxic microenvironment [3], restricted tumor-infiltrating lymphocytes [2], weak immunogenicity^[3], and high expression of immune-inhibiting molecules [4]. Therefore, there is an urgent need to develop new strategies to reverse the "cold" state of solid tumors, and combined with other treatment paradigm to improve the therapeutic outcomes of immunotherapy.

Our group is focusing on developing novel nanomedicine to combine immunotherapy with other therapeutic modalities, such as photodynamic therapy (PDT) or photothermal therapy (PTT) to improve the response rate of different immunotherapy paradigm. PDT has been extensively studied in solid tumor treatment, while it usually aggravates tumor hypoxia, which promotes the survival and metastasis of residue cancer cells; although it has been reported that PDT also could induce immunogenic death of cancer cells to activate host anti-tumor responses, but such responses were generally weak and not enough to eliminate the residue cancer cells; therefore, the tumors always suffer fast recurrence after PDT treatment. To resolve these problems, we designed metal-organic framework (MOF) based nanoparticles to combine PDT, anti-hypoxic signaling, and CpG adjuvant as in-situ immunostimulant to boost the host anti-tumor responses after PDT. The MOF based nanoparticles were self-assembled through the coordination of photosensitizer (H2TCPP) and Zirconium ions (named as PCN); the HIF-1 α inhibitor acriflavine (ACF) was loaded into the pores of PCN, and the immunologic adjuvant CpG was successively coated on the surface; afterwards, the hyaluronic acid (HA) was coated on the out surface. The aggravated hypoxic survival signaling after PDT could be blocked by ACF to inhibit the HIF-1 α induced survival and metastasis. With the help of CpG adjuvant, the tumor associated antigens generated from PDT based cancer cell destruction could initiate strong antitumor immune responses to eliminate residue cancer cells. By integrating these strategies, our designed novel MOF system could significantly improve the cancer therapeutic efficiency both *in vitro* and *in vivo* (Figure 1 Left)[3].

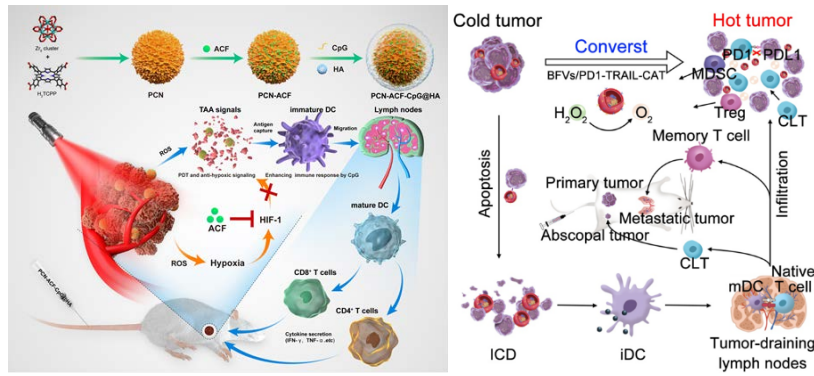


Figure 1: (Left) Schematic illustration of the preparation procedure and the working principle of PCN-ACF-CpG@HA to integrate PDT, anti-hypoxic signaling and CpG adjuvant as in-situ immunostimulant. (Right) Schematic illustration of the mechanism of BFVs that generate robust antitumor immune responses. BFVs synergistically improve immunotherapy by converting immune cold into hot.

To systematically converting the immune cold tumor to hot tumor, we developed biosynthetic functional vesicles (BFVs) to integrate strategies including overcome hypoxia, induce immunogenic cell death and immune checkpoint inhibition to boost systematic antitumor immunity. The BFVs presents PD1 and tumor necrosis factor-related apoptosis-inducing ligand (TRAIL) on the surface, while loads catalase into its inner core. The TRAIL can specifically induce immunogenic death of cancer cells to initiate immune response, which is further synergistically strengthened by blocking PD1/PDL1 checkpoint signal through ectogenic PD1 proteins on BFVs. The catalase can catalyze high level of H₂O₂ in tumor microenvironment to produce O₂ to overcome tumor hypoxia, in turn to increase infiltration of effector T cells while deplete immunosuppressive cells in tumor. The comprehensive immuno-modulating ability of BFVs elicits robust and systematic antitumor immunity, as demonstrated by significant regression of tumor growth, prevention of abscopal tumors and excellent inhibition of lung metastasis (Figure 1 Right) [2].

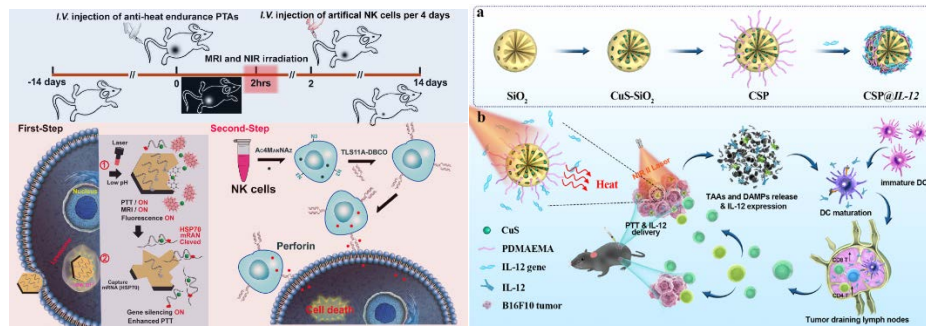


Figure 2:(Left) Schematic illustration of Artificial engineered NK cells combined with anti heat endurance strategy for improving the therapeutic efficiency of PTT. (Right) (a) Schematic illustration of CSP@IL-12 nanocomplex synthesis. (b) The mechanism of anti-tumor effects of CSP@IL-12 nanocomplex for synergistic PTT and IL-12 cytokine therapy by tumor local administration.

PTT has also been pre-clinically applied in solid tumor treatment, while the incomplete tumor removal of PTT and heat endurance of tumor cells would induce significant tumor relapse after treatment. To overcome these shortages, we designed a programmable therapeutic strategy that integrated PTT agents (PTAs) for MRI guided phototherapy, DNazymes for anti-heat endurance, and artificial engineered natural killer (A-NK) cells for adoptive immunotherapy. The novel PTAs exhibited excellent light-to-

heat conversion ability, tumor micro-environment enhanced T1-MRI guiding ability, and anti-heat endurance ability through activating DNazymes by released Mn²⁺ after PTT to cleave HSP70 mRNA. Furthermore, the artificial engineered NK cells could specifically eliminate any possible residual tumor cells after PTT, to systematically enhance the therapeutic efficacy of PTT and avoid tumor relapse. Overall, we highlighted the potential of A-NK cells combined with anti-heat endurance as powerful adjuvant for immuno-enhancing photothermal therapy efficiency of solid tumors (Figure 2 Left)[4]. Furthermore, a novel photothermal and gene co-delivery nanoparticle, with CuS inside the SiO₂ pore channels and PDMAEMA polycation on the outside of SiO₂ surface, is also explored for tumor localized NIR II PTT and in situ immunotherapy through local generation of IL-12 cytokine. The resultant CSP integrated with the plasmid encoding IL-12 gene (CSP@IL-12) exhibited excellent gene transfection efficiency, outstanding NIR-II PTT effect and excellent therapeutic outcomes both *in vitro* and *in vivo*. Such an in situ synergistic therapy modality could significantly induce systemic immune responses including promoting DC maturation, CD8⁺ T cell proliferation and infiltration to efficiently eliminate possible metastatic lesions through abscopal effects. Hence, this creative synergistic strategy of NIR-II PTT and IL-12 cytokine therapy might provide a more efficient, controllable and safer alternative strategy for future photo-immunotherapy (Figure 2 Right).

References

- [1] E. Vivier, S. Ugolini, D. Blaise, C. Chabannon, L. Brossay. Targeting natural killer cells and natural killer T cells in cancer. *Nature Reviews Immunology*, 12(4), 239-252, 2012.
- [2] M Wu, D Zheng, D Zhang, P Yu, L Peng, F Chen, Z Lin, Z Cai, J Li, Z Wei, X Lin, J Liu, X Liu. Converting Immune Cold into Hot by Biosynthetic Functional Vesicles to Boost Systematic Antitumor Immunity. *iScience*, 23(7):101341, 2020.
- [3] Z Cai, F Xin, Z Wei, M Wu, X Lin, X Du, G Chen, D Zhang, Z Zhang, X Liu, C Yao. Photodynamic Therapy Combined with Antihypoxic Signaling and CpG Adjuvant as an In Situ Tumor Vaccine Based on Metal-Organic Framework Nanoparticles to Boost Cancer Immunotherapy. *Adv Healthcare Materials*, 9(1): e1900996, 2020.
- [4] Zhang D, Zheng Y, Lin Z, Lan S, Zhang X, Zheng A, Li J, Liu G, Yang H, Liu X, Liu J. Artificial Engineered Natural Killer Cells Combined with Antiheat Endurance as a Powerful Strategy for Enhancing Photothermal-Immunotherapy Efficiency of Solid Tumors. *Small*, 15(42): e1902636, 2020.

STUDY OF SKIN DEHYDRATION IN THE COURSE OF GRAFTED TUMOR DEVELOPMENT USING SPECTRAL REFRACTOMETRY, NIR AND THZ SPECTROSCOPY

POLINA DYACHENKO (TIMOSHINA)^{1,2}, EKATERINA LAZAREVA^{1,2}, MAXIM NAZAROV³, ALLA BUCHARSKAYA⁴, VALERY TUCHIN^{1,2,5} AND ALEXANDER SHKURINOV⁶

¹Saratov State University, Russia

²National Research Tomsk State University, Russia

³NRC «Kurchatov Institute», Russia

⁴Saratov State Medical University, Russia

⁵Institute of Precision Mechanics and Control, Russian Academy of Sciences, Saratov, Russia

⁶Lomonosov Moscow State University, Russia

timoshina2906@mail.ru

Abstract

Currently, different optical methods are widely used for diagnostics and therapy of some diseases. An increase of image contrast induced by tissue dehydration and optical clearing in the area of pathology is extremely important for the monitoring of precancerous conditions, early stages of cancer and other diseases [1]. The combination of studies in the optical and terahertz ranges opens up new possibilities for more reliable diagnosis of a number of diseases.

In this work, experimental studies of the spectral characteristics of the skin of laboratory animals with an inoculated tumor when probed by an optical clearing agent (100% glycerol solution). The reflection spectra were recorded in the spectral range 900–2000 nm using a USB4000-Vis-NIR spectrometer (Ocean Optics, USA) and a QR400-7-Vis / NIR fiber probe (Ocean Optics, USA). The tumor was inoculated by subcutaneous injection of 0.5 ml of a 25% tumor cell suspension in the Hanks solution of PC1 alveolar liver cancer strain into the scapula area. Laboratory rats were divided into two groups: pathological group No. 1 with a tumor inoculated 14 days after vaccination of a tumor and pathological group No. 2 with a vaccinated tumor after 28 days after inoculation of a tumor. NIR Spectroscopy measurements were taken from the skin area directly above the tumor formation and nearby (control area) without neoplasm. For the optical clearing study, a 99.3% glycerol solution was poured into a special cuvette in an amount of 1 ml, which openly touched the skin to ensure complete contact of the OCA with the skin surface for 30 min. After removal of the solution, reflection spectra were recorded from the studied area of the skin. Next, studies of the solution collected after 30 min of exposure to the skin were carried out using refractometry in the visible/NIR and THz spectroscopy. The refractive index of modified glycerol solutions was measured using an Abbe DR-M2 / 1550 multiwave refractometer (Atago, Japan). To select the wavelengths, interference filters were used for 480, 486, 546, 589, 644, 656, 680, 800, 930, 1100, 1300, and 1550 nm.

In both groups, an increase in the concentration of water in the skin of animals under the influence of OCA was recorded. This may happen due to strong glycerol affinity to water molecules which migrated from the in-depth skin layers and subcutaneous tissues to the site, where glycerol is. It was also noted that there are differences in the effect of the optical clearing agent on the concentration of water in the skin of control sites and over the tumor (Fig.1). This indicates a change in the optical properties of the skin under the development of pathology. The development of a malignant neoplasm caused a delayed diffusion of the agent into the skin, which is confirmed by the small effect of the agent on the concentration of water over the tumor neoplasm, in contrast to the skin of a healthy rat. The results obtained by the three methods correlate with each other.

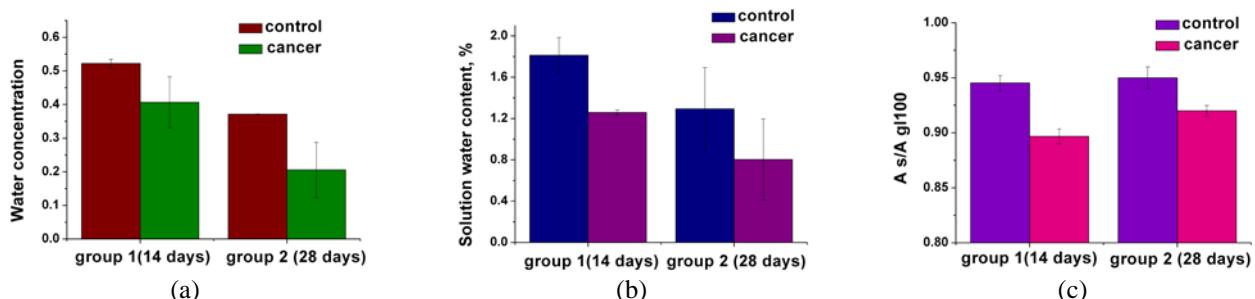


Figure 1: (a) Data on changes in the concentration of water in the skin for both groups by NIR Spectroscopy; (b) data for the ratio of the transmittance amplitude of the sample relative to the transmittance amplitude of a pure glycerol solution in the THz region; (c) water content in glycerol solution according to the results of measurements of the refractive index in the visible/NIR regions.

The presented study were made possible with was supported by grants RFBR 17-00-00270 (PD, EL, MN, AS), 17-00-00272 (VT).

References

- [1] V.V. Tuchin, Tissue Optics: Light Scattering Methods and Instruments for Medical Diagnostics, 3rd ed., SPIE Press, Bellingham, Washington , p. 988, 2015

SILICON NANOMATERIALS FOR BIOSENSING AND BIOIMAGING

YAO HE

¹Laboratory of Nanoscale Biochemical Analysis, Institute of Functional Nano & Soft Materials (FUNSOM) and Jiangsu Key Laboratory for Carbon-based Functional Materials & Devices, Soochow University, Suzhou 215123, China

yaohe@suda.edu.cn

Abstract

During the past decades, silicon nanotechnology for biological and biomedical applications has been extensively studied due to the favorable biocompatibility of silicon. Notably, silicon nanohybrids featuring unique electronic/optical/mechanical properties have been widely employed for constructing biosensing platforms with excellent sensitivity, good specificity, adaptable reproducibility, and multiplexing capabilities [1-4]. In addition, it is worth mentioning that the silicon nanohybrids can be explored for setting up surface-enhanced Raman scattering (SERS) big data, allowing artificial intelligence (AI)-based DNA discrimination in label-free manners [5]. On the other hand, proof-of-concept studies have opened up promising avenues for developing fluorescent silicon nanoprobe-based bioimaging techniques. Of particular significance, silicon-based nanoprobe feature strong fluorescence, robust photostability, and negligible toxicity. Those attractive merits have triggered extensive exploration of functionalized silicon nanomaterials as potentially ideal biological fluorescent probes, showing high promise for *in vitro* and *in vivo* bioimaging analysis [6-10].

References

- [1] R.Z. Chen, H.Y. Shi, X.Y. Meng, Y.Y. Su, H.Y. Wang, Y. He, Dual-amplification strategy-based SERS chip for sensitive and reproducible detection of DNA methyltransferase activity in human serum, *Anal. Chem.* 3597-3603, 2019, 91.
- [2] X.Y. Meng, H.Y. Wang, N. Chen, P. Ding, H.Y. Shi, X. Zhai, Y.Y. Su, Y. He, A Graphene–Silver Nanoparticle–Silicon Sandwich SERS Chip for Quantitative Detection of Molecules and Capture, Discrimination, and Inactivation of Bacteria, *Anal. Chem.* 5646-5653, 2018, 90.
- [3] B.B. Chu, B. Song, X.Y. Ji, Y.Y. Su, H.Y. Wang, Y. He, Fluorescent Silicon Nanorods-Based Ratiometric Sensors for Long-Term and Real-Time Measurements of Intracellular pH in Live Cells, *Anal. Chem.* 12152-12159, 2017, 89.
- [4] H.Y. Wang, Y.F. Zhou, X.X. Jiang, B. Sun, Y. Zhu, H. Wang, Y.Y. Su, Y. He, Simultaneous Capture, Detection, and Inactivation of Bacteria as Enabled by a Surface-Enhanced Raman Scattering Multifunctional Chip, *Angew. Chem., Int. Ed.* 5132-5136, 2015, 54.
- [5] H.Y. Shi, H.Y. Wang, X.Y. Meng, R.Z. Chen, Y.S. Zhang, Y.Y. Su, Y. He, Setting Up a Surface-Enhanced Raman Scattering Database for Artificial-Intelligence-Based Label-Free Discrimination of Tumor Suppressor Genes, *Anal. Chem.* 14216-14221, 2018, 90.
- [6] B. Song, Y. Zhong, S. Wu, B. Chu, Y. Su, Y. He, One-Dimensional Fluorescent Silicon Nanorods Featuring Ultrahigh Photostability, Favorable Biocompatibility, and Excitation Wavelength-Dependent Emission Spectra, *J. Am. Chem. Soc.* 4824-4831, 2016, 138.
- [7] S.C. Wu, Y. Zhong, Y. Zhou, B. Song, B. Chu, X. Ji, Y. Wu, Y.Y. Su, Y. He, Biomimetic Preparation and Dual-Color Bioimaging of Fluorescent Silicon Nanoparticles, *J. Am. Chem. Soc.* 14726-14732, 2015, 137.
- [8] F. Peng, Y.Y. Su, Y. Zhong, S.T. Lee, Y. He, Silicon Nanomaterials Platform for Bioimaging, Biosensing, and Cancer Therapy, *Acc. Chem. Res.* 612-623, 2014, 47.
- [9] M.M. Tang, X.Y. Ji, H. Xu, L. Zhang, A.R. Jiang, B. Song, Y.Y. Su, Y. He, Photostable and Biocompatible Fluorescent Silicon Nanoparticles-Based Theranostic Probes for Simultaneous Imaging and Treatment of Ocular Neovascularization, *Anal. Chem.* 8188-8195, 2018, 90.
- [10] J.L. Tang, B.B. Chu, J.H. Wang, B. Song, Y.Y. Su, H.Y. Wang, Y. He, Multifunctional Nanoagents for Ultrasensitive Imaging and Photoactive Killing of Gram-Negative and Gram-Positive Bacteria, *Nat. Commun.* 4057, 2019, 10.

DISPERSION-MEDIATED CONJUGATE SUPPRESSION FOR HIGH SPEED OPTICAL COMPUTING OCT IMAGING

WENXIN ZHANG, CHENGMING WANG, ZHENYU CHEN, BIN HE, ZHANGWEI HU AND PING XUE*

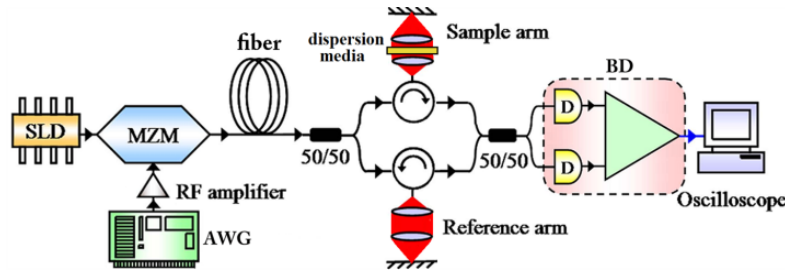
Department of Physics, Tsinghua University, Beijing, 100084, China

* xuep@tsinghua.edu.cn

Abstract

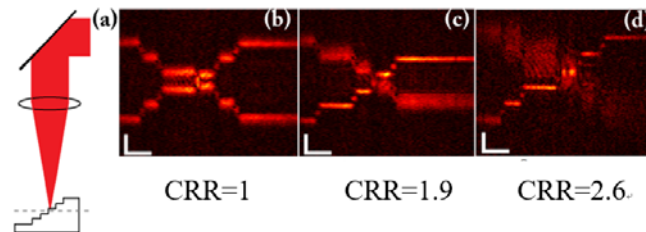
We will illustrate that optical computing optical coherence tomography with proper dispersion imbalance may achieve ~ 2 times higher resolution and restrain the conjugate signal without any data processing at imaging speed of 5M-A-scans per second.

For all imaging techniques such as optical coherence tomography (OCT)[1], fast imaging speed is always of high demand. Optical computing OCT (OC²T) has achieved ultrahigh speed for real time 3D imaging without post data processing, but its spatial resolution is lowered down due to an imperfect Fourier transformation in the optical computing process. In this talk, we will illustrate the theory of OC²T and prove that the dispersion imbalance between reference arm and sample arm may be introduced to improve the resolution. Furthermore, this novel OC²T technique can also enable a conjugate restrained OCT imaging without any data processing, achieving ~ 2 times higher resolution than typical OC²T. At an imaging speed of as high as 5M-A-scans per second, the dispersion imbalance OC²T has strong ability of restraining the conjugate signal with a conjugate signal rejection ratio of 2.6.



Figures 1: Optical design of the OC²T. SLD: super luminescent diode, MZM: Mach-Zehnder modulator, AWG: arbitrary waveform generator, RF: radio frequency, BD: balanced detector.

The optical design of the OC²T [2] is shown in Fig.1. An MZM (JDS Uniphase, OC-192, bandwidth of 10GHz) is used to modulate the light. The modulation function is generated by an arbitrary waveform generator (AWG, Keysight, M8195A, bandwidth of 40GHz). An envelope detector is used to acquire the envelope of high frequency signal to form OCT image.



Figures 2 : Comparison of OC²T with different CRR for real time conjugate suppression.(a) Sample arm; (b) typical OC²T image with balanced dispersion; (c) OC²T image with proper dispersion imbalance and CRR=1.9; (d) OC²T image with proper dispersion imbalance and CRR=2.6; the scare bar refers to 100 μ m.

To describe how much the conjugate signal is restrained, we may define conjugate signal rejection ratio $CRR = \frac{\text{amplitude of signal}}{\text{amplitude of conjugate}}$, which is [3]: $CRR = (1 + 16a^3L^4\beta_L^4 / c^4\gamma^4)^{1/4}$, where, $\gamma = (2\ln 2)^{1/2} \lambda_0^2 / (c\pi\Delta\lambda)$ is the bandwidth of the light λ_0 in angular frequency and $\Delta\lambda$ the FWHM bandwidth in wavelength. a is a constant and a^*t the modulation frequency of the MZM at the time t . L, β_L , care the fiber

length, group-velocity dispersion and speed of light, respectively. Real time conjugate suppression for high speed optical computing OCT imaging is shown in Fig. 2. Larger suppression can be achieved with larger L . However, L has an upper limit for a fixed optical computing speed, which is, by now, 150 km to achieve $\text{CRR}=35$ with optical computing speed of 5M-A-scans/s and duty cycle of 80%.

Our technique demonstrates, for the first time, the real time conjugate suppression without post-processing at imaging speed of as high as 5M-A-scans per second, the fastest speed up to now to our knowledge.

References

- [1] D. Huang, et al, "Optical coherence tomography" *Science* 254, 1178, (1991).
- [2] X. Zhang, et al, "Optical computing for optical coherence tomography" *Sci. Rep.* 6, 37286, (2016).
- [3] W. Zhang, et al, "Optical computing optical coherence tomography with conjugate suppression by dispersion" *Opt. Lett.*, 44(8): 2077, (2019).

THE ROLE OF INDIVIDUAL CYSTEINE SUBSTITUTIONS IN THE FAST PHOTOSWITCHING AND PHOTOCONVERSION OF THE BIPHOTOCHROMIC FLUORESCENT PROTEIN SAASOTI

ALEXANDRA GAVSHINA¹, NADEZHDA MARYNICH¹ AND ALEXANDER SAVITSKY^{1, 2}

¹A.N. Bach Institute of Biochemistry, Research Center of Biotechnology of the Russian Academy of Sciences, Russia,

²Department of Chemistry, M.V. Lomonosov Moscow State University, Russia

apsavitsky@inbi.ras.ru

Abstract

Biphotochromic fluorescent protein (FP) SAASoti is a unique representative of GFP-family as its wild type gene can be irreversibly photoconverted ($\lambda=400$ nm) and reversibly photoswitched ($\lambda=470$ nm). In the course of this work, we obtained a series of SAASoti mutant forms with introduced single amino acid substitutions of cysteine residues (C21N, C117S, C117T, C72V, C106V, and C176A). Corresponding recombinant proteins were expressed in *E. coli* BL21 (DE3) cells, isolated and purified by chromatographic methods (combination of HIC and anion-exchange chromatography). Different physicochemical and fluorescent parameters (excitation/emission maxima, pKa values of the chromophore, molar extinction coefficient and quantum yield) of the obtained V127T SAASoti mutant variants were measured. C21 residue was found to be involved in the intermolecular dimerization of SAASoti at high concentrations, C72V SAASoti variant has an increased photoconversion (green-to-red) rate during 400 nm illumination, while C106V SAASoti demonstrates the maximum photoswitching rate between green fluorescent and dark states under 470 nm illumination. The photoswitching kinetics of C176A SAASoti follows a distinct mathematical model, indicating on different processes.

Phototransformable fluorescent proteins (PTFPs) are indispensable tools for localization and super-resolution techniques [1]. Such fluorescent markers should be monomeric and do not contain reactive amino acid residues. E.g., SH-groups of cysteine residues can form intra- and intermolecular disulfide bridges or become sulfoxidized. The difficulty is that sometimes cysteine-free variants of fluorescent proteins lose their photostability or become even non-fluorescent [2, 3, 4]. Interestingly, that in some cases substitution to cysteine residue in the chromophore microenvironment resulted in the several times more photostable variant [5]. Site-directed mutagenesis sometimes comes with uncontrollable and undesirable changes of other fluorescent properties.

Biphotochromic FP SAASoti can be irreversibly photoconverted between green and red fluorescent states under 400 nm illumination [6] and reversibly photoswitched between its green fluorescent and dark forms during 470 nm illumination [7]. Subsequently, we also determined conditions when the red SAASoti form can undergo reversible photoswitching [8]. Significantly, its biphotochromic nature can be observed on the wild type gene, while other biphotochromic proteins (IrisFP [9], NijiFP [10]) were obtained by site-directed mutagenesis of amino acid residues in the chromophore microenvironment (M159A, F173S). This fact makes SAASoti a unique representative of GFP-family. A monomeric variant of SAASoti (V127T) was also obtained and successfully applied as a genetically encoded fluorescent marker in PALM-technique [11], but V127T SAASoti tends to partial dimerization at high concentrations, and addition of reducing agent dithiothreitol (DTT, 10 mM) to the sample and to the system disrupts these interactions. These weak interactions between the monomeric subunits may prevent SAASoti from crystal packing, that is why we decided to evaluate the impact of individual cysteine substitutions in V127T SAASoti gene.

Five cysteine residues are located in the SAASoti structure – C21, C72, C106, C117 and C176 – and two of them (21 and 117) are surface-facing, while SH-groups of the others are oriented inside β -barrel. At first stage, we generated C21N/wt, C117S/wt, C117T/wt, C21N/V127T, and C117S/V127T SAASoti variants by site-directed mutagenesis, the corresponding recombinant proteins were isolated and characterized by gel-filtration chromatography. C21N and C117S substitutions in the wild type gene removed aggregates eluted in the bed volume, whereas C117T/wt variant demonstrated the same elution profile. C21N/V127T mutant form even at higher concentrations than V127T SAASoti exists as a monomer. Based on the previous data on moxDendra [12] and moxMaple [13] cysteine-free FPs, we suggested the following substitutions in the V127T SAASoti gene: C72V, C106V, and C176A. The corresponding mutant forms were obtained by site-directed mutagenesis; the recombinant proteins were expressed and purified.

At first, we measured different physicochemical parameters (excitation/emission maxima, pKa values of the chromophore, molar extinction coefficient and quantum yield) of the obtained V127T SAASoti mutant variants (C21N, C72V, C106V, and C176A). Introduced single point mutations led to the spectral shift of the red forms, and a significant increase in their pKa values, especially in the C176A SAASoti variant. C72V and C106V variants have the lowest value of molar extinction coefficient. At the next step, we recorded kinetics of green-to-red photoconversion as a function of the red fluorescence signal during 400 nm illumination. Substitution of the inside-

facing cysteine residues (C72, C106, and C176) led to the increase in the initial rate of the red form formation. One of the possible reasons explaining the phenomenon might be the fact, that pKa values of their green forms are also shifted to more alkaline pH values. In the case of C106V substitution, it also negatively affected its photostability. The increase in the initial rate suggests the reduction in 400 nm exposure time that will be less toxic to live cells. On-to-off photoswitching of the green form of the obtained mutant forms was investigated in the same manner but using blue light illumination with 470 nm LED (Fig. 1). In the first switching cycle, all except C176A SAASoti variant demonstrated the same drop in green fluorescence intensity.

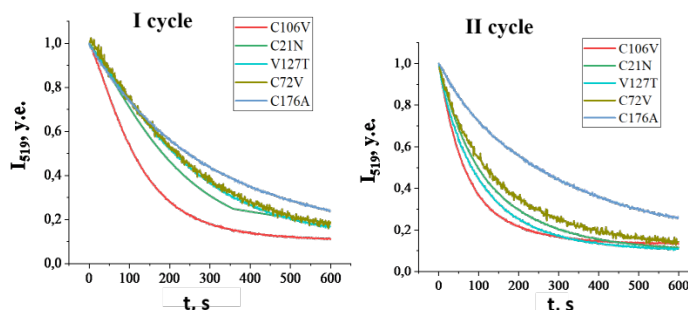


Figure 1: Kinetics of green fluorescence on-off photoswitching recorded under 470 nm (0.17 Wt/cm^2) illumination of different SAASoti variants ($10 \mu\text{M}$) in cuvette during 10 min. A) First switching cycle. B) Second switching cycle.

The process in those cases can be described by a bi-exponential function with the opposite sign of the components (Eq. 1), whereas the second and subsequent cycles follow the bi-exponential model (Eq. 2).

$$I = I_1 * \exp(-k_1 t) - I_2 * \exp(-k_2 t) + c \quad (1)$$

$$I = I_1 * \exp(-k_1 t) + I_2 * \exp(-k_2 t) + c \quad (2)$$

where I_1 and I_2 – pre-exponential coefficients, k_1 and k_2 – rate constants, c – background fluorescence signal. This fact might indicate on some photochemical modification of the protein (in all the cases except C176A SAASoti protein) during the first 470 nm illumination cycle, which leads to fluorescence kindling. C106V SAASoti variant also demonstrates the maximum photoswitching rate of the green form, whereas C176A SAASoti variant – the minimum.

Acknowledgements: The work was supported by the Russian Science Foundation project No 19-14-00373.

References

- [1] K. Nienhaus, G. U. Nienhaus, Fluorescent proteins for live-cell imaging with super-resolution, *Chem. Soc.Rev.*, vol. 43(4), p. 1088–1106, 2014.
- [2] L.M. Costantini, O.M. Subach, M. Jaureguierry-Bravo, V.V. Verkhusha, E.L. Snappa, Cysteineless non-glycosylated monomeric blue fluorescent protein, secBFP2, for studies in the eukaryotic secretory pathway, *Biochem. Biophys. Res. Commun.*, vol. 430(3), p. 1114–1119, 2013.
- [3] L. Costantini, M. Baloban, M. Markwardt et al., A palette of fluorescent proteins optimized for diverse cell environments, *Nature Communications*, vol. 6, p. 7670, 2015.
- [4] T. Suzuki, S. Arai, M. Takeuchi, C. Sakurai, H. Ebana et al., Development of Cysteine-Free Fluorescent Proteins for the Oxidative Environment, *PLoS ONE*, vol. 7(5), p. e37551, 2012.
- [5] H. Ren, B. Yang, C. Ma, Y.S. Hu, P.G. Wang, and L. Wang, Cysteine Sulfoxidation Increases the Photostability of Red Fluorescent Proteins, *ACS Chem. Biol.*, vol. 11(10), p. 2679–2684, 2016.
- [6] G. Lapshin, A. Salih, P. Kolosov, M. Golovkina, Y. Zavorotnyi, T. Ivashina, L. Vinokurov, V. Bagratashvili, A. Savitsky, Fluorescence color diversity of great barrier reef corals, *J. Innov. Opt. Heal. Sci.*, vol. 8, p. 1550028, 2015.
- [7] I.D. Solovyev, A.V. Gavshina, A.P. Savitsky, Reversible photobleaching of photoconvertible SAASoti-FP. *J. Biomed. Photon. Eng.*, vol. 3, 2017.
- [8] I.D. Solovyev, A.V. Gavshina and A.P. Savitsky, Novel Phototransformable Fluorescent Protein SAASoti with Unique Photochemical Properties, *Int. J. Mol. Sci.* v. 20, p. 3399, 2019.
- [9] V. Adam, M. Lelimosin, S. Boehme, G. Desfonds, K. Nienhaus, M.J. Field, J. Wiedenmann, S. McSweeney, G. U. Nienhaus, Structural characterization of IrisFP, an optical highlighter undergoing multiple photo-induced transformations. *Proc. Natl. Acad. Sci. USA* 2008, 105, 18343–18348.
- [10] V. Adam, B. Moeyaert, C.C David, H. Mizuno, M. Lelimosin, P. Dedecker, R. Ando, A. Miyawaki, J. Michiels, Y. Engelborghs, J. Hofkens. Rational Design of Photoconvertible and Biphotochromic Fluorescent Proteins for Advanced Microscopy Applications, *Chem. Biol.*, vol. 18, p. 1241–1251, 2011.
- [11] I.D. Solovyev, A.V. Gavshina, A.S. Katti, A.I. Chizhik, L.M. Vinokurov, G.D. Lapshin, T.V. Ivashina, M.G. Khrenova, I.I. Kireev, I. Gregor et al., Monomerization of the photoconvertible fluorescent protein SAASoti by rational mutagenesis of single amino acids, *Sci. Rep.*, vol. 8, p. 15542, 2018.
- [12] A.A. Kaberniuk, N.C. Morano, V.V. Verkhusha, E.L. Snapp / moxDendra2: an inert photoswitchable protein for oxidizing environments // *Chemical Communications (Cambridge)*. - 2017. Feb 9;53(13):2106-2109.
- [13] A.A. Kaberniuk, M.A. Mohr, V.V. Verkhusha, et al. / moxMaple3: a Photoswitchable Fluorescent Protein for PALM and Protein Highlighting in Oxidizing Cellular Environments // *Scientific Reports*. - 2018. - vol. 8. - p. 14738.

STUDY ON THE RELATIONSHIP BETWEEN REDUCED SCATTERING COEFFICIENT AND YOUNG'S MODULUS IN MICROWAVE ABLATION

ZHIYU QIAN¹, XIAOFEI JIN¹ AND YU FENG¹

¹Department of Biomedical Engineering, Nanjing University of Aeronautics and Astronautics, China

Abstract

Background and objective: Due to the conspicuous curative effect, minimally invasive, small side effects and low complications, microwave ablation(MWA) is considered as another effective method for the treatment of malignant tumors besides surgical excision, chemotherapy, radiotherapy and immunotherapy. This therapy has played a huge role in clinical cancer treatment [1,2], and has been widely used in treating liver cancer [3-5], lung cancer [6,7], kidney cancer [8], thyroid cancer [9], and other common tumors. In the current clinical treatment of tumors using MWA, although temperature can be used as an important reference index for evaluating the curative effect of ablation, it cannot fully reflect the biological activity status of tumor tissue during thermal ablation. Finding multi-parameter comprehensive evaluation factors to achieve real-time evaluation of therapeutic effects has become the key for precise ablation[10-14]. More and more scholars use the reduced scattering coefficient (μ'_s) and Young's modulus (E) to evaluate the treatment outcomes of MWA. However, the intrinsic relationship between these parameters is unclear. It is necessary and valuable to investigate the specific relationship between μ'_s and E during MWA.

Material and methods: The MWA experiment was conducted on porcine liver in vitro, the two-parameter simultaneous acquisition system was designed to obtain the reduced scattering coefficient and Young's modulus of the liver tissue during MWA (Figure 1). In the experiment, different levels of ablation power were used, namely, 50W, 60W, and 70W, and different ablation duration were used, namely, 3 minutes, 5 minutes, and 8 minutes. In addition, the distance between the fiber optic probe and the microwave ablation antenna also varied from 0.2cm, 0.5cm, 1cm, and to 1.5cm, respectively. Different combinations of ablation power, ablation duration, fiber optic probe and the microwave ablation antenna distance were use in the experiment. The relationship between reduced scattering coefficient and Young's modulus was investigated.

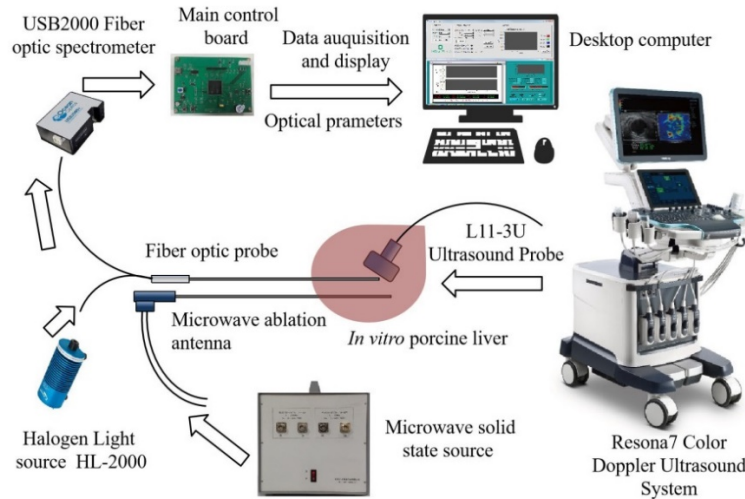


Figure 1: Microwave ablation real-time parameters acquisition system

Results: It can be found that with the increase of ablation duration at the fixed power, the Young's modulus gradually becomes larger at some regions as shown in the 2D shear wave image, which is characterized by color turning from blue to red, and the effective region is roughly elliptical (Figure 2). The effective region of the 2D shear wave image is gradually enlarging, and the average Young's modulus in the effective region is also increasing. More areas turning to red in the effective region in the shear wave image indicates that the tissue hardness is gradually expanding. It is also found that the trend of change of μ'_s is very similar to E in the process of MWA, that is, first increasing and then reaching a steady state (Figure 3), and in some experiments, there are synchronous changes (Figure 4). Based on this, the quantitative correlation model between E- μ'_s is established, enabling the estimation of Young's modulus of liver tissue based on reduced scattering coefficient. The maximum absolute error is 29.37 kPa and the minimum absolute error is 0.88 kPa.

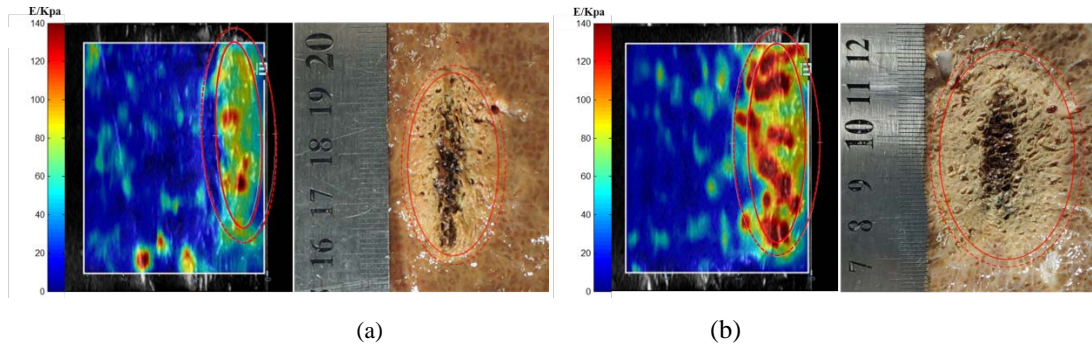


Figure 2:(a) Changes of E after 2 minutes at a fixed 50W power (b) Changes of E after 5 minutes at a fixed 50W power

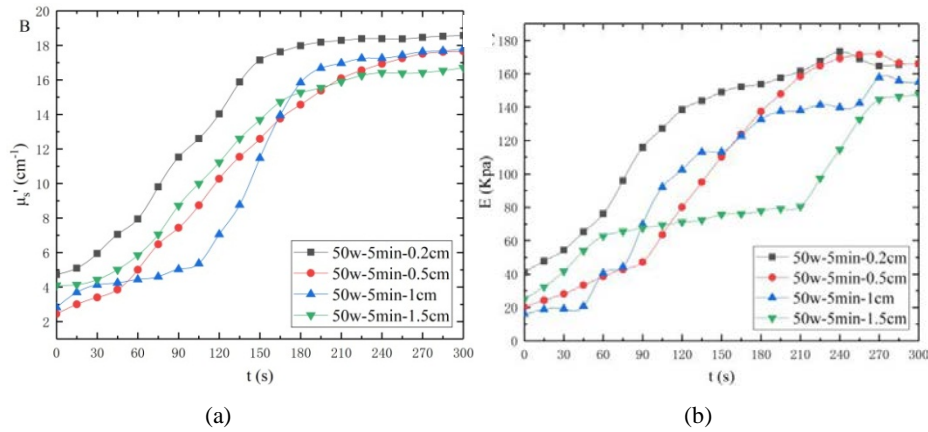


Figure 3:(a) Changes of μ'_s at different distances (0.2 cm, 0.5 cm, 1 cm, 1.5 cm) away from the MWA antenna (b) Changes of E at different distances (0.2 cm, 0.5 cm, 1 cm, 1.5 cm) away from the MWA antenna

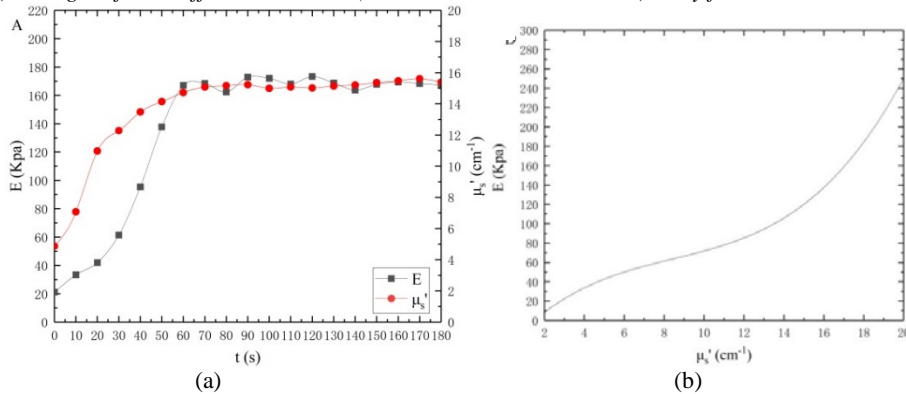


Figure 4:(a) Simultaneous changes of μ'_s and E (b) The correlation model curve

Conclusion: An effective E - μ'_s correlation model is proposed. The corresponding Young's modulus' average value can be calculated based on the reduced scattering coefficient under different states of ablation. The reduced scattering coefficient and Young's modulus of the liver tissue in the normal zone, transition zone, and coagulation zone are different, and the changes of μ'_s and E are closely related to the degree of tissue thermal damage. This study contributes to the further establishment of multi-parameter MWA effectiveness evaluation model. It is also valuable for clinically evaluating the ablation outcomes of tumor in real time.

References

- [1] Dou J P, Liang P, Yu J. Microwave ablation for liver tumors. *Abdom Radiol.* 2016,41(4):650-658.
- [2] Wells S A, Hinshaw J L, Lubner M G, et al. Liver Ablation: Best Practice[J]. *Radiol Clin North Am.* 2015, 53(5):933-971.
- [3] Ryu T, Takami Y, Wada Y, Wada Y, et al. Oncological outcomes after hepatic resection and/or surgical MWA for liver metastasis from gastric cancer. *Asian Journal of Surgery.* 2019,42(1):100-105.
- [4] De Cobelli F, Marra P, Ratti F, et al. Microwave ablation of liver malignancies: comparison of effects and early outcomes of percutaneous and intraoperative approaches with different liver conditions. *Med Oncol,* 2017, 34(4):49.
- [5] Meloni M F, Chiang J, Laeseke P F, et al. Microwave ablation in primary and secondary liver tumours: technical and clinical approaches. *Int J Hyperthermia.* 2016, 33(1):15-24.
- [6] Alhakim R A, Abtin F G, Genshaft S J, et al. Defining new metrics in microwave ablation of pulmonary tumors: ablation work and ablation resistance score. *J Vasc Interv Radiol,* 2016, 27(9):1380-1386.
- [7] Vogl T J, Roman A, Nour Eldin N E A, et al. A comparison between 915 MHz and 2450 MHz microwave ablation systems for the treatment of small diameter lung metastases. *Diagn Interv Radiol.* 2018, 24(1):31-37.

- [8] Cornelis F H, Marcelin C, Bernhard J C. Microwave ablation of renal tumors: A narrative review of technical considerations and clinical results. *Diagn Interv Radiol.* 2017, 98(4):287-297.
- [9] Yue W, Wang S, Yu S, et al. Ultrasound-guided percutaneous microwave ablation of solitary T1N0M0 papillary thyroid microcarcinoma: Initial experience. *Int J Hyperthermia.* 2014, 30(2):150-157.
- [10] Hu G, Qian Z, Ding S, et al. Study on the effective ablation volume of MWA of porcine livers. *Photonics Lasers Med.* 2013, 2(3):241-247.
- [11] Zhao J, Qian Z, Liu J, et al. Real-time assessment of microwave ablation efficacy by nir spectroscopic technique. *J Innov Opt Health Sci.*, 2014, 7(1):1350053.
- [12] Zhao J, Zhao Q, Jiang Y, et al. Feasibility study of modeling liver thermal damage using minimally invasive optical method adequate for in situ measurement. *J Biophotonics.* 2018:e201700302.
- [13] Bo X W, Li X L, Xu H X, et al. 2D shear-wave ultrasound elastography (SWE) evaluation of ablation zone following radiofrequency ablation of liver lesions: is it more accurate?. *Br J Radiol.* 2016, 89(1060):20150852.
- [14] Sugimoto K, Oshiro H, Ogawa S, et al. Radiologic-pathologic correlation of three-dimensional shear-wave elastographic findings in assessing the liver ablation volume after radiofrequency ablation. *World J Gastroenterol.* 2014, 20(33):11850-11855.

IMAGING PROCESSING OF LASER SPECKLE CONTRAST IMAGING OF BLOOD FLOW

WEIMIN CHENG^{1,2}, XIAOHU LIU^{1,2}, JINLING LU^{1,2}, AND PENGCHENG LI^{1,2}¹ Britton Chance Center for Biomedical Photonics, Wuhan National Laboratory for Optoelectronics, Huazhong University of Science and Technology² MoE Key Laboratory for Biomedical Photonics, School of Engineering Sciences, Huazhong University of Science and Technology

pengchengli@mail.hust.edu.cn

Abstract

Laser speckle contrast imaging (LSCI) is a wide-field, noninvasive, and noncontact optical imaging technology for mapping blood flow. Given the advantage of high spatio-temporal resolution, LSCI is widely used in blood flow imaging of the skin, retina, splanchnic organs, tumor, and brain in recent years. In practical applications, the spatial and temporal window size of speckle contrast analysis is usually expected to be minimized for higher spatio-temporal resolution. However, a reduced spatio-temporal window size of LSCI results in significant noise of K^2 owing to the statistical uncertainty [1]. To improve the measurement accuracy, a suitable denoising algorithm is required to enhance the signal-to-noise ratio (SNR) of LSCI. Furthermore, LSCI is well known to be highly sensitive to the motions induced by both environment and biological tissue itself. These disturbances will cause displacements of the speckle images, resulting in the error of speckle contrast estimation based on multiple frames of speckle images. Therefore, it is of urgent importance to minimize the impact of motion when LSCI is put into practical usage. We proposed a Manhattan distance based adaptive BM3D (MD-ABM3D) method to manage the complicated inhomogeneous noise in tLSCI image and improve the signal-to-noise ratio [2]. Manhattan distance improves the accuracy of the block-matching in strong noise, and the adaptive algorithm adapts to the inhomogeneous noise and estimates suitable parameters for improved denoising. As shown in Figure 1, the image-quality evaluation of MD-ABM3D for tLSCI ($t = 20$ frames) equals that of savg-tLSCI ($t = 60$ frames). It achieves high signal-to-noise ratio with a reduced number of sampling frames.

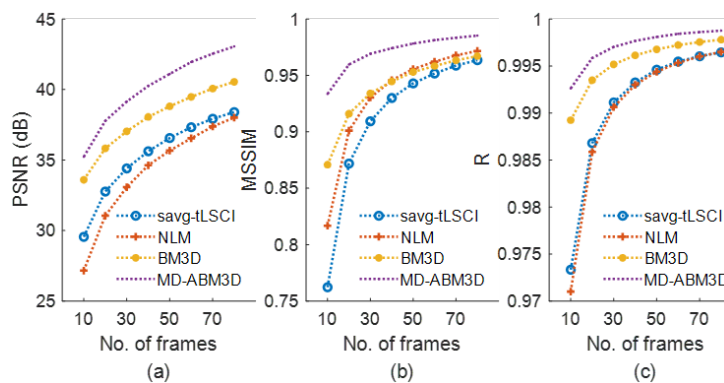


Figure 1 : Image-quality evaluation of each denoising method for tLSCI with temporal windows ($t = 10-80$ frames). (a)–(c) are evaluation of PSNR, MSSIM, and R, respectively[2]

However, the processing time of MD-ABM3D makes it difficult to realize real-time denoising. Furthermore, it is still difficult to obtain an acceptable level of SNR with a few raw speckle images given the presence of significant noise and artifacts. We proposed to train a feed-forward denoising convolutional neural network (DnCNN) for LSCI in a log-transformed domain to improve training accuracy and it achieves an improvement of 5.13 dB in the peak signal-to-noise ratio (PSNR). To decrease the inference time and improve denoising performance, we further proposed a dilated deep residual learning network with skip connections (DRSNet)[3]. The image-quality evaluations of DRSNet with five raw speckle images outperform that of spatially average denoising with 20 raw speckle images. DRSNet takes 35 ms (i.e., 28 frames per second) for denoising a blood flow image with 486×648 pixels on an NVIDIA 1070 GPU.

References

- [1] J. Hong, L. Shi, X. Zhu, J. Lu and P. Li, Laser speckle auto-inverse covariance imaging for mean-invariant estimation of blood flow, *Opt. Lett.*, 44(23):5812-5815, 2019
- [2] W. Cheng, J. Lu, X. Zhu, J., X. Liu, M. Li, P. Li, Dilated residual learning with skip connections for real-time denoising of laser speckle imaging of blood flow in a log-transformed domain, *IEEE Trans. Med. Imag.*, 39(5): 1582-1593, 2019
- [3] W. Cheng, X. Zhu, X. Chen, M. Li, J. Lu, P. Li, Manhattan distance based adaptive 3D transform-domain collaborative filtering for laser speckle imaging of blood flow, *IEEE Trans. Med. Imag.*, 38(7):1726-1735, 2019

TUMOR MICROENVIRONMENT-RESPONSIVE DRUG DELIVERY SYSTEMS

YI MA AND YUEQING GU

Department of engineering, China pharmaceutical university, China

Yima.ant@163.com

Abstract

It is known that most small-molecule anticancer drugs frequently suffer from poor efficacy caused by the development of drug resistance in cancer cells. Nanostructure formulations of these drugs can greatly mitigate drug resistance. However, the naked nanodrugs always cause systemic toxicity to normal organs due to non-specific drug release. Therefore, it would be an ideal strategy to encapsulate the naked nanodrugs into a biocompatible carrier for controlled release in the tumor environment. The intrinsic properties are the basis in the design of internal stimuli-responsive nanocarriers with the main focus on internal stimuli like pH value, glutathione (GSH) concentration, enzyme specific overexpression and hyperthermic. The characteristics of these triggers in pathological tissues are different from that in normal sites, thus the utility of these triggers provides new strategies in designing nanovehicles for drug delivery with higher on-target property and enhanced cellular uptake efficiency. This study aims to construct tumor microenvironment-responsive drug delivery systems to release anticancer agent in response to telomerase activity or GSH concentration. This technology will not only assist in the identification of cancer cells, its ability to intrinsically treat only cancerous cells will prevent the undesired death of healthy cells that is commonly seen using more conventional forms of chemotherapy. These findings will also help to inspire future designs of drug delivery systems that respond to cancer-specific biomolecules more accurately.

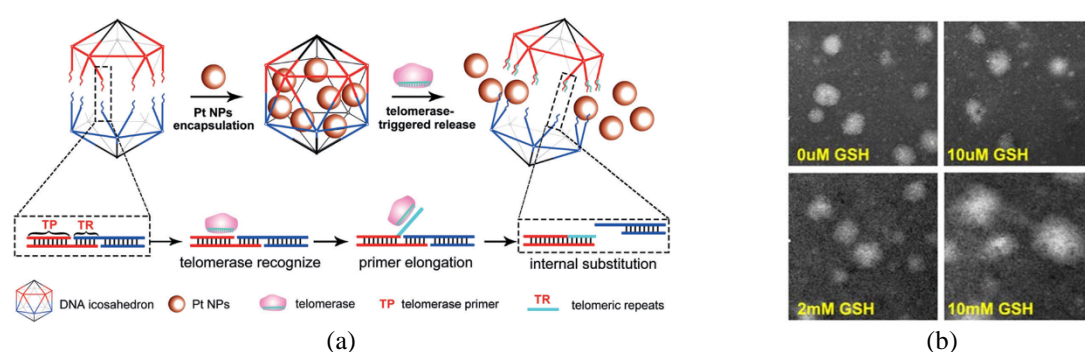


Figure: (a) Illustration of PtNP encapsulation and telomerase-triggered release from the DNA icosahedra (b) TEM images of CBN treated with different concentrations of GSH

References

- [1] Yi Ma, Zhaohui Wang, Yuxuan Ma, Zhihao Han, Min Zhang, Haiyan Chen and Yueqing Gu, A Telomerase-Responsive DNA Icosahedron for Precise Delivery of Platinum Nanodrugs to Cisplatin-Resistant Cancer [J]. *Angewandte Chemie*, 2018, 130(19): 5487-5491.
- [2] Zhaohui Wang, Yi Ma, Xiyuan Yu, Qi Niu, Zhihao Han, Han Wang, Tingting Li, Dingping Fu, Samuel Achilefu, Zhiyu Qian, Yueqing Gu, Targeting CXCR4–CXCL12 Axis for Visualizing, Predicting, and Inhibiting Breast Cancer Metastasis with Theranostic AMD3100–Ag2S Quantum Dot Probe. *Advanced Functional Materials*, 2018, 28(23): 1800732.
- [3] Min Zhang, Yi Ma, Zhaohui Wang, Zhihao Han, Weidong Gao, Qiumei Zhou and Yueqing Gu, A CD44-Targeting Programmable Drug Delivery System for Enhancing Chemotherapy to Drug-Resistant Cancer. *ACS Applied Materials & Interfaces* 2019, 11, 5851-5861.

SAPPHIRE FIBER BUNDLES FOR TERAHERTZ IMAGING WITH SPATIAL RESOLUTION BEYOND THE ABBE LIMIT

K.I. ZAYTSEV^{1,2,3*}, G.M. KATYBA^{2,4}, N.V. CHERNOMYRDIN^{1,2,3}, I.N. DOLGANOVA^{2,3,4}, A.S. KUCHERYAVENKO^{1,2}, A.N. ROSSOLENKO⁴, V.V. TUCHIN^{5,6}, V.N. KURLOV^{3,4}, AND M. SKOROBOGATYIY⁷

¹*Prokhorov General Physics Institute of RAS, Russia*

²*Bauman Moscow State Technical University, Russia*

³*Institute for Regenerative Medicine, Sechenov University, Russia*

⁴*Institute of Solid State Physics of RAS, Russia*

⁵*Saratov State University, Russia* ⁶*Institute of Precision Mechanics and Control of RAS, Russia*

⁷*Department of Engineering Physics, Polytechnique Montreal, Canada*

*E-mail: kirzay@gmail.com

Abstract

While fiber bundles attract much interest in optics, their resolution is limited by the individual fiber size, which can be as large as a wavelength λ for common fiber optics materials. In order to increase fiber bundle resolution, in our work, high-refractive-index sapphire fibers ($n > 3$), which were fabricated using the Edge-defined Film-fed Growth (EFG) technique [1], are employed in the terahertz (THz) range. They ensure strong confinement of the guided modes and enable a fiber bundle resolution beyond the 0.62λ Abbe limit of free space optics [2]. A sapphire fiber bundle is fabricated and its advanced resolution is experimentally demonstrated, using both analysis of the pair correlation function of the disordered fiber packing and continuous-wave THz imaging. The resolution varies across the aperture with the mean value of 0.53λ , while it is as low as 0.3λ at certain regions of the bundle. The developed principles can be translated to any spectral range where high-refractive index fiber optics materials are available.

Acknowledgements

This work was partially supported by the Russian Science Foundation, Projects #17-79-20346 and #19-12-00402.

References

- [1] Progress in Crystal Growth & Characterization of Materials 64(4), 133–151 (2018), DOI: 10.1016/j.pcrysgrow.2018.10.002.
[2] Advanced Optical Materials, in press (2020), DOI: 10.1002/adom.202000307.

MONTE CARLO SIMULATION OF THE COVID-19 SPREAD IN EARLY AND PEAK STAGES IN DIFFERENT REGIONS OF THE RUSSIAN FEDERATION USING AN AGENT-BASED MODELLING

MIKHAIL KIRILLIN¹, EKATERINA SERGEEVA¹, ALEKSANDR KHILOV¹, DARIA KURAKINA¹, AND NIKOLAYSAPERKIN²

¹*Institute of Applied Physics RAS, Russia,*
²*Privolzhsky Research Medical University, Russia*

mkirillin@yandex.ru

Abstract

The COVID-19 outbreak of the beginning of 2020 has grown into a full-scale world crisis, which is still continuing. Minimization of losses requires adequate systemic aids for the disease spread prevention, which, in turn, requires adequate models allowing to predict the effect of different factors to disease spread. Traditional simulation approaches based on derivatives of a SIR model, although being quite efficient, suffer from not accounting for random factors. Agent-based models provide a convenient solution which allows accurately accounting for such factors as age structure of population, feature of self-isolation strategies and testing protocols, presence of super-spreaders etc. In this paper we report on the results of predicting the spread of COVID-19 in several representative regions of Russia. Our approach is based on an agent-based model with a general pool that includes a model of the population testing strategy. The model accounts for the following key epidemiologic characteristics: population age distribution, distributions of infestation period, manifestation period, and age-dependent probability of critical disease currency. It is demonstrated, that despite local features of different regions, the daily case curves can be predicted well for different territories with the same model parameters, except the initial number of infected, which serve as a tuning parameter of the model.

Introduction

Prediction of further development of COVID-19 outbreak and timely introduction of preventive measures require reliable tools for epidemic spread simulations. Several classes of models are currently employed for the prognosis of the spread of infections.

Regression models are known to provide us with rapid estimations of the spread of infections [1,2]. Non-adaptive models allow obtaining the prognosis for any chosen period of time, however, they ignore local perturbations of epidemical characteristics, thus they are not suitable for short-term prognosis. On the contrary, adaptive models are predominantly employed for short-term prognosis only. Autoregressive moving average model is applicable for short-term prognosis [3], while autoregressive integrated moving average model is applicable both for short-term and long-term prognosis [4]. Dynamic Bayesian networks are employed only for short-term prognosis and predominantly in the form of Markov models [5]. Neural networks and other machine learning based methods can be applied only for short-term prognosis. Only feedforward neural networks and backpropagation algorithm are applicable for the prognosis of infections spread [6].

Dynamic systems based on differential equations, which are the class of compartmental models, are employed for long-term prognosis. The pioneering work by Kermack and McKendrick [7] proposed SIR model, in which the population is divided into three groups — susceptible (S), infected (I), recovered (R) — and their interaction is described with non-linear differential equations. Modern compartmental models employ bigger number of groups, accounting for exposed (E), hospitalized (H), critical (C), dead (D), and those at the quarantine (Q) or isolation (J). Compartmental models are widely employed for the modeling of the spread of coronavirus-induced infections (SARS, MERS, COVID-19). For example, SEIR model has been applied for modeling of COVID-19 spread in African countries [8], Iran [9], Indonesia [10], Spain and Italy [11]. Early COVID-19 spread and the efficacy of governmental measures are discussed in paper [12] also with the application of SEIR model. Compartmental models are easy to construct, but they do not account for random factors of the spread of infections and individual characteristics of population members.

Individually-oriented models include so-called agent-based models, which can be applied both for short-term and long-term prognosis of the spread of infection. Every member of population (agent) is described by number of constant and variable characteristics, and the rules of interactions between the agents are determined. Agent-based models were proved to be effective in the description of the propagation of infections, such as Ebola [13] and flu [14], for different sizes of population. Agent-based models were also applied for the modeling of COVID-19 spread, for example, the modeling of the development and the regress of the infection in the city of Helsinki is described in [15]. NotreDame-FRED model [16], developed at the University of Notre Dame, is based on previously developed at the University of Pittsburgh FRED model (Framework for Reconstructing Epidemic Dynamics) for the prediction of flu pandemics in the

year 2009. The modeling of the second wave of COVID-19 after the cancellation of the restrictive measures was also performed within agent-based model [17].

The aim of this paper is the development of an agent-based model capable of predicting the progress of the COVID-19 burst in different regions of the Russian Federation. Another important problem to be resolved in this study is the determination of the key model parameters that provide the agreement of the simulated dynamics and actual statistics on daily new infection cases and deaths associated with COVID-19.

Agent-Based Covid-19 Spread Model

In this study, we fitted a general pool model, in which all the individuals (agents) may interact with each other. Conditional on a simulated scenario, each agent has the following binary states, which values are governed by the Monte Carlo based random values: susceptible, infected, contagious, with disease manifestations, critical, recovered. Time resolution of a simulation is one day, since general statistics on newly registered cases and deaths is available on the daily basis. The model accounts for the population age structure based on the information on different disease progression in different age groups. Typical lengths of disease manifestation, progression, critical, and symptomless periods are introduced in accordance with the available data.

The average number of individuals R , to which an infected agent may transmit the infection within one week given that no restriction measures are applied, is considered as the main model parameter directly related to infection transmission coefficient. Given that the probabilities to be infected from different agents are independent, the contagination probability for an agent interacting with the general pool in a particular day is calculated as:

$$P = \frac{RN_i}{7N_t},$$

where N_i is the number of infected individuals presenting in the general pool in the current day and N_t is the total number of agents in the considered population. The N_t number is chosen in accordance with the population of the simulated region.

The model accounts for the efficiency of the following restrictive measures introduced by employing a so-called self-isolation index. This is an empirical value introduced by Yandex (Russia), which represents a cumulative parameter reflecting population activity based on both traffic information and activities in different internet services. The isolation index varies in the range between 0 and 5, and in simulation it is assumed that the index is proportional to the percentage of agents that obey the restrictive rules and do not interact with the general pool in the current day. For the days, when the restriction measures are applied, official data on self-isolation index by Yandex are employed. For the prognosis, the two approaches were applied. In the first one, the extrapolation of the detected dynamics of the self-isolation index was employed. Since general trend at the day of the prognosis generation demonstrated the decreases of the self-isolation index with time, this scenario is attributed as “negative”. An alternative scenario was produced by the introduction of constant self-isolation index values for particular time intervals. Since this scenario accounts for constant self-isolation index, it was attributed as “positive”.

The introduced rules of testing are an important part of the model, since the real data that are usually compared with the results of simulation are daily statistics on number of newly revealed cases and deaths. Obviously, the former number depends on the testing strategy within a given region and, therefore, its accurate description is of huge importance. In the model, the number of daily tests for each region is either taken from official statistics or determined from the daily number of cases for the entire Russian Federation in proportion to the region population. The testing model also accounts for the increase in the accuracy of COVID-19 tests with time.

Depending on the introduced anti-epidemic measures accounted in the simulation, an agent also may get a binary status “isolated”, if the agent has a positive COVID-19 test, or under the self-isolation, if in current day he/she follows the restrictive measures and does not interact with the general pool.

Results

Figures 1a,b and 1 c,d demonstrate the results of simulations of the negative and positive scenarios of the epidemic progress in Moscow ($N_t = 11.4 \cdot 10^6$) and Novosibirskaya oblast (Novosibirsk region) ($N_t = 2.7 \cdot 10^6$), respectively. To provide a best-fit scenario, we manipulated with two key parameters of the model, namely, the number of initial infected agents, percentage of deaths among agents in the critical state p_d and virus transmission coefficient R . Each scenario was constructed by averaging five scenarios that are the closest to the real statistical data over a total of 20 realizations with the same parameters. Due to the stochastic origin of the developed model, similar starting parameters may result in totally different scenarios of an epidemic progress.

In Fig. 1 circles show the original data employed for determination of the model fitting parameters, while triangles denote the official statistical data reported after prediction by the model. It is worth noting that the prediction for Moscow was obtained for the same transmission coefficient value $R = 4.6$ and death percentage of $p_d = 3\%$. Of note, the prediction was made during the epidemic peak in Moscow (Fig. 1a,b), in this connection, the positive scenario for daily newly

registered cases provides the best fit supposing preservation of the restrictive measures combined with the increase in the accuracy of testing.

Simulation results for Novosibirskaya oblast demonstrate the prediction abilities of the model for regions with relatively small number of confirmed COVID-19 cases and single deaths. The main advantage of our approach was that the values of fitting parameters of the epidemic for Novosibirskaya oblast were taken from fitting results from Moscow, thus, only the number of initial cases for the first day of consideration was fitted. These results suggest that the general epidemic spread parameters are quite close for different regions.

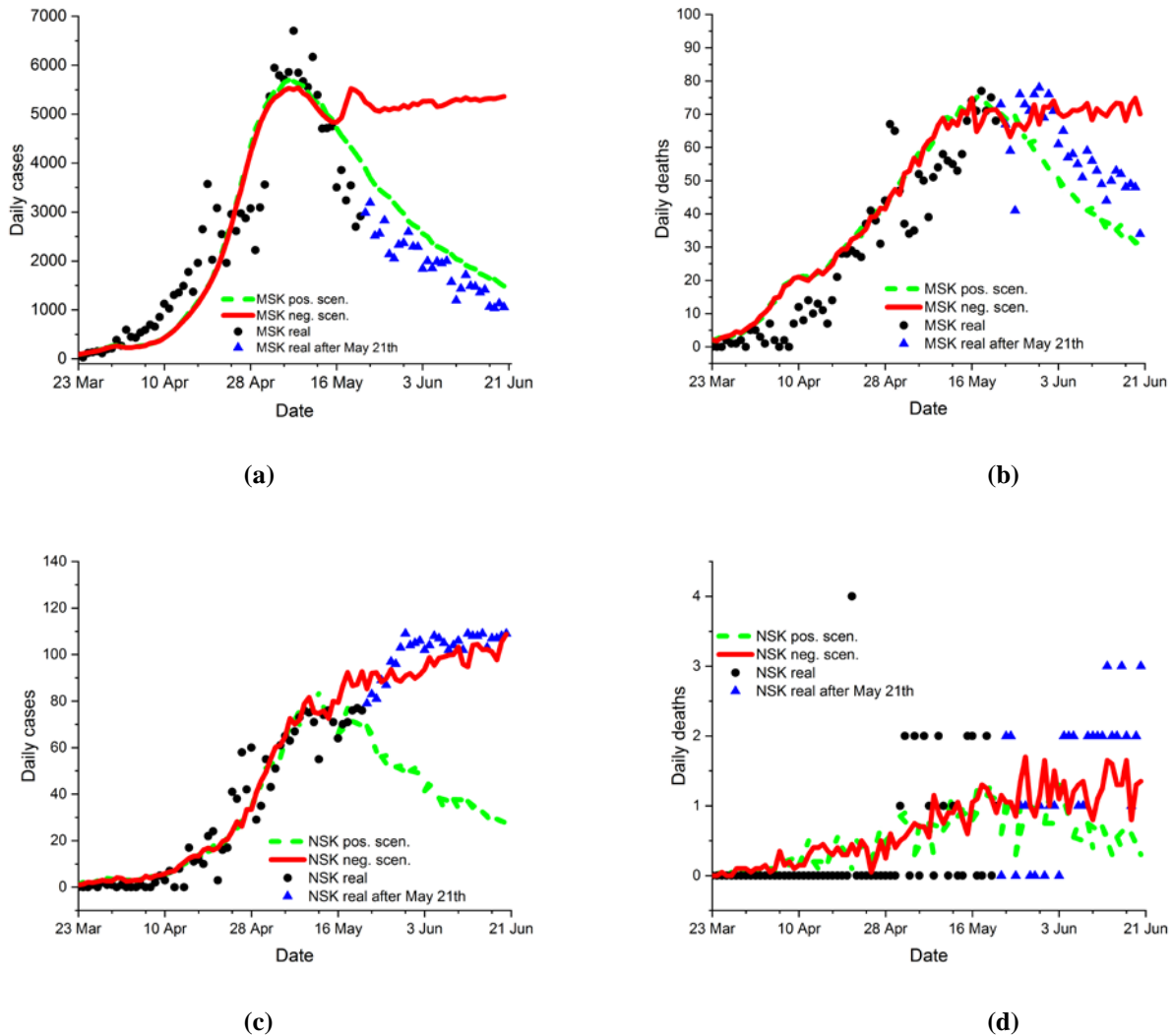


Figure 1: Comparison of simulated (positive and negative scenarios) and real statistical data for daily numbers of newly revealed COVID-19 (a,c) and lethal COVID-19 associated (b,d) cases in Moscow (a,b) and Novosibirskaya oblast (c,d) in the period 23 March – 23 June 2020..

Conclusion

In this paper we presented an agent-based model of COVID-19 epidemic spread widely employing the rigorous methodology of Monte Carlo simulation principles. The model is able to account for the age-dependent disease development, restrictive measures as well as testing system. It was validated on the statistical data for daily new cases and deaths which were reported from two representative regions of Russia, such as the Moscow city and Novosibirskaya oblast. Moreover, 1-month-long predictions of further epidemic spread were made on 21, May, 2020. For each region we considered two scenarios, “negative” and “positive”, considering weakening or preservation of the introduced restrictive measures, respectively. It was shown, that the epidemic spread fitting parameters derived from simulations for Moscow could be successfully incorporated for prognosis of the disease spread in other region.

References

[1]. H.S. Burkom, S.P. Murphy, and G. Shmueli, “Automated time series forecasting for biosurveillance,” *Statistics in medicine*, 26(22), pp. 4202-4218, 2007.

- [2]. J.C. Brillman et al., "Modeling emergency department visit patterns for infectious disease complaints: results and application to disease surveillance," *BMC medical informatics and decision making*, 5(1), p. 4, 2005.
- [3]. D. Lai, "Monitoring the SARS epidemic in China: a time series analysis," *Journal of Data Science*, 3(3), pp. 279-293, 2005.
- [4]. J. Diaz-Hierro et al., "Evaluation of time-series models for forecasting demand for emergency health care services," *Emergencias*, 24(3), pp. 181-188, 2012.
- [5]. S. Unkel et al., "Statistical methods for the prospective detection of infectious disease outbreaks: a review," *Journal of the Royal Statistical Society: Series A (Statistics in Society)*, 175(1), pp. 49-82, 2012.
- [6]. R. Kiang et al., "Meteorological, environmental remote sensing and neural network analysis of the epidemiology of malaria transmission in Thailand," *Geospatial health*, 1(1), pp. 71-84, 2006.
- [7]. W.O. Kermack, and A.G. McKendrick, "A contribution to the mathematical theory of epidemics," *Proceedings of the royal society of London. Series A, Containing papers of a mathematical and physical character*, 115(772), pp. 700-721, 1927.
- [8]. Z. Zhao et al., "Prediction of the COVID-19 spread in African countries and implications for prevention and controls: A case study in South Africa, Egypt, Algeria, Nigeria, Senegal and Kenya," *Science of the Total Environment*, 729, p. 138959, 2020.
- [9]. N. Ghaffarzadegan, and H. Rahmandad, "Simulation-based estimation of the early spread of COVID-19 in Iran: actual versus confirmed cases," *System Dynamics Review*, 36(1), pp. 101-129, 2020.
- [10]. S. Annas et al., "Stability analysis and numerical simulation of SEIR model for pandemic COVID-19 spread in Indonesia," *Chaos, Solitons & Fractals*, 139, p. 110072.
- [11]. L. López, and X. Rodo, "A modified SEIR model to predict the COVID-19 outbreak in Spain and Italy: simulating control scenarios and multi-scale epidemics," *medRxiv:20045005*, 2020.
- [12]. Y. Fang, Y. Nie, and M. Penny, "Transmission dynamics of the COVID-19 outbreak and effectiveness of government interventions: A data-driven analysis," *Journal of medical virology*, 92(6), pp. 645-659, 2020.
- [13]. S. Siettos et al., "Modeling the 2014 Ebola virus epidemic—agent-based simulations, temporal analysis and future predictions for Liberia and Sierra-Leone," *PLoS currents*, 7, 2015.
- [14]. H. Arduin et al., "An agent-based model simulation of influenza interactions at the host level: insight into the influenza-related burden of pneumococcal infections," *BMC infectious diseases*, 17(1), p. 382, 2017.
- [15]. J.T. Tuomisto et al., "An agent-based epidemic model REINA for COVID-19 to identify destructive policies," *medRxiv:20047498*, 2020.
- [16]. Retrieved from https://github.com/confunguido/covid19_ND_forecasting
- [17]. M. D'Orazio, G. Bernardini, and E. Quagliarini, "How to restart? An agent-based simulation model towards the definition of strategies for COVID-19 second phase in public buildings," *arXiv:2004.12927*, 2020.

MACS: RAPID AQUEOUS CLEARING SYSTEM FOR THREE-DIMENSIONAL MAPPING OF INTACT ORGANS

JINGTAN ZHU, TINGTING YU, YUSHA LI, JIANYI XU, YISONG QI, YINGTAO YAO, YILIN MA, PENG WAN, ZHILONG CHEN, XIANGNING LI, HUI GONG, QINGMING LUO, DAN ZHU*

¹Britton Chance Center for Biomedical Photonics, Wuhan National Laboratory for Optoelectronics, Huazhong University of Science and Technology, China

²MoE Key Laboratory for Biomedical Photonics, Huazhong University of Science and Technology, Wuhan 430074, China
Email: zhujingtang@hust.edu.cn

Abstract

Tissue optical clearing techniques have provided important tools for large-volume imaging. Aqueous-based clearing methods are known for good fluorescence preservation and scalable size maintenance, but are limited by long incubation time, or insufficient clearing performance, or requirements for specialized devices. Additionally, few clearing methods are compatible with widely-used lipophilic dyes while maintaining high clearing performance. Here, to address these issues, m-xylylenediamine (MXDA) is firstly introduced into tissue clearing and used to develop a rapid, highly efficient aqueous clearing method with robust lipophilic dyes compatibility, termed MXDA-based Aqueous Clearing System (MACS). MACS can render whole adult brains highly transparent within 2.5 d and is also applicable for other intact organs. Meanwhile, MACS possesses ideal compatibility with multiple probes, especially for lipophilic dyes. MACS achieves three-dimensional (3D) imaging of the intact neural structures labelled by various techniques. Combining MACS with DiI labelling, MACS allows reconstruction of the detailed vascular structures of various organs and generates 3D pathology of glomeruli tufts in healthy and diabetic kidneys. Therefore, MACS provides a useful method for 3D mapping of intact tissues and is expected to facilitate morphological, physiological and pathological studies of various organs.

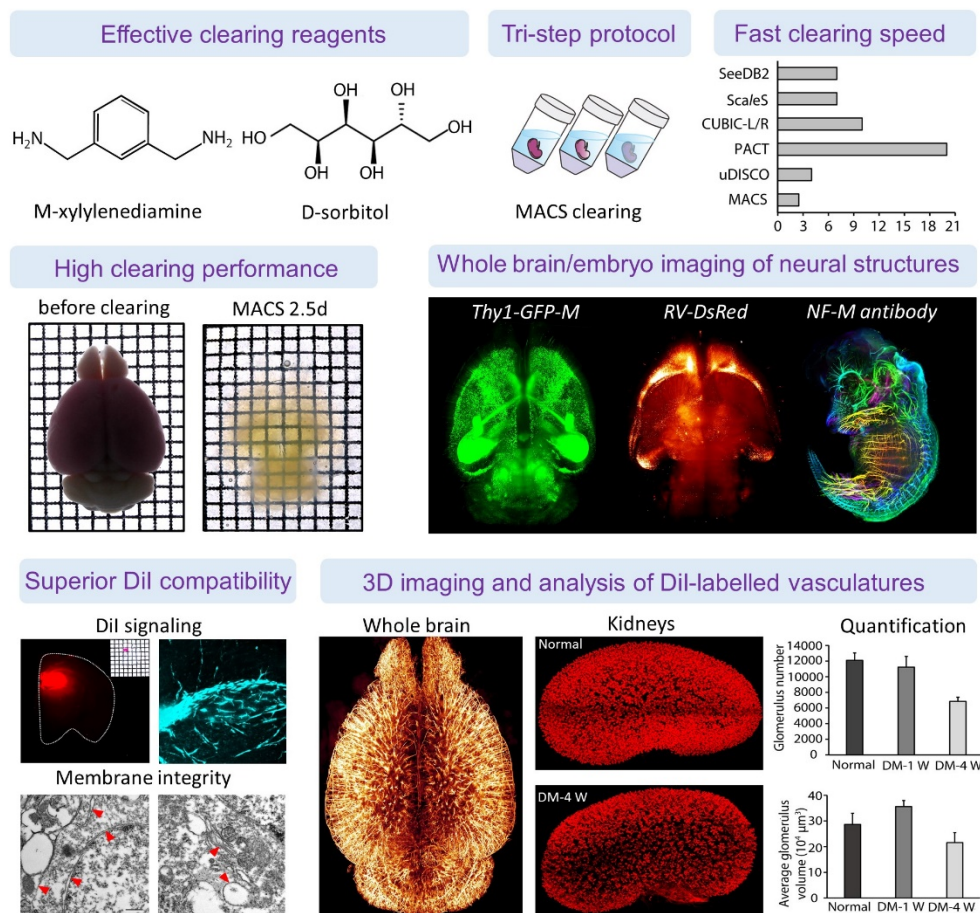


Figure 1: Overview of MACS clearing method.

RECENT ADVANCES IN OPTICAL IMAGING FOR PHOTODYNAMIC THERAPY

BUHONG LI

Key Laboratory of OptoElectronic Science and Technology for Medicine of Ministry of Education, Fujian Provincial Key Laboratory of Photonics Technology, Fujian Normal University, Fuzhou, 350117, P. R. China.

*E-mail: bhli@fjnu.edu.cn

Abstract

Photodynamic therapy (PDT) is a clinically-approved, minimally-invasive therapeutic procedure that utilizes photosensitizer to generate cytotoxic reactive singlet oxygen for the treatment of a wide variety of malignant and nonmalignant conditions. For PDT applications, the robust and comprehensive individualized dosimetry is essential for achieving satisfactory outcomes but remains a challenge, particularly for clinical translation. The main dosimetric parameters for predicting the PDT efficacy include the delivered light dose, the administrated photosensitizer distribution and concentration, the tissue oxygen concentration, the amount of singlet oxygen generation and the resulting biological responses. In this talk, the emerging optical imaging techniques that in use or under development for monitoring dosimetric parameters during PDT treatment were presented. In particular, laserspeckle imaging, laser Doppler imaging, optical coherence tomography and singlet oxygen luminescence imaging will be highlighted. In addition, the future challenges in developing real-time and non-invasive optical techniques for monitoring PDT dosimetric parameters will be discussed.

References

- [1] Lin L, Lin H, Chen D, Xie S, Gu Y, Wilson BC, Li B. Imaging of singlet oxygen luminescence in blood vessels. *SPIE Newsroom*. 2014, 10.1117/2.1201405.005511.
- [2] Li B, Lin L, Lin H, Wilson BC. Photosensitized singlet oxygen generation and detection: Recent advances and future perspectives in cancer photodynamic therapy. *Journal of Biophotonics*. 2016, 9:1314-25.
- [3] Pfitzner M, Schlothauer JC, Lin L, Li B, Röder B. Singlet oxygen luminescence imaging-a prospective tool in bioscience? in *Imaging in Photodynamic Therapy*. 2017, CRC Press, 67-87.
- [4] Yang S, Chen H, Liu L, Chen B, Yang Z, Wu C, Hu S, Lin H, Li B, Qu J. OCT imaging detection of brain blood vessels in mouse, based on semiconducting polymernanoparticles. *Analyst*, 2017, 142:4503-4510.
- [5] Wei Z, Wu M, Li Z, Lin Z, Zeng J, Sun H, Liu X, Liu J, Li B, Zeng Y. Gadolinium-doped hollow CeO₂-ZrO₂ nanoplatform as multifunctional MRI/CT dual-modal imaging agent and drug delivery vehicle. *Drug Delivery*, 2018, 25: 353-363.
- [6] Shen Y, Liang F, Niu Y, Lin H, Gu Y, Wilson BC, Li B. Monitoring vascular targeted PDT response with multimode optical imaging. *Proc. SPIE*, 2019, 10879:1087906.
- [7] Lin L, Lin H, Shen Y, Chen D, Gu Y, Wilson BC, Li B, Singlet oxygen luminescence image in blood vessels during vascular targeted photodynamic therapy. *Photochemistry and Photobiology*. 2020, 96(3): 646-651.
- [8] Xu Teng, Feng Li, Chao Lu, Buhong Li, Carbon dots-assisted luminescence of singlet oxygen: generation dynamics but not cumulative amount of singlet oxygen responsible for photodynamic therapy efficacy. *Nanoscale Horizons*, 2020, 5(6): 978-985.
- [9] Xianglian Liao, Ziguo Lin, Yi Shen, Huiyun Lin, Da Zhang, Xiaolong Liu and Buhong Li. Self-assembled metallo-supramolecular nanoflowers for NIR/acid-triggered multidrug release, long-term tumor retention and NIR-II fluorescence guided-phototherapy. *Chemical Engineering Journal*. 2020, 400: 125882.
- [10] Xu X, Lin L, Li B. Automatic protocol for quantifying the vasoconstriction in blood vessel image. *Biomedical Optics Express*. 2020, 11(4): 2122-2136.

ANGIOGENESIS AND GLIAL RESPONSES AFTER NEAR-INFRARED LIGHT ATTENUATES AB BURDEN AND ALLEVIATES COGNITIVE IMPAIRMENTS IN APP/PS1 MICE

LECHAN TAO¹ AND XUNBIN WEI^{1,2}

¹ *Med-X Research Institute and School of Biomedical Engineering, Shanghai Jiao Tong University, China.*

² *Department of Biomedical Engineering, Peking University, China.*

xwei01@sjtu.edu.cn

Abstract

Alzheimer's disease (AD), a chronic debilitating neurodegenerative disease, is associated with loss of motivation, memory and spatial learning difficulties, as well as language disorders[1]. The pathology of AD is poorly understood. Nevertheless, it is widely believed that the amyloid- β ($A\beta$)-containing senile plaques is one of the neuropathological hallmarks of AD[2]. Much of this work centered on the biosynthesis of $A\beta$ and factors that influence its production and deposition. $A\beta$ is derived from the regulated intracellular proteolysis of amyloid precursor protein (APP), which is hydrolyzed by the sequential action of the γ - and β -secretases. Normally $A\beta$ peptides contain 39 to 43 amino acids. A number of studies have shown that mutations in the APP gene or in presenilins result in increased β -secretase cleavage and production of both $A\beta$ 1-40 and $A\beta$ 1-42, which are the major peptides associated with AD plaque formation via aggregation[3]. "The amyloid hypothesis" suggests that the accumulation of $A\beta$ peptides serves as the central event triggering neuron degeneration[4]. Plaque reduction is seen as an indicator of effective therapies.

In 1903, the Danish Niels Finsen won the third Nobel Prize in Physiology and Medicine for the treatment of lupus erythematosus with red light, and since then opened a new chapter of light therapy. The biological effects of low-level lasers on tissue or body were first illustrated by Hungarian physician Endre Mester. In 1967, Mester et al. discovered that the ruby laser (694 nm) could promote hair regeneration and wound healing in mice[5]. It opened a new way in the medical field and developed into "low-dose laser therapy", also known as low-level laser treatment. It refers to irradiate tissue or body with the low-level laser, resulting in not irreversible damage but a series of physiological and biochemical responses to regulate tissues or the body, ultimately ameliorating or curing the diseases[6]. Biological effects of NIR light include wound healing, pain reduction, and alleviation of oral mucositis[7, 8]. Effects such as cytoprotection, cellular proliferation and growth factor release have also been reported[9]. Accumulating studies have explored the effect of light on brain diseases, such as AD [10-15], Parkinson's disease [16-18], depression [19, 20], stroke [21-23] and traumatic brain injury[24-26]. Low power laser irradiation can rescue neurons loss and dendritic atrophy via upregulation of BDNF in both $A\beta$ -treated hippocampal neurons and cultured APP/PS1 mouse hippocampal neurons[27]. The 808-nm laser can also attenuate $A\beta$ -induced reactive gliosis and proinflammatory cytokines production in the hippocampal CA1 region of the rat injected with $A\beta$ 1-42. In addition, PBM ameliorates $A\beta$ -induced oxidative stress by suppressing glucose-6-phosphate dehydrogenase and nicotinamide adenine dinucleotide phosphate oxidase activity [28].

Although many studies have explored the effects of PBM on $A\beta$ -mediated neuronal dysfunction, glial activation, inflammation and oxidative stress. Few studies have explored the mechanisms of PBM on the $A\beta$ clearance. Degradation of cerebral $A\beta$ via efflux across the blood-brain barrier (BBB) into the circulation, and uptake by macrophages, microglia and astrocyte phagocytosis are two main mechanisms of cerebral $A\beta$ clearance[29]. Here, we hypothesized that NIR light could reduce the $A\beta$ burden in the brain of APP/PS1 mice by activating glial responses and promoting cerebral angiogenesis to improve memory and cognitive deficits. To test this, we studied the biological responses of the cerebral vessel and glial cells in the APP/PS1 mice to the NIR light at different pathological progression and its effects on the $A\beta$ clearance. For light treatment, the mice in light groups were placed in the light device and received irradiation of 6 minutes per day for consecutive 60 days, with a wavelength between 1040 nm and 1090 nm. At the last 10 days of irradiation treatment, we tested the memory and learning ability of all mice via behavioral tests. Following the behavioral experiments, mice were humanely sacrificed and prepared to evaluate the effect of NIR light on alterations of glial cells and vessels.

Our results showed that NIR light significantly improved the performance of behavior tests in mice at 12 months old, as well as decreased the $A\beta$ burden of AD mice at different pathological progression. The results suggested that NIR light promoted angiogenesis in the cortex through different VEGF signaling pathways which changed with pathological progression. The vessel density was also positively correlated with the clearance of $A\beta$ deposition, indicating that PBM could reduce $A\beta$ burden via increase cerebral vessel density. Likewise, the microglia and astrocyte in the cortex had unique responses to NIR light. In mice at 6 months old, alteration of microglia morphology was observed, suggesting the increase in $A\beta$ phagocytosis of mice in light group. Meanwhile, there was also a significant decrease in reactive astrocyte. In mice at 12 months old, microglia displayed no differences in morphology among groups, while light recruited more microglia around $A\beta$ which contributed to the clearance of $A\beta$ in the brain. Finally, we also found out that NIR light significantly reduced neurodegeneration in the CA1 region of mice at 12M, which was critical to learning and

memory. Overall, our findings suggest that NIR light could reduce cerebral A β levels and A β -mediated neurotoxicity of APP/PS1 mice through the promotion of angiogenesis and activation of microglia and astrocyte in the brain. It provides new insights into the clinical application of NIR on treating AD.

References

- [1] L. Vermunt, S.A.M. Sikkes, A. van den Hout, R. Handels, I. Bos, W.M. van der Flier, S. Kern, P.J. Ousset, P. Maruff, I. Skoog, F.R.J. Verhey, Y. Freund-Levi, M. Tsolaki, A.K. Wallin, M. Olde Rikkert, H. Soininen, L. Spuru, H. Zetterberg, K. Blennow, P. Scheltens, G. Muniz-Terrera, P.J. Visser, I. Alzheimer Disease Neuroimaging, A.R. Group, I.D.s. groups, Duration of preclinical, prodromal, and dementia stages of Alzheimer's disease in relation to age, sex, and APOE genotype, *Alzheimers Dement* 15(7) (2019) 888-898.
- [2] J. Hardy, D. Allsop, Amyloid deposition as the central event in the aetiology of Alzheimer's disease, *Trends Pharmacol Sci* 12(10) (1991) 383-8.
- [3] Y. Chen, L. De Taboada, M. O'Connor, S. Delapp, J.A. Zivin, Thermal effects of transcranial near-infrared laser irradiation on rabbit cortex, *Neurosci Lett* 553 (2013) 99-103.
- [4] K. Hsiao, P. Chapman, S. Nilsen, C. Eckman, Y. Harigaya, S. Younkin, F. Yang, G. Cole, Correlative memory deficits, Abeta elevation, and amyloid plaques in transgenic mice, *Science* 274(5284) (1996) 99-102.
- [5] B. Gu, S. Yang, L. Tao, F. Zhou, X. Wei, Phototherapy of Neurodegenerative Diseases: Mechanism, Application, and Prospect, *Chinese Journal of Engineering Science* 22(3) (2020).
- [6] H. Chung, T. Dai, S.K. Sharma, Y.Y. Huang, J.D. Carroll, M.R. Hamblin, The nuts and bolts of low-level laser (light) therapy, *Ann Biomed Eng* 40(2) (2012) 516-33.
- [7] J.T. Eells, M.T. Wong-Riley, J. VerHoeve, M. Henry, E.V. Buchman, M.P. Kane, L.J. Gould, R. Das, M. Jett, B.D. Hodgson, D. Margolis, H.T. Whelan, Mitochondrial signal transduction in accelerated wound and retinal healing by near-infrared light therapy, *Mitochondrion* 4(5-6) (2004) 559-67.
- [8] A. Honmura, A. Ishii, M. Yanase, J. Obata, E. Haruki, Analgesic effect of Ga-Al-As diode laser irradiation on hyperalgesia in carrageenin-induced inflammation, *Lasers Surg Med* 13(4) (1993) 463-9.
- [9] A. Bradford, A. Barlow, P.L. Chazot, Probing the differential effects of infrared light sources IR1072 and IR880 on human lymphocytes: evidence of selective cytoprotection by IR1072, *J Photochem Photobiol B* 81(1) (2005) 9-14.
- [10] S. Purushothuman, D.M. Johnstone, C. Nandasena, J. Mitrofanis, J. Stone, Photobiomodulation with near infrared light mitigates Alzheimer's disease-related pathology in cerebral cortex - evidence from two transgenic mouse models, *Alzheimers Res Ther* 6(1) (2014)
- [11] S.L. Grillo, N.A. Duggett, A. Ennaceur, P.L. Chazot, Non-invasive infra-red therapy (1072 nm) reduces β -amyloid protein levels in the brain of an Alzheimer's disease mouse model, *TASTPM, J Photochem Photobiol B* 123 (2013) 13-22.
- [12] D. Farfara, H. Tuby, D. Trudler, E. Doron-Mandel, L. Maltz, R.J. Vassar, D. Frenkel, U. Oron, Low-level laser therapy ameliorates disease progression in a mouse model of Alzheimer's disease, *J Mol Neurosci* 55(2) (2015) 430-6.
- [13] L. De Taboada, J. Yu, S. El-Amouri, S. Gattoni-Celli, S. Richieri, T. McCarthy, J. Streeter, M.S. Kindy, Transcranial laser therapy attenuates amyloid- β peptide neuropathology in amyloid- β protein precursor transgenic mice, *J Alzheimers Dis* 23(3) (2011) 521-35.
- [14] M.M. Comerota, B. Krishnan, G. Tagliatalata, Near infrared light decreases synaptic vulnerability to amyloid beta oligomers, *Sci Rep* 7(1) (2017) 15012.
- [15] S. Purushothuman, D.M. Johnstone, C. Nandasena, J. Eersel, L.M. Ittner, J. Mitrofanis, J. Stone, Near infrared light mitigates cerebellar pathology in transgenic mouse models of dementia, *Neurosci Lett* 591 (2015) 155-9.
- [16] F. Darlot, C. Moro, N. El Massri, C. Chabrol, D.M. Johnstone, F. Reinhart, D. Agay, N. Torres, D. Bekha, V. Auboiroux, T. Costecalde, C.L. Peoples, H.D. Anastascio, V.E. Shaw, J. Stone, J. Mitrofanis, A.L. Benabid, Near-infrared light is neuroprotective in a monkey model of Parkinson disease, *Ann Neurol* 79(1) (2016) 59-75.
- [17] C. Peoples, S. Spana, K. Ashkan, A.L. Benabid, J. Stone, G.E. Baker, J. Mitrofanis, Photobiomodulation enhances nigral dopaminergic cell survival in a chronic MPTP mouse model of Parkinson's disease, *Parkinsonism Relat Disord* 18(5) (2012) 469-76.
- [18] V.E. Shaw, S. Spana, K. Ashkan, A.L. Benabid, J. Stone, G.E. Baker, J. Mitrofanis, Neuroprotection of midbrain dopaminergic cells in MPTP-treated mice after near-infrared light treatment, *J Comp Neurol* 518(1) (2010) 25-40.
- [19] F. Schiffer, A.L. Johnston, C. Ravichandran, A. Polcari, M.H. Teicher, R.H. Webb, M.R. Hamblin, Psychological benefits 2 and 4 weeks after a single treatment with near infrared light to the forehead: a pilot study of 10 patients with major depression and anxiety, *Behav Brain Funct* 5 (2009) 46.
- [20] S.G. Disner, C.G. Beevers, F. Gonzalez-Lima, Transcranial Laser Stimulation as Neuroenhancement for Attention Bias Modification in Adults with Elevated Depression Symptoms, *Brain Stimul* 9(5) (2016) 780-787.
- [21] P.A. Lapchak, Taking a light approach to treating acute ischemic stroke patients: transcranial near-infrared laser therapy translational science, *Ann Med* 42(8) (2010) 576-86.
- [22] B.N. Huisa, A.B. Stemer, M.G. Walker, K. Rapp, B.C. Meyer, J.A. Zivin, Transcranial laser therapy for acute ischemic stroke: a pooled analysis of NEST-1 and NEST-2, *Int J Stroke* 8(5) (2013) 315-20.
- [23] Y. Lampl, J.A. Zivin, M. Fisher, R. Lew, L. Welin, B. Dahlof, P. Borenstein, B. Andersson, J. Perez, C. Caparo, S. Ilic, U. Oron, Infrared laser therapy for ischemic stroke: a new treatment strategy: results of the NeuroThera Effectiveness and Safety Trial-1 (NEST-1), *Stroke* 38(6) (2007) 1843-9.
- [24] M.A. Naeser, A. Saltmarche, M.H. Krengel, M.R. Hamblin, J.A. Knight, Improved cognitive function after transcranial, light-emitting diode treatments in chronic, traumatic brain injury: two case reports, *Photomed Laser Surg* 29(5) (2011) 351-8.
- [25] T. Ando, W. Xuan, T. Xu, T. Dai, S.K. Sharma, G.B. Kharkwal, Y.Y. Huang, Q. Wu, M.J. Whalen, S. Sato, M. Obara, M.R. Hamblin, Comparison of therapeutic effects between pulsed and continuous wave 810-nm wavelength laser irradiation for traumatic brain injury in mice, *PLoS One* 6(10) (2011) e26212.
- [26] M.A. Naeser, M.R. Hamblin, Potential for transcranial laser or LED therapy to treat stroke, traumatic brain injury, and neurodegenerative disease, *Photomed Laser Surg* 29(7) (2011) 443-6.

- [27] C. Meng, Z. He, D. Xing, Low-Level Laser Therapy Rescues Dendrite Atrophy via Upregulating BDNF Expression: Implications for Alzheimer's Disease, *The Journal of Neuroscience* 33(33) (2013) 13505-13517.
- [28] Y. Lu, R. Wang, Y. Dong, D. Tucker, N. Zhao, M.E. Ahmed, L. Zhu, T.C. Liu, R.M. Cohen, Q. Zhang, Low-level laser therapy for beta amyloid toxicity in rat hippocampus, *Neurobiol Aging* 49 (2017) 165-182.
- [29] S.S. Yoon, S.A. Jo, Mechanisms of Amyloid-beta Peptide Clearance: Potential Therapeutic Targets for Alzheimer's Disease, *Biomol Ther (Seoul)* 20(3) (2012) 245-55.

MITOGENETIC EFFECT (STIMULATION OF MITOSES WITH ULTRA-WEAK UV-RADIATION) AND ITS APPLICATIONS TO CANCER RESEARCH AND DIAGNOSTICS

ILYA VOLODYAEV¹ AND ELENA NAUMOVA²

¹*Biological faculty, M.V. Lomonosov Moscow State University, Russia*

²*D Rzhanov Institute of Semiconductor Physics, Russian Academy of Science, Russia*

a_naumova@isp.nsc.ru

Abstract

The report briefly reviews early researches on the mitogenetic effect (1923-1948) including the cancer diagnostics based on this effect and the claimed tumor marker. The key methodical details of mitogenetic effect observation are pointed out on the ground of the relevant literature and practical experience of one of the authors (IV). Prospects and necessity of the unambiguous verification of mitogenetic effect and related cancer diagnostics are shown. The review covers both published and unpublished materials from the unique archive by A.G. Gurwitsch and his scientific dynasty.

The phenomena of ultraweak endogenous radiation of biological systems and mitotic rate stimulation with ultra-weak UV-radiation were discovered by A.G. Gurwitsch in 1923 [1]. He directed the root of one onion (inducer) onto the meristem zone of the other root (detector) and observed that the inducer locally stimulated mitoses in the detector. This phenomenon was called a mitogenetic effect. The factor that mediated mitogenetic effect was shown to be ultraviolet radiation (chemical isolation of the inducer from the detector and insertion of quartz plate did not influence the effect, while a glass plate eliminated it). It was called mitogenetic radiation. Mitogenetic effect was observed in microbe and cell cultures, and tissues. When an inducer and a detector belonged to different families or even kingdoms the effect was also observed. There were more than 700 publications devoted to mitogenetic effect in 1923-1948. This effect was proved by more than hundred researchers including Nobel Prize Winner D. Gabor, academician G.M. Frank, famous microbiologist C. Wolff and others [2-6].

The spectra of mitogenetic radiation of various inducers were studied with spectrographs having rows of biological detectors instead of photographic plates [7, 8]. Spectra of most of the biological inducers were reported to be within the range of 190-250 nm, mitogenetic effect was induced also by a number of biochemical and even inorganic chemical reactions [9]. It was suggested that an energy released in chemical reactions involving free radicals resulted in the excitation of specific molecules or groups and could be emitted as quanta of mitogenetic radiation [10]. Intensity of mitogenetic radiation was estimated with modified Geiger-Müller counters as 10-1000 photons/cm² s [9].

The study of cancer cells and early cancer diagnostics were the most developed practical applications of mitogenetic effect. Whole blood and blood serum of young, healthy animals and people were proved to be good inducers of mitogenetic effect, while blood of cancer patients and animals did not induce it [11, 12]. The lacking of mitogenetic effect from blood was actually not an utterly specific indicator of cancer. For instance, blood of exhausted people did not induce mitogenetic effect also [13]. It was an ability of blood being added to any other known inducer to inhibit mitogenetic effect, that was really specific for cancer patients [14-16]. The substance responsible for the luminescence quenching in inducers was highly specific for cancer diseases and was called a "cancer quencher". Nowadays, it is alpha-fetoprotein that is generally recognized as the first tumor marker. However, an existence of a tumor marker in blood, which was called cancer quencher, was claimed almost thirty years earlier. The physical and chemical properties of the cancer quencher were studied and it was shown to be a peptide. An important fact shown in [17] and other works, was that blood of animals with experimental tumors (induced with chemical carcinogens, injection of suspension of malignant cells, or tumor transplantation) quenched luminescence of other inducers before the malignant process could be diagnosed clinically. Compliant results were obtained in clinics, for instance, the cancer quencher was found in blood of women with myoma only in those cases when they were to get cancer later, and before tumor could be diagnosed by any other means [17]. According to the ample clinical data of the leading medical institutions of the USSR gathered in 1940s the cancer diagnostics based on the detection of this tumor marker had specificity and sensitivity >95%. The detection was based on the lacking of mitogenetic effect from the yeast inducers to which the studied blood was added.

Researches on mitogenetic effect were conducted in 1928-1935 years mainly in the USSR and in Germany, and also in the USA, France, the Netherlands, Italy, Japan and other countries. In the USSR the works were persecuted altogether with genetics after the decisions of the All-Union Academy of Agricultural Sciences in 1948, see details in [18]. In Western countries these researches declined even earlier and were completely abandoned in the beginning of the World War II. It happened mainly due to historical reasons and a few influential negative publications (e.g. [19, 20]). Detailed analysis of methodical aspects of these works reveal severe violation of the methods suggested in the "positive" works (See [18]). The main points there are: (1) the recipient culture state (it should be a certain part of the lag-period or post-diauxic phase); (2) the time and duration of exposure (it should be optimized individually for each inducer-recipient pair;

the effect of over-exposure was observed in a many works); (3) some physical limitations, like the recipient culture density less than a certain limit, very thin suspension layers, semidarkness, lack of any external UV.

Further experiments on the subject were rather sporadic and gave no final proof or disproof of the key results of 1923-1948. One of us (IV) participated in attempts to reproduce mitogenetic effect, his scientific team managed to get a good reproducible effect from the yeast-inducer culture on the yeast-detector culture which was in the lag phase during the exposure [21]. Yet, the effect appeared to be caused by CO₂, which was secreted by the inducer and accepted by the detector (it was also shown to be signal-like action, but not purely metabolic). Later, analyzing their results in the context of publications of 1923-1948, the authors came to the conclusion that they paid not enough attention to methodical details of early works, and if the mitogenetic effect existed, it was sure not to manifest itself under used experimental conditions. First of all, it were the culture state and the medium composition that made mitogenetic effect observation impossible, and the effect, which was observed [21], had nothing to do with mitogenetic radiation that was the initial goal of the work (see [18]). After this failure the authors of paper [21] including the author of this report (IV) came to the deep reading of the methodical conditions of early works and besides their own mistakes, concluded that all the well-known “negative” works [19, 20, 22-25] also contained critical deviations from these methods, that would have guarantee their failure in the mitogenetic effect verification. Detailed methodical recommendations were given in a number of early works e.g.[26, 27], see also both positive and negative works analyzed from methodical viewpoint in [18] (Fig. 1).

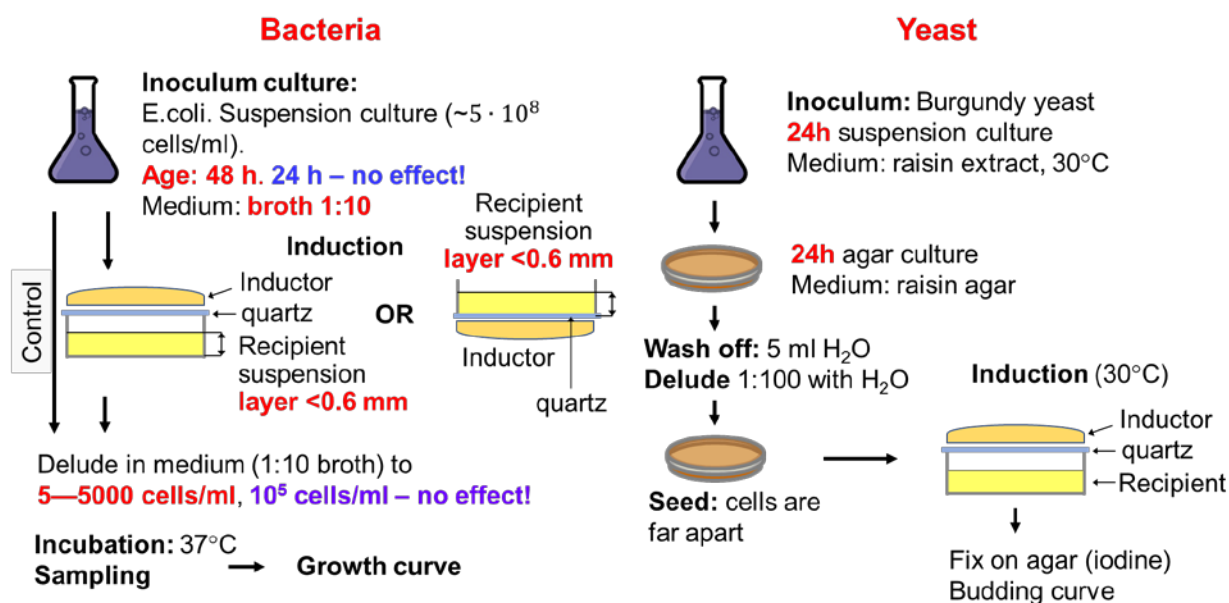


Figure 1: Modern analysis of the most effective methods for obtaining the mitogenetic effect on bacterial (left) and yeast (right) cultures (after [18])

Many conclusions made in experiments on MGE were proved to be correct and much ahead of their time. These are: an existence of tumor peptide markers in blood, photo-reactivation, anti-Stokes luminescence, free-radical mechanism of ultra-weak photon emission etc. Yet, the phenomenon itself remains an unresolved problem in both fundamental and applied biology till now in spite of the progress in UV-sensing. Particularly, photomultiplier tubes with AlGa_N photocathodes have a high spectral sensitivity in the whole mitogenetic range and extremely low dark counts that makes signal/noise ratio high enough for the unambiguous verification of experiments on mitogenetic radiation and related cancer diagnostic.

Verification of experimental results on mitogenetic effect and cancer quencher with the use of present-day techniques, knowledge and level of evidence is very promising both for basic science and practical applications and requires a thorough revision of early publications. More details about mitogenetic effect and cancer quencher can be found in monographs [8-10, 27-30] and reviews [18, 31, 32].

References

- [1] A. G. Gurwitsch, Die Natur des spezifischen Erregers der Zellteilung, Archiv für mikroskopische Anatomie und Entwicklungsmechanik, 100(1-2), 11-40, 1923.
- [2] T. Reiter, and D. Gabor, Ultraviolette Strahlen und Zellteilung, Strahlentherapie, (28), 125-131, 1928.
- [3] J. B. Tuthill, and O. Rahn, Zum Nachweis mitogenetischer Strahlung durch Hefesprossung, Archiv für Mikrobiologie, 4(1-4), 565-573, 1933.
- [4] A. J. Ferguson, and O. Rahn, Zum Nachweis mitogenetischer Strahlung durch beschleunigtes Wachstum von Bakterien, Archiv für Mikrobiologie, 4(1-4), 574-582, 1933.
- [5] L. K. Wolff, and G. Ras, Über Gurwitsch-Strahlen bei Bakterien, Acta Brevia Neerlandica de physiologia, pharmacologia, microbiologia, 1(7), 136-137, 1931.
- [6] W. Loos, Untersuchungen über mitogenetische Strahlen, Jahrb. Wiss. Bot., 72(4), 611-664, 1930.

- [7] G. Frank, Das mitogenetische Reizminimum und -maximum und die Wellenlänge mitogenetischer Strahlen, *Biologisches Zentralblatt*, 49), 129-141, 1929.
- [8] A. G. Gurwitsch, and L. D. Gurwitsch, Mitogenetic radiation: physical and chemical bases and applications in biology and medicine (in Russian), Medgiz, Moscow 1945.
- [9] A. G. Gurwitsch, and L. D. Gurwitsch, Mitogenetic radiation (in Russian), VIEM publishing house, Leningrad 1934.
- [10] A. G. Gurwitsch, and L. D. Gurwitsch, An introduction to the teaching of mitogenesis, USSR Academy of Medical Sciences Publishing House, Moscow, 1948.
- [11] L. D. Gurwitsch, and S. Salkind, Das mitogenetische Verhalten des Bluts Carcinomatoser, *Biochemische Zeitschrift*, 211(1-3), 362-372, 1929.
- [12] W. W. Siebert, Die mitogenetische Strahlung des Bluts und des Harns gesunder und kranker Menschen, *Biochemische Zeitschrift*, 226, 4/6), 253-256, 1930.
- [13] S. Brainess, Die mitogenetische Strahlung als Methode zum Nachweis und Analyse der Ermüdungserscheinungen, *Arbeitsphysiologie*, 6(1), 90-104, 1932.
- [14] W. Siebert, and H. Seffert, Zur Frage der Blutstrahlung bei Krankheiten, insbesondere bei Geschwülsten, *Biochemische Zeitschrift*, 289(6/2), 292-293, 1937.
- [15] A. G. Gurwitsch, and L. D. Gurwitsch, Mitogenetic analysis of cancer cell biology (In Russian), VIEM publishing house, M 1937.
- [16] A. G. Gurwitsch, L. D. Gurwitsch, S. Y. Zalkind et al., The teaching of the cancer quencher: Theory and clinics (in Russian), USSR Academy of Medical Sciences Press, Moscow 1947.
- [17] B. S. Pesochensky, The phenomenon of the mitogenetic radiation quenching in blood in cancer and "precancer": Dr. Med. Sci. Dissertation (in Russian), Leningrad Oncological Institute, Leningrad, 1942.
- [18] I. V. Volodyaev, and L. V. Belousov, Revisiting the mitogenetic effect of ultra-weak photon emission, *Frontiers in Physiology*, 6(00241), 1-20, 2015.
- [19] A. Hollaender, and W. D. Claus, An experimental study of the problem of mitogenetic radiation, National research council of the National academy of sciences, Washington 1937.
- [20] O. W. Richards, and G. W. Taylor, "Mitogenetic rays" - a critique of the yeast-detector method, *The Biological Bulletin*, 63(1), 113-128, 1932.
- [21] I. V. Volodyaev, E. N. Krasilnikova, and R. N. Ivanovsky, CO₂ mediated interaction in yeast stimulates budding and growth on minimal media, *PLoS One*, 8(4), e62808-e62808, 2013. 10.1371/journal.pone.0062808
- [22] G. W. Taylor, and E. N. Harvey, The theory of mitogenetic radiation, *Biolog. Bull.*, 61(3), 280-293, 1931.
- [23] K. H. Kreuchen, and J. B. Bateman, Physikalische und biologische Untersuchungen über mitogenetische Strahlung, *Protoplasma*, 22(1), 243-273, 1934.
- [24] T. I. Quickenden, and R. N. Tilbury, An Attempt to Stimulate Mitosis in *Saccharomyces cerevisiae* with the ultraviolet luminescence from exponential phase cultures of this yeast, *Radiation Research* 254-263, 102), 254-263, 1985.
- [25] T. I. Quickenden, A. J. Matich, S. H. Pung et al., An attempt to stimulate cell division in *Saccharomyces cerevisiae* with weak ultraviolet light, *Radiation Research*, 117(1), 145-157, 1989.
- [26] A. G. Gurwitsch, Methodik der mitogenetischen Strahlenforschung, in the Book "Handbuch der biologischen Arbeitsmethoden", E. Abderhalden, ed., 2/2, Urban & Schwarzenberg, Berlin, Wien, 1401-1470 1929.
- [27] T. Reiter, and D. Gabor, Zellteilung und Strahlung, Springer-Verlag, Berlin 1928.
- [28] A. A. Gurwitsch, The Problem of mitogenetic emission as an aspect of molecular biology (in Russian), Leningrad, Meditzina, 1968.
- [29] E. van Wijk, I. V. Volodyaev, Cifra, M. et al., Ultra-weak photon emission from biological systems: endogenous biophotonics and intrinsic biological luminescence (in print), Springer, 2020.
- [30] O. Rahn, Invisible radiations of organisms, Gebrüder Bornträger, Berlin 1936.
- [31] A. G. Gurwitsch, and L. D. Gurwitsch, Twenty Years of Mitogenetic Radiation: Emergence, Development, and Perspectives (translation from *Advances in Contemporary Biology*, 305-334 16 (3), 1943), *21st Century Science and Technology Magazin*, 12(3), 41-53, 1999.
- [32] E. V. Naumova, A. E. Naumova, D. A. Isaev et al., Historical review of early researches on mitogenetic radiation: from discovery to cancer diagnostics, *Journal of Biomedical Photonics & Engineering*, 4(4), 040201, 2018.

EXPRESS DIAGNOSTICS OF ERYTHROCYTES SIZE DISTRIBUTION ON THE BASIS OF HYPERSPETRAL HOLOGRAPHY AND LASER DIFFRACTOMETRY TECHNIQUES

ANDREI LUGOVTSOV^{1,2}, VLADISLAV USTINOV³, GEORGY KALENKOV⁴, SERGEY KALENKOV⁵ AND
ALEXANDER PRIEZZHEV^{1,2}

¹*Physics Department, Lomonosov Moscow State University, Russia*

²*International Laser Center, Lomonosov Moscow State University, Russia*

³*Moscow Center of Fundamental and Applied Mathematics, Lomonosov Moscow State University, Russia*

⁴*Institute of Geosphere Dynamics RAS, Russia*

⁵*Moscow Polytechnic University, Russia*

anlug@biomedphotonics.ru

Abstract

Modern medical diagnostics includes blood tests on the first stages that provides very important information allowing to insure the accuracy of further diagnosis. Red cell distribution width (RDW) is known as a crucial parameter in case of blood anemia. RDW is a measure of how much the erythrocytes differ from each other in size. RDW is close to zero, when all cells have similar size, and increases when the sizes are different. RDW has been evaluated for decades, and its application field grows rapidly. Recent investigation performed with more than 8000 people shows that RDW serves as a reliable mortality predictor independent of the disease type [1]. Thus, accurate diagnostic instruments for measuring this parameter are in high demand.

In this work, we developed the approach for diagnostics of erythrocytes size based on the information obtained by laser diffractometry and hyperspectral holography of erythrocytes. In laser diffractometry, erythrocytes are illuminated by a laser beam and a diffraction pattern is observed in the far-field diffraction zone. One can solve an integral equation, in which the diffraction pattern is used as an input data and the solution is the erythrocytes size distribution [2]. Another strategy is to rely on certain features of the diffraction pattern. For example, the visibility of the pattern reflects the shape and size of particles. In [3], it was shown that the visibility of the diffraction pattern monotonically depends on RDW of the cells in the given blood sample. Thus, laser diffractometry allows one to assess the value of RDW. It is possible to illuminate hundreds of thousands of cells within a moment. Calculation of the visibility parameter can also be performed during less than a second using any modern personal computer. This makes the method more preferable to other standards. However, the shape of the cells remains unknown as in the Coulter counter and one has to use some 3D geometrical model of the cells. In hyperspectral holography (HH), one obtains the phase modulation of the light rays passing through the object with resolution up to half of the incident light wavelength. HH technique has been well developed and successfully tested on biological particles [4]. In the present work, we have applied HH to measure the phase profiles of red blood cells on a glass smear. This enables one to reconstruct the 3D geometrical model of the erythrocytes shape. In this work, we use the specific technique developed in [4]. The main goal of the work is to enhance laser diffractometry of erythrocytes by using the 3D geometrical model of a real cell experimentally obtained using the HH method. The visibility of the diffraction pattern depends not only on RDW value but also on the cells shape. We validate the dependency of the visibility parameter on RDW comparing different theoretical and experimentally obtained cells models. Geometrical 3D models of human red blood cells in a dry smear were obtained experimentally using the HH method. Corresponding diffraction patterns in the far field diffraction zone were calculated. Visibility values of the diffraction patterns were obtained in cases of low and high red cell size distribution width. The results revealed that the visibility is influenced by the cells shapes. Namely, the visibility is always lower when using the model of real cells shape to compare with the case of ideal symmetric shapes. However, the visibility of the diffraction pattern still can be used to assess the red cell distribution width in clinical practice. The typical visibility value obtained in our calibration experiments was about 7%. Basing on the calculated dependency of the visibility of the diffraction pattern on the spread of cells in size, the relative spread of cells was determined to be 18 ± 4 %. The compact, computerized laser device based on the principles of ektacytometry (diffractometry) designed to measure the width of the distribution of size of erythrocytes has been developed.

Acknowledgement: This work was supported by the Russian Foundation for Basic Research grant №17-29- 03507-ofi-m.

References

- [1] K. V. Patel, L. Ferrucci, W. B. Ershler, D. L. Longo, and J. M. Guralnik, Red blood cell distribution width and the risk of death in middle-aged and older adults, *Archives of Internal Medicine* 169(5), 515–523, 2009.
- [2] D. L. Black, M. Q. McQuay, and M. P. Bonin, Laser-based techniques for particle-size measurement: a review of sizing methods and their industrial applications, *Progress in energy and combustion science* 22(3), 267–306, 1996.
- [3] S. Yu. Nikitin, A. E. Lugovtsov, A. V. Priezzhev, and V. D. Ustinov, Relation between the diffraction pattern visibility and dispersion of particle sizes in an ektacytometer, *Quantum Electronics* 41(9), 843–846, 2011.
- [4] S. G. Kalenkov, G. S. Kalenkov, and A. E. Shtanko, Hyperspectral holography: an alternative application of the Fourier transform spectrometer, *Journal of the Optical Society of America B* 34(5), B49–B55, 2017.

CHARACTERIZATION OF TISSUE ELASTICITY WITH OPTICAL COHERENCE ELASTOGRAPHY: GOING BEYOND THE LINEAR PARADIGM

VLADIMIR Y. ZAITSEV¹, ALEXANDER A. SOVETSKY¹, LEV A. MATVEEV¹, ALEXANDER L. MATVEYEV¹, EKATERINA V. GUBARKOVA², ANTON A. PLEKHANOV², MARINA A. SIROTKINA² AND NATALIA D. GLADKOVA²

¹*Institute of Applied Physics of the Russian Academy of Sciences, Russia*

²*Institute of Experimental Oncology and Biomedical Technologies, Privolzhsky Research Medical University, Russia*

vyuzai@ipfran.ru

Abstract

In this report we present recent results related to characterization of nonlinear elastic properties of biological tissues using quantitative Compression Optical Coherence Elastography (C-OCE) with application of reference silicone layers as optical stress sensors. In the reduced form this approach has already proven its efficiency for estimation of the tangent Young's modulus of nonlinear tissues for a standardized pressure. Analysis of entire stress-strain dependences opens new possibilities for diagnostics of biological tissues, which was inaccessible within the framework of conventionally used paradigm of linear elasticity.

C-OCE is an emerging approach to studying mechanical properties of biological tissues [1]. The idea of this approach was borrowed from the medical ultrasound elastography [2] and was introduced in OCT by J. Schmitt [3] based on the paradigm of linear elasticity of the tissue. Within the framework of this paradigm it is supposed that the values of uniaxial stress σ the values of stress and the resultant axial strain ε are linearly proportional to each other:

$$\sigma = E\varepsilon \quad (1)$$

The axial strain in OCT can be found by comparing subsequently acquired OCT scans, namely, by estimating axial gradients of interframe phase variations using either classical least-square procedures [4] or recently proposed more advanced "vector" method [5, 6].

It is clear from Eq. (1) that in order to quantify modulus E , knowing only local strain ε is not sufficient, so that estimation of stress σ is also required. In principle, one can try to evaluate stress σ by measuring the force applied to the tissue from the OCT probe with a known contacting area. However, in [2] and [3] it was proposed that the spatial distribution of the Young's modulus (at least in the relative sense) can be extracted from the initially reconstructed axial profiles of strain. Indeed, if the deformation is produced by uniaxial stress (i.e., the tissue is allowed to freely expand laterally) the stress σ is the same for different depths with the Young's moduli $E_{1,2}$ and the corresponding strains $\varepsilon_{1,2}$ of the tissue, so that

$$\sigma = E_1\varepsilon_1 = E_2\varepsilon_2, \quad (2)$$

or equivalently

$$E_1/E_2 = \varepsilon_2/\varepsilon_1 \quad (3)$$

The measurement of the axial strain distribution, therefore, is the key step in deconstructing the distribution of the Young's modulus. Equations (2) and (3) mean that the depth distribution of local strains is directly proportional to relative distribution of inverse Young's modulus $1/E$. Therefore, if in some area this modulus is known, this opens the possibility to quantify the elastic modulus over the entire imaged region. This idea was mentioned quite long ago [2], but did not find application in ultrasound compression elastography, whereas in compression OCE the utilization of translucent reference layers (usually made of soft silicone) is efficiently used for quantifying the tissue elasticity [7,8]. Although in C-OCE typical values of interframe strain are on the order of 10^{-4} .. 10^{-3} , for which the linear Eqs.(2)and(3) hold fairly well, quite often larger strains (up to several per cent and greater) are produced in the tissue. In many cases the tissue surface is not ideally plane, so that even if a highly compliant silicone layer is placed between the OCT-probe window and the sample, the mechanical contact over the entire visualized zone is attained only when the most prominent tissue areas are strained up to several per cent. With further compression the strain becomes even greater. Such strains cannot be directly measured by comparing individual OCT scans, but can be estimated by analyzing a series of scans acquired during the tissue deformation and finding cumulative strains for such a series [8, 9]. For such larger strains, biological tissues exhibit rather

pronounced nonlinear elasticity [10]. In such a case the stress-strain dependence $\sigma(\varepsilon)$ for the tissue is essentially nonlinear, whereas linearized Eq.(1) may hold only for sufficiently small increments in stress $\Delta\sigma$, and strain $\Delta\varepsilon$, so that the elastic modulus becomes dependent on the tissue pre-compression,

$$E(\sigma) = \Delta\sigma / \Delta\varepsilon \quad (4)$$

To measure nonlinear stress-strain dependences $\sigma(\varepsilon)$, one needs to measure simultaneously strain in the tissue and the applied stress. In view of the above-mentioned fact that quite often the stress in the visualized region depends on the lateral coordinate, a method is needed to estimate the current local stress during the tissue deformation. In this regard an important question arises whether it is possible to use reference silicone layers as stress sensors not only for very small strains, but for larger strains as well. In other words, how strong is the nonlinearity of silicone? To verify this point the straightforward solution is to independently measure stress and strain, which is quite challenging because of numerous possible distorting factors (such as the influence of stiction between the OCT-probe and silicone as discussed in [8]). However, there is another solution proposed in [3]. It is based on utilization of a sandwich structure made of two silicones with highly contrasting strains. During the compression of this sandwich one may compare the cumulative strains in two silicones by plotting one strain against the other to verify if this dependence is linear or nonlinear. The stiffer silicone is deformed weaker (still remaining in the definitely linear region of straining), whereas the softer experiences significantly stronger deformation and thus can potentially exhibit pronounced nonlinearity, whereas for linearly deformed materials, the strains should remain proportional to each other resulting in a linear dependence. It has been experimentally verified that strains of two silicones in such compressed sandwich structures demonstrate very good linear proportionality up to quite large strains over 50% (see Fig. 1a).

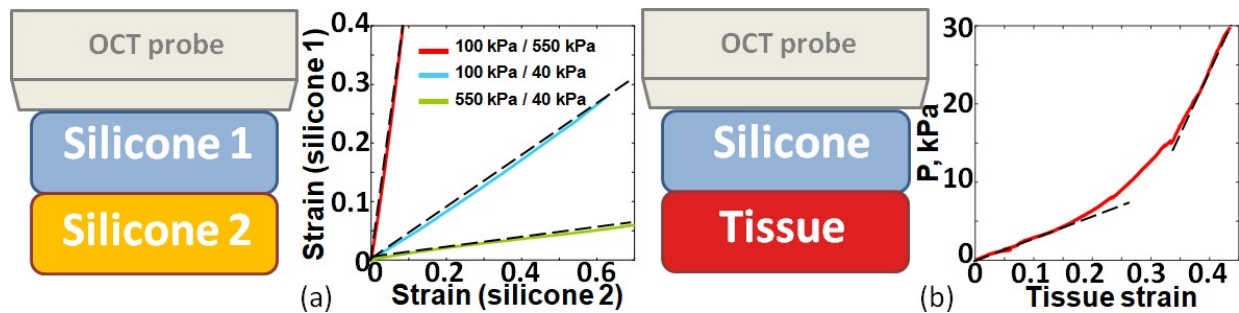


Figure 1: (a) Illustration of the self-testing of silicones' linearity using compression of a sandwich composed of two silicone layers with contrasting stiffness. (b) An example of nonlinear stress-strain curve for normal breast stroma obtained using a pre-calibrated silicone layer as the stress sensor.

This experimental finding indicates that silicones are rather linear materials, so that even for such fairly large strain in the reference silicone layer, its strain remains linearly proportional to stress. This means that pre-calibrated reference silicone layers may serve as optical stress sensors and can be used to local stress over the visualized region. Thus measuring cumulative strains in the reference silicone layer and plotting it against the cumulative strain in the tissue one can obtain nonlinear stress-strain curves for the examined tissue sample. An experimentally obtained example of such a curve is given in Fig. 1b corresponding to a normal stroma of human breast tissue. This figure demonstrates that for strains below ~15% the stress-strain dependence is rather linear with almost invariable slope (i.e., initially the Young's modulus is nearly invariable ~30kPa), whereas for larger strains the slope of $\sigma(\varepsilon)$ noticeably increases, so that the modulus becomes several times greater tending to ~150 kPa for strains >35%). It can be pointed out that for other components of breast tissue (pre-cancer states like fibrosis and hyalinosis and, furthermore, for cancerous tissues) similar stress-produced stiffening can be observed for several times smaller strains (even for strains ~1.5-2%) [8].

In view of such pronounced nonlinearity, unambiguous quantitative interpretation of C-OCE-based estimates of the elastic moduli and meaningful comparison with other measurements requires that one should specify the pressure, for which a particular value of the Young modulus is obtained. Even if a sample is strongly mechanically inhomogeneous and stress during the C-OCE examination is also inhomogeneous, it is possible to construct an OCE-image for a selected standardized pressure by processing a series of OCT images obtained during the sample compression (see details in [11]). Examples of quantitative interpretation of C-OCE data for the tissue stiffness estimated using the pressure standardization can be found in refs. [12,13,14].

In studies [12,13,14], however, the ability of the proposed method to obtain nonlinear stress-strain curves was utilized in the reduced form, only for estimation of the tangent (current) Young's modulus for a chosen standardized pressure. However, in fact the analysis of entire nonlinear stress-strain dependences suggests new diagnostic

information. In particular, nonlinear curves can be fitted using one or another analytical law, such that in addition to the Young's modulus, parameter(s) characterizing the tissue nonlinearity can be also extracted and used as additional diagnostic signatures of the tissue state (including classification of pathologies). To demonstrate diversity of nonlinear elastic properties for various types of biological tissues Fig. 2 shows examples of stress-strain curves and dependence of the tangent Young's modulus as a function of tissue strain for three significantly different samples: an excised fragment of human artery wall, excised rabbit's cornea and rat's cortex (in normal state). For cornea and the artery wall, the nonlinearity looks as pronounced tissue stiffening with increasing compression strain. In contrast, for cortex, the nonlinearity demonstrates qualitatively different character: the opposite sign corresponding to the decrease in the Young's modulus with increased compressive strain. In that experiment it was verified that the white matter and the tumor (astrocytoma) region also demonstrated qualitatively similar initial softening with increased compression, which was changed to slight stiffening with further compression. It is interesting to point out that in contrast to majority of other tumors (for which the Young's modulus is usually much higher than for the normal tissue), astrocytoma demonstrated initially more than twice lower stiffness than normal cortex and white matter. However, after fairly moderate ~5% strain astrocytoma demonstrated pronounced (about two times) stiffening, such that its Young's modulus could become comparable with its values for normal cortex and white matter. These results indicate that analysis of full nonlinear stress-strain dependences gives much richer information for differentiation of tissue types in comparison with conventionally discussed linear elastic modulus.

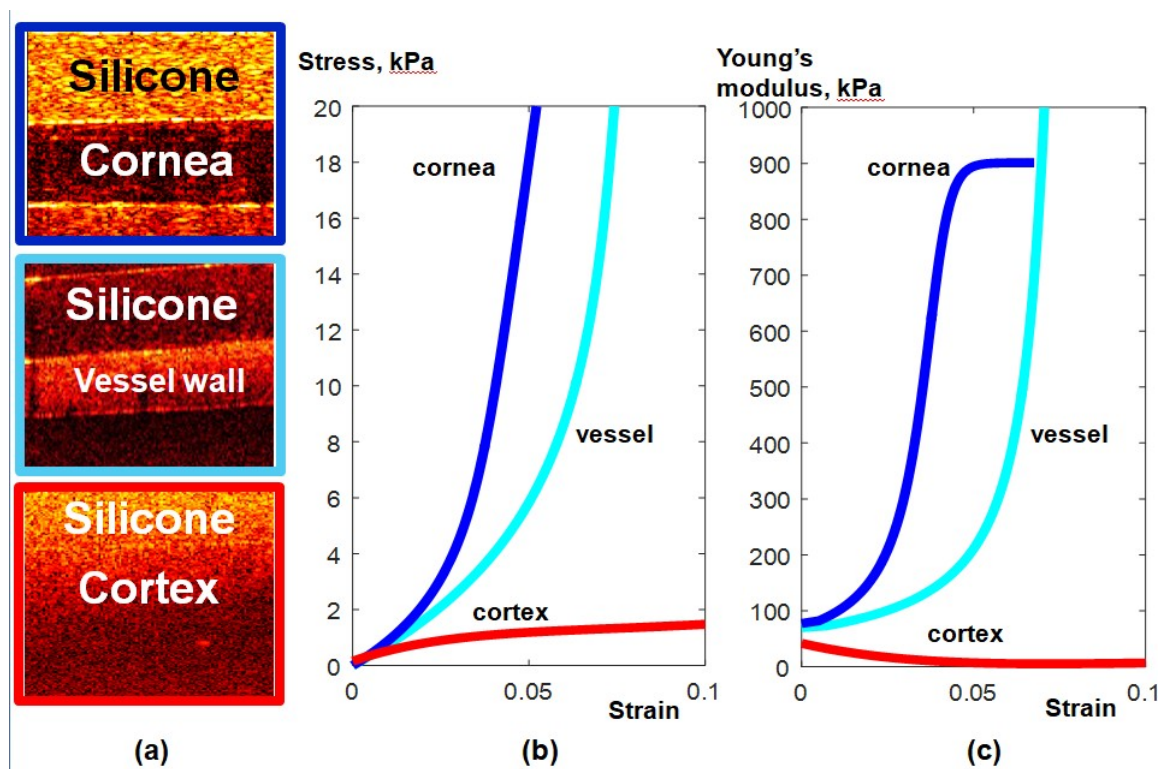


Figure 2: (a) examples of structural OCT scans for three different tissues (excised rabbit cornea, fragment of human artery wall and rat's cortex). (b) are the corresponding nonlinear stress-strain curves obtained by the C-OCE method using reference silicone layer as a linear stress sensor. (c) are the dependences on tangent Young's modulus derived from the stress-strain curves shown in panels (b).

Although the behavior of cortex (as well as white matter and astrocytoma) with atypical softening differs from the nonlinear behavior of most tissues, it can be pointed out that such nonlinearity is known for materials containing microstructural heterogeneities with threshold reaction to loading, for example, it was observed for an artificial material in the form of a homogeneous gel-like matrix with embedded hollow shells that experience buckling when compressive loading reaches certain threshold value [15]. Probably microstructural units with similar mechanical properties may occur in some natural tissues.

The nonlinearity of stiffening type (like for cornea and the vessel wall) is easier to understand. Such tissues with collagenous matrix are penetrated by narrow pores/gaps (often crack-like ones) through which interstitial physiological liquids penetrate, in particular to supply the tissue with nutrition. Such gaps are more compliant than the surrounding matrix tissue and with increasing compression these gaps gradually close, so that their concentration gradually decreases and the tissue becomes more dense and stiff. Such behavior is clearly demonstrated by cornea, in which the gaps among collagenous layers become nearly completely closed by reaching average strain ~5-7%. For

such compression, the stiffness of cornea increases by an order of magnitude and becomes comparable with stiffness of cartilaginous tissue. The compliance properties of such narrow gaps/pores resemble the properties of cracks that attract much attention in nondestructive testing, geophysics and related areas, where it is shown that the average strain producing closing of such narrow gaps is determined by their aspect ratio (i.e., the ration of the opening to the lateral size). The models describing crack-containing materials can be adapted to describe softening/stiffening of biological tissues due to the influence of interstitial gaps, such that the C-OCE data can be used to estimate averaged aspect ratio of such gaps [16] and even to reconstruct the distribution of these gaps over their aspect ratios [17].

Although the fact of pronounced elastic nonlinearity of biological tissues has been known over several decades, in OCE the linear-elasticity paradigm still remains dominating and the OCE-based methods for obtaining nonlinear stress-strain curves and their utilization for diagnostic applications are yet emerging (e.g., another variant of OCE-based method for obtaining stress-strain curves can be found in [18]). However, bearing in mind the recent breakthrough results on the development of C-OCE techniques [1] one can expect a similar breakthrough in the development of C-OCE beyond the linear paradigm, which should significantly extend diagnostic potential and accuracy of OCT-based elastographic methods.

This work was supported by RSN grant 16-15-10274 in part of the development of C-OCE method and RFBR grant 18-32-20056 in part of the analysis of nonlinear stress-strain dependences.

References

- [1] Zaitsev V.Y., Matveyev A.L., Matveev L.A., Sovetsky A.A., Hepburn M.S., Mowla A., Kennedy B.F. (2020) Strain and elasticity imaging in compression optical coherence elastography: the twodecade perspective and recent advances. *Journal of Biophotonics*: e202000257. doi:10.1002/jbio.202000257
- [2] Ophir J., Céspedes I., Ponnekanti H., Yazdi Y., and Li X. (1991) Elastography: A quantitative method for imaging the elasticity of biological tissues. *Ultrasonic Imaging* 13, 2: 111–134. [https://doi.org/10.1016/0161-7346\(91\)90079-w](https://doi.org/10.1016/0161-7346(91)90079-w)
- [3] Schmitt J.M. (1998) OCT elastography: imaging microscopic deformation and strain of tissue. *Optics Express* 3, 6:199.
- [4] Kennedy B.F., Koh S.H., McLaughlin R.A., Kennedy K.M., Munro P.R.T., Sampson D.D. (2012) Strain estimation in phase-sensitive optical coherence elastography. *Biomed Opt Express* 3:1865. <https://doi.org/10.1364/boe.3.001865>
- [5] Zaitsev V.Y., Matveyev A.L., Matveev L.A., Gelikonov G.V., Sovetsky A.A., and Vitkin A. (2016) Optimized phase gradient measurements and phase-amplitude interplay in optical coherence elastography. *Journal of Biomedical Optics* 21, 11: 116005. doi: 10.1117/1.JBO.21.11.116005
- [6] Matveyev A.L., Matveev L.A., Sovetsky A.A., Gelikonov G.V., Moiseev A.A., and Zaitsev V.Y. (2018) Vector method for strain estimation in phase-sensitive optical coherence elastography. *Laser Physics Letters* 15, 6: 65603. <https://doi.org/10.1088/1612-202x/aab5e9>
- [7] Kennedy K.M., Chin L., McLaughlin R.A., Latham B., Saunders C.M., Sampson D.D., and Kennedy B.F. (2015) Quantitative micro-elastography: imaging of tissue elasticity using compression optical coherence elastography. *Scientific Reports* 5, 1. doi:10.1038/srep15538
- [8] Zaitsev V.Y., Matveyev A.L., Matveev L.A., Gubarkova E.V., Sovetsky A.A., Sirotkina M.A., Gelikonov G.V., Zagaynova E.V., Gladkova N.D., and Vitkin A. (2017) Practical obstacles and their mitigation strategies in compressional optical coherence elastography of biological tissues. *Journal of Innovative Optical Health Sciences* 10, 6:1742006.
- [9] Sovetsky A.A., Matveyev A.L., Matveev L.A., Shabanov D.V., and Zaitsev V.Y. (2018) Manually-operated compressional optical coherence elastography with effective aperiodic averaging: demonstrations for corneal and cartilaginous tissues. *Laser Physics Letters* 15, 8: 85602. <https://doi.org/10.1088/1612-202x/aac879>
- [10] T. A. Krouskop, T. M. Wheeler, F. Kallel, B. S. Garra, and T. Hall. 1998. Elastic Moduli of Breast and Prostate Tissues under Compression. *Ultrasonic Imaging* 20, 4: 260–274. <https://doi.org/10.1177/016173469802000403>
- [11] Sovetsky A.A., Matveyev A.L., Matveev L.A., Gubarkova E.V., Plekhanov A.A., Sirotkina M.A., Gladkova N.D., Zaitsev V.Y. Full- optical method of local stress standardization to exclude nonlinearity-related ambiguity of elasticity estimation in compressional optical coherence elastography. *Laser Physics Letters*. 2020 May4;17(6):065601.
- [12] Gubarkova E.V., Sovetsky A.A., Zaitsev V.Y., Matveyev A.L., Vorontsov D.A., Sirotkina M.A., Matveev L.A., Plekhanov A.A., Pavlova N.P., Kuznetsov S.S., Vorontsov A.Y. OCT-elastography-based optical biopsy for breast cancer delineation and express assessment of morphological/molecular subtypes. *Biomedical optics express*. 2019 May 1;10(5):2244-63. doi:10.1364/BOE.10.002244
- [13] A. A. Plekhanov, M. A. Sirotkina, A. A. Sovetsky, E. V. Gubarkova, S. S. Kuznetsov, A. L. Matveyev, L. A. Matveev, E. V. Zagaynova, N. D. Gladkova, and V. Y. Zaitsev. 2020. Histological validation of in vivo assessment of cancer tissue inhomogeneity and automated morphological segmentation enabled by Optical Coherence Elastography. *Scientific Reports* 10, 11781. doi: 10.1038/s41598-020-68631-w
- [14] M. A. Sirotkina, E. V. Gubarkova, A. A. Plekhanov, A. A. Sovetsky, V. V. Elagin, A. L. Matveyev, L. A. Matveev, S. S. Kuznetsov, E. V. Zagaynova, N. D. Gladkova, and V. Y. Zaitsev. 2020. In vivo assessment of functional and morphological alterations in tumors under treatment using OCT-angiography combined with OCT-elastography. *Biomedical Optics Express* 11, 3: 1365. doi: 10.1364/BOE.386419
- [15] Zaitsev V.Y., Dyskin A., Pasternak E., & Matveev L.A. (2009) Microstructure-induced giant elastic nonlinearity of threshold origin:
- [16] Mechanism and experimental demonstration. *Europhys. Lett.*, 86(4), 44005. <https://doi.org/10.1209/0295-5075/86/44005>
- [17] Zaitsev V.Y., Matveyev A.L., Matveev L.A., Gelikonov G.V., Baum O.I., Omelchenko A.I., Shabanov D.V., Sovetsky A.A., Yuzhakov A.V., Fedorov A.A., Siplivy V.I., Bolshunov A.V., & Sobol E.N. (2019) Revealing structural modifications in thermomechanical reshaping of collagenous tissues using optical coherence elastography. *Journal of Biophotonics*, 12(3),

e201800250. <https://doi.org/10.1002/jbio.201800250>

- [18] Matveev L.A, Sovetsky A.A., Matveyev A.L., Baum O.I., Omelchenko A.I., Yuzhakov A.V., Sobol E.N., Zaitsev V.Y. Optical coherence elastography for characterization of natural interstitial gaps and laser-irradiation-produced porosity in corneal and cartilaginous samples. In *Biomedical Spectroscopy, Microscopy, and Imaging 2020* Apr 1 (Vol. 11359, p. 113590G). International Society for Optics and Photonics.
- [19] Qiu Y., Zaki F.R.Z., Chandra N., Chester S.A., & Liu X. (2016). Nonlinear characterization of elasticity using quantitative optical coherence elastography. *Biomedical Optics Express*, 7(11), 4702–4710.

TWO-COMPONENT DIELECTRIC FUNCTION OF GOLD NANOSTARS: NOVEL CONCEPT FOR THEORETICAL MODELING AND ITS EXPERIMENTAL VERIFICATION

NIKOLAI G. KHLBTSOV^{1,2}, SERGEY V. ZARKOV³, VITALY A. KHANADEV¹ AND YURI A. AVETISYAN³

¹*Institute of Biochemistry and Physiology of Plants and Microorganisms, Russian Academy of Sciences,*

²*Saratov State University, Russia*

³*Institute of Precision Mechanics and Control, Russian Academy of Sciences, Russia*

khlebtsov@ibppm.ru

Abstract

Plasmon resonances of gold nanostars can be tuned across 600–2000 nm, which makes them an attractive platform for applications. Rational design of nanostar morphology requires adequate computational models. The common approach, based on electromagnetic simulations with the bulk dielectric function, is not applicable to sharp nanostar spikes, typical of plasmon resonances above 800 nm. Here we suggest a two-component dielectric function in which the nanostar core is treated as a bulk material, whereas the size-corrected dielectric function of the spikes is treated in terms of a modified Coronado–Schatz model. In contrast to common simulations with bulk gold constants and in agreement with experimental observations, the simulated nanostar spectra show a strong reduction in the Q factor of the plasmonic peak. The effect of NIR water absorption on the calculated cross sections is negligible, and the simulated and measured two-peaked UV–vis–NIR extinction spectra of water colloids and AuNST monolayers on glass in air are in qualitative agreement.

Gold nanostars (AuNSTs) have attracted much research attention because they are uniquely tunable across the vis–NIR-I-II spectral bands, are easy to fabricate, can generate strong local fields near the spikes, and are low cytotoxic. These properties make AuNSTs promising for bioimaging, photothermal, and sensing applications [1,2]. The main obstacles to applications and fundamental studies of AuNSTs are their size polydispersity and multibranch random morphology, which result from poorly controlled seed-mediated synthesis [3]. On the other hand, it is owing to their multibranch morphology that AuNSTs are much less sensitive to their orientation with respect to the incident polarized light than are their well-developed and precisely controlled alternative—Au nanorods.

Rational design of AuNST morphology for single-particle photothermal and imaging platforms [4] and 2D SERS arrays requires adequate computational models including the frequency-dependent dielectric function of gold. Until now, to the best of our knowledge, the common practice—without any exceptions—has been the use of the bulk Au optical constants tabulated by Johnson and Christy (J–Ch) [5]. However, AuNSTs consist of two morphological components: (1) a quasispherical core with a typical diameter of above 20 nm; (2) thin anisotropic spikes with aspect ratios (length/base) in the range 3–8. Because of the strong size-dependent correction, the dielectric function of the thin anisotropic spikes may be very different from the tabulated bulk values. It is well known that simulations with a size-corrected dielectric function strongly increase the width of the plasmonic peak and decrease its amplitude. What is more, the recent development of 6-tip AuNSTs with the main plasmonic peak in the range 1000–2000 nm makes the use of the J–Ch data questionable. A very thorough reexamination of the bulk Au optical constants by Olmon *et al.* [6] for evaporated, template-stripped, and single-crystal gold samples clearly shows a notable deviation from the J–Ch data. Evidently, the input dielectric function may strongly affect the peak position. As a result, the fitting of simulated spectra to experimental measurements by varying AuNST morphology may produce biased parameters.

Quite recently, we suggested [7] a two-component dielectric function in which the nanostar core and spikes are treated in terms of different dielectric functions:

$$\varepsilon(\omega, \mathbf{r}) = \begin{cases} \varepsilon_c(\omega, \mathbf{r}), & \mathbf{r} \in V_{core}, \\ \varepsilon_s(\omega, \mathbf{r}), & \mathbf{r} \in V_{spike}, \end{cases} \quad (1)$$

where V_{core} and V_{spike} are the volumes of the core and spike, respectively. The core and spike components are calculated as $\varepsilon_{c,s}(\omega, \mathbf{r}) = \varepsilon_b(\omega) + \Delta\varepsilon(\omega, \mathbf{r}, l_{c,s})$, with the Lorenz–Drude correction to the tabulated bulk value $\varepsilon_b(\omega)$:

$$\Delta\varepsilon(\omega, \mathbf{r}, l_{c,s}) \equiv \Delta\varepsilon(\omega, l_{c,s}) = \frac{\omega_p^2}{\omega^2 + i\omega\gamma_b} - \frac{\omega_p^2}{\omega^2 + i\omega(\gamma_b + \gamma_{c,s})}. \quad (2)$$

where ω_p is the plasma frequency; γ_b is the damping constant of bulk gold; $l_{c,s}$ is the effective path length of the electrons in the core and spikes, respectively; and $\gamma_{c,s}$ takes into account three possible contributions from radiation

damping, surface-electron scattering, and chemical interface damping (CID) [8] $\gamma_{c,s} = \gamma_{c,s}^{rad} + \gamma_{c,s}^{surf} + \gamma_{c,s}^{CID}$. We have shown **[Ошибка! Залка не определена.]** that for typical AuNST cores, the size correction is small and the core dielectric function can be taken as the bulk value $\varepsilon_b(\omega)$. The radiation damping is proportional to the particle volume, and for thin spikes, we can neglect this contribution. Further, for spherical particles of radius R , the surface-scattering term scales like $1/R$. The same scaling is expected for CID damping, because the number of s -electrons interacting with the surface adsorbate is proportional to the particle volume, whereas the number of adsorbate molecules scales like R^2 . Thus, the surface and CID correction terms can be combined into one relation,

$$\gamma_s = (A_s^{surf} + A_s^{CID}) \frac{v_F}{l_s} = A_s \frac{v_F}{l_s}, \quad (3)$$

where A_s takes into account the surface-electron scattering and CID contributions, v_F is the Fermi velocity, and l_s is the effective path length. In Eq. (3), the effective length of the size-corrected dielectric function can be calculated in terms of a modified Coronado–Schatz model [9] for a conical spike of base radius R_s and height (length) h .

The next crucial point concerns appropriate values for the damping parameter A_s . Recent comparisons of simulated and experimental spectra on the basis of extinction measurements of monodisperse Au nanorod colloids, absorption experiments with single Au nanospheres and scattering experiments with single Au nanorods have shown that the best fitting value is about $A_s = 1/3$. This value should be considered a low limit for cetyltrimethylammonium bromide-coated Au nanorods. For other ligands, the CID contribution can be different. For example, in the case of dodecanethiol adsorption on Au nanorods, Foerster *et al.* reported $A_{surf} = 0.12$ and $A_{CID} = 0.34$, thus giving the total $A = 0.46$. On the other hand, for small Au clusters, the maximal A value approaches 1. In summary, the possible range of A_s values is 0.3–1.

In addition to the conventional NIR-I biotissue window (700–1000 nm), two other optical windows, namely NIR-II (1000–1350 nm) and NIR-III or shortwave IR (SWIR) (1550–1870 nm), have been identified recently [10]. In the NIR-III spectral band, water absorbs the incident light strongly. Therefore, an important question arises: what is the physical meaning, if any, of the commonly used extinction, absorption, and scattering cross sections for particles hosted in an absorbing medium [11]? This question has been extensively dealt with in recent years (for details, the readers are referred to paper [12] and references therein). The main conclusion is that for an absorbing host medium, the electromagnetic energy budget depends on the geometry of the measuring volume, the properties of the scattering particle, and the particle's position with respect to the incident light and detector. The only observable integral quantity is the extinction cross section, which cannot be written as the sum of the absorption and scattering cross sections in the same way as for a nonabsorbing host medium. In fact, being operationally defined in the usual way, the scattering and absorption cross sections become dependent on the particle position. By contrast, the extinction cross section is independent of the particle position and characterizes the particle itself.

To make rough estimates of water-absorption effects, we consider small gold spheres and spheroids in an absorbing host medium. For small spheroidal particles with semiaxes (a, b, b) , we suggested a new analytical expression:

$$C_{ext;a,b} = \pi R_{ev}^2 Q_{ext;a,b} = \pi R_{ev}^2 \frac{4k_0 R_{ev}}{\sqrt{\varepsilon_2}} \text{Im} \frac{\varepsilon_2(\varepsilon_r - 1)}{3 + 3L_{a,b}(\varepsilon_r - 1)} \quad (4)$$

where $k_0 = 2\pi/\lambda$ is the wave number in vacuum, $n_2 = n_2' + in_2'' = \sqrt{\varepsilon_2}$ is the medium's refractive index, and $\varepsilon_r = \varepsilon_1/\varepsilon_2$ is the particle relative permeability, R_{ev} is the equivolume sphere radius, and $L_{a,b}$ are the geometrical depolarization factors of the spheroids ($L_a + 2L_b = 1$). For randomly oriented particles $\langle C_{ext} \rangle = (C_{ext,a} + 2C_{ext,b})/3$. We have found that the effect of host absorption on the calculated cross sections is moderate for spheres and is quite negligible for spheroids. This validates our computations of the AuNST cross sections by using COMSOL Multiphysics v. 5.1 with a nonabsorbing refractive index of water.

A simplified 6-spike geometrical model of AuNSTs was obtained from the TEM data of Tsoulos *et al.* by fitting the calculated absorption peak position (with J–Ch Au constants) to the experimental range 1800–1900 nm. A similar model was also derived from TEM images of the AuNSTs synthesized in this work. We use the scattering geometry in which the incident electric field is polarized along one of the side spikes, because the optical properties of AuNSTs are determined mainly by the in-plane dipole excitation of spikes.

Figures 1A,B show the AuNST absorption and scattering spectra calculated with the bulk Au optical constants of J–Ch and Olmon *et al.* In addition to the main plasmonic peak, associated with the in-plane dipolar excitation of the collinear spike, there are two minor peaks (near 710 and 930 nm), associated with the hybridization of the core and spike multipolar plasmons. The spike peaks are increased by bonding with the gold core, which serves as a plasmonic

antenna. The integral absorption cross section dominates the scattering one by an almost one order of magnitude. The positions and magnitudes of the main peaks calculated with the two sets of bulk Au optical constants differ noticeably. Thus, any fitting procedure based on the comparison of experimental and calculated NIR-II-III spectra with the J-Ch input optical constants may produce biased output data.

Figures 1C,D show the spike size-correction effect on the absorption and scattering spectra. As expected, the size correction results in noticeable decrease and broadening of the main peaks. The minor peaks retain their magnitudes but also become broadened. The plasmonic dumping in the spikes affects the scattering peaks of the AuNSTs much more strongly than it affects the corresponding absorption peaks (see the insets in panels C and D).

Figure 2A shows three types of nanostars, as found by SEM. The NST-1 type particles (~74%) were typical surfactant-free AuNSTs with an average of 6 asymmetrical spikes. The type 2 particles (NST-2; 12%) were highly symmetrical multispiked “sea urchins” (average spike number, 20). Finally, the type 3 particles (NST-3; 14%) mostly had small protrusions and sometimes also one or two small spikes. Typically, the reported extinction spectra of the AuNSTs synthesized with the Vo-Dinh protocol display a single major peak between 650–1100 nm. Except for rare cases, there seem to be no studies of colloids in the NIR–SWIR region of 1200–2300 nm, because such spectrophotometers are uncommon. Close inspection of the reported UV–vis–NIR spectra of AuNSTs suggests that possible SWIR peaks were simply missed because of the limited spectral ranges of the spectrophotometers used.

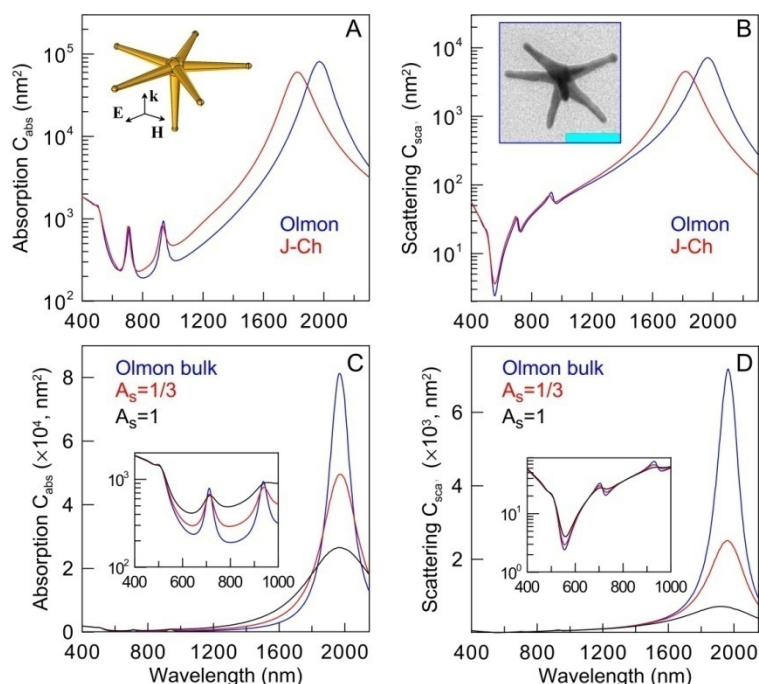


Figure 1: Absorption (A, C) and scattering (B, D) spectra of AuNSTs, as calculated with the bulk Au optical constants of Olmon *et al.* and J-Ch. Panels (C) and (D) illustrate the plasmonic dumping effect in the spikes with different dumping parameters. For cores, the bulk constants are used. The insets show the geometrical model of AuNSTs (A) and TEM image (B, scale bar is 50 nm).

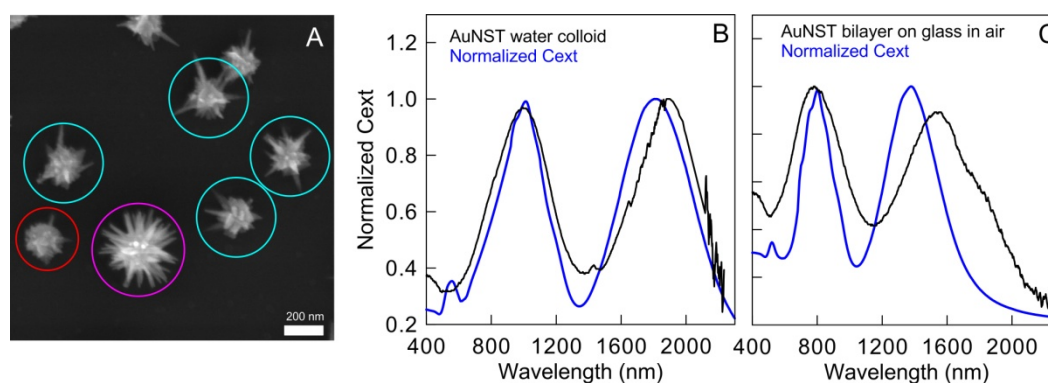


Figure 2: (A) Three types of AuNSTs, as found by SEM: NST-1 (cyan circles), NST-2 (magenta), and NST-3 (red). Panels (B) and (C) compare experimental (black) and simulated (blue) extinction spectra for water colloids (B) and bilayer on glass in air (C).

It is generally believed that the long spikes of surfactant-free AuNSTs correspond to typical broad plasmonic peaks observed experimentally between 800–1200 nm. In fact, however, such NIR peaks should be attributed to the short spikes of NST-1A subensemble, whereas the long-spike NST-1B subensemble produces the second plasmonic peak

located between 1800–2300 nm. To the best of our knowledge, this plasmonic feature of surfactant-free AuNSTs has never been noted previously. By using statistical data and derived electromagnetic model we were able to reproduce the main spectral features of water AuNST colloids and bilayer on glass in air (Figs. 2B,C, blue curves).

In summary, we have introduced a new two-component dielectric function for modeling the plasmonic properties of AuNSTs. The model takes into account the size-dependent plasmonic dumping mechanisms for thin spikes, whereas the core dielectric function is treated as a bulk material parameter. We have provided, for the first time, an analytical expression for the extinction cross sections of small spheroids embedded in an absorbing host medium. With this solution and COMSOL simulations, we have demonstrated negligible effects of water absorption on the calculated cross sections for a broad spectral range (300–2300 nm). By contrast, the size-dependent correction of plasmonic dumping in the spikes causes the dipolar and multipolar plasmonic peaks to broaden and decrease strongly.

Our extensive numerical simulations with various structural models have revealed several new features, which have not been reported previously:

(1) The core + two spikes nanostructure is a minimal structure that reproduces the basic spectral feature of 6-spike AuNAs and the more complex 20-spike AuNSTs.

(2) The addition of a third, 45° spike to a two-collinear spike configuration does not affect the two-spike spectra under collinear excitation; instead, it produces only a small shoulder under 45° excitation. When the incident field is directed along the 45° spike, it excites an intense dipolar plasmon and a strong local field around the neighbouring collinear spike, rather than around the exciting 45° spike. These observations contradict Zhu *et al.*'s [13] explanation of two peaks in AuNST spectra.

(3) The absorption spectra of spheroids and AuNAs in strongly absorbing media are close to those calculated for similar dielectric media. However, we have found unexpected behaviour of the scattering plasmonic peak, when water absorption increases it by almost 30%. Further work is needed to explain this effect.

(4) We have demonstrated a typical decrease in the quality factor of the absorption and scattering spectra with the damping parameter A_s increasing from 0 to 1. However, in some cases, we have found an unexpected increase in the main absorption peaks. This effect has been explained by a small increase in spike absorption, enhanced by plasmonic coupling with the core.

(5) For symmetrical multispike AuNSTs, we have demonstrated the polarization invariance of absorption spectra and have also shown the invariance of scattering spectra. Although the absorption and scattering spectra of 6-spike AuNSTs are not polarization invariant, we have shown (both numerically and analytically) the polarization invariance for a specific case when the electric field lies in the spike plane.

(6) We have explicitly demonstrated the broadening of spectra with an increase in the damping parameter and the absence of a broadening for polarization-dependent normalized spectra.

(7) For common surfactant-free AuNSTs, we have reported, for the first time, very intense SWIR plasmonic peaks around 1600–1900 nm. By thoroughly inspecting the SEM images of surfactant-free AuNSTs, we have found two clusters in the spike length–spike base diagrams and in the spike length and aspect ratio histograms. This morphological feature has been correlated with the experimentally observed two-peaked spectra. In contrast to general belief, we have shown that the common UV–vis–NIR plasmonic peak of the surfactant-free AuNSTs is related to the multiple short spikes, rather than to the long ones. The long spike produces an intense SWIR plasmonic mode, which has not been reported before for such nanostars.

(8) To simulate the experimental extinction spectra of colloids and bilayers on glass in air, we have developed a simplified three-fraction model consisting of typical Vo-Dinh AuNSTs (major NST-1 fraction, about 75%), multiple branched symmetrical sea urchins (NST-2), and particles with protrusions (NST-3). The spike length of the major fraction consists of two sub-ensembles of short (NST-1A) and long (NST-1B) spikes, which are presented on the same core and generate UV–vis–NIR (700–1100 nm) and SWIR (1600–1900 nm) plasmonic bands, respectively. With our model, we have demonstrated good agreement between simulated and measured spectra. The suggested model of the dielectric function and the reported results could be useful for a deeper understanding of the optical properties of morphologically complex AuNSTs.

Acknowledgment: This research was supported by the Russian Scientific Foundation (Project No. 18-14-00016). The work by VK on AuNST synthesis and characterization was supported by the Russian Scientific Foundation (Project No. 19-72-00120). The work by SZ and YA on electromagnetic simulations was supported by the Russian Foundation for Basic Research (Project No. 19-07-00378)

References

- [1] G. Chirico, M. Borzenkov and P. Pallavicini, *Gold Nanostars. Synthesis, Properties and Biomedical Application*. Springer, Cham, 2015.
- [2] T. V. Tsoulos et al. Colloidal plasmonic nanostar antennas with wide range resonance tunability. *Nanoscale* 11, 18662–18671, 2019

- [3] A. S De Silva Indrasekara, S. F. Johnson, R. A. Odion and T. Vo-Dinh, Manipulation of the geometry and modulation of the optical response of surfactant-free gold nanostars: a systematic bottom-up synthesis. *ACS Omega* 3, 2202–2210, 2018,
- [4] Y. Hu et al. Enhancing the Plasmon resonance absorption of multibranch gold nanoparticles in the near-infrared region for photothermal cancer therapy: theoretical predictions and experimental verification. *Chem. Mater.* 31, 471–482. 2019
- [5] P. B. Johnson and R. W. Christy, Optical Constants of the noble metals. *Phys. Rev. B* 6, 4370–4379, 1972.
- [6] R. L. Olmon et al. Optical dielectric function of gold. *Phys. Rev. B* 86, 235147, 2012,
- [7] N. G. Khlebtsov, S. V. Zarkov, V. Khanadeev and Y. A. Avetisyan. Novel concept of two-component dielectric function for gold nanostars: theoretical modelling and experimental verification. *Nanoscale*, 2020, DOI: 10.1039/D0NR02531C
- [8] B. Foerster et al. Plasmon damping depends on the chemical nature of the nanoparticle interface. *Sci. Adv.* 5, eaav0704, 2019.
- [9] Coronado E. A and Schatz G.C. Surface plasmon broadening for arbitrary shape nanoparticles: A geometrical probability approach. *J. Chem. Phys.* 119, 3926. 2003.
- [10] S. Golovynskyi et al. Optical windows for head tissues in near-infrared and short-wave infrared regions: approaching transcranial light applications. *J. Biophotonics* 11, e201800141, 2018.
- [11] C. F Bohren and D. P. Gilra, Extinction by a spherical particle in an absorbing medium. *J. Colloid Interface Sci.* 72 215–22, 1979.
- [12] M. I. Mishchenko and P. Yang, Far-field Lorenz–Mie scattering in an absorbing host medium: theoretical formalism and FORTRAN program. *J. Quant. Spectrosc. Radiat. Transfer* 205, 241–252, 2018.
- [13] J. Zhu, Gao, J.-J. Li and J.-W. Zhao, *Appl. Surf. Sci.* 322, 136–142, 2014.

MULTIMODAL TISSUE IMAGING AT OPTICAL CLEARING

VALERY V. TUCHIN

Saratov State University, Saratov, Russia
National Research Tomsk State University, Tomsk, Russia
Institute of Precision Mechanics and Control, Russian Academy of Sciences, Saratov, Russia

tuchinvv@mail.ru

Abstract

A description of ‘tissue optical virtual windows’ concept and method of optical clearing (OC) based on controllable and reversible modification of tissue or cell optical properties by their soaking with a biocompatible optical clearing agent (OCA) are presented in Refs. [1-27]. Fundamentals and major mechanisms of OC allowing one to enhance optical imaging facilities and laser treatment efficiency of living tissues and cells are also discussed in the literature [1-27].

In this work, perspectives of immersion optical clearing/contrasting technique aiming to enhance imaging of living tissues by using different imaging modalities working in the ultra-broad wavelength range from a free electron beam excitation (Cherenkov light emission) to terahertz waves are summarized in the Fig.1 [13, 25]. OC method improves and provides:

- Quantitative estimation of the concentration of chromophores and fluorophores of tissue at various depths
- Multi-category classification of tissue properties based on the extraction of meaningful multimodal spectroscopic biomarkers
- Clinically compatible spectroscopy-based methods of tissue pathology diagnosis
- Practical recommendations for increasing *in vivo* efficacy of diagnostics in UV/visible/NIR (200-2000 nm), THz combined with x-ray CT and MRI.

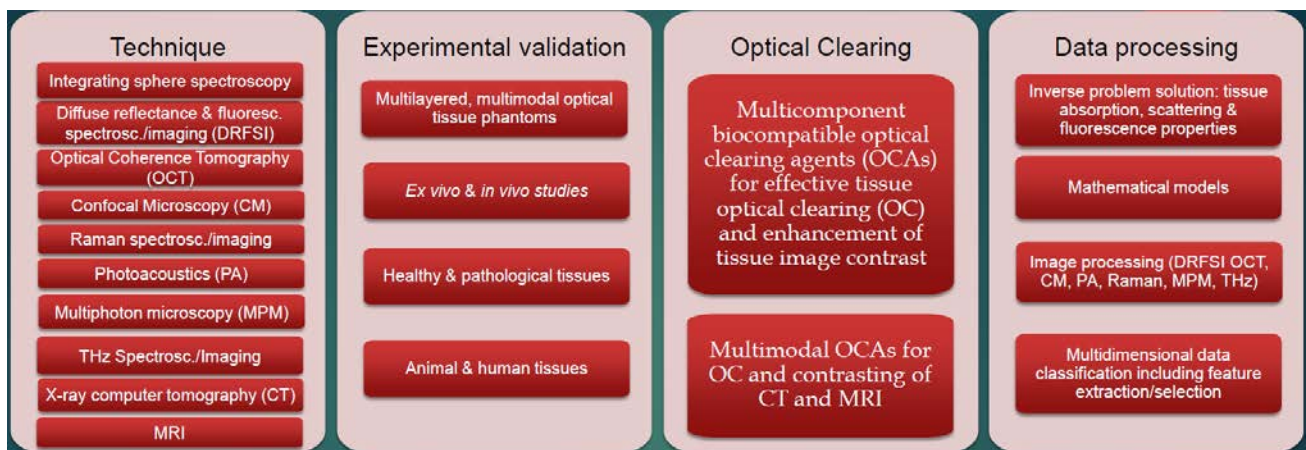


Figure 1: Multimodal approaches based on tissue optical clearing concept.

The enhancement of probing/treatment depth and image contrast for a number of human and animal tissues investigated by using different optical modalities, including diffuse reflectance spectroscopy, collimated transmittance, OCT, photoacoustic microscopy, linear and nonlinear fluorescence, SHG and Raman microscopies is possible. Experimental data on the diffusion and permeability coefficients of biocompatible FDA approved OCAs, such as glucose, glycerol, PEG, albumin, computer tomography (CT) contrast agents (Iohexol (OmnipaqueTM) and Iodixanol (VisipaqueTM)), and MRI contrast agents (Gadobutrol (GadovistTM)) in normal and pathological tissues (cancer and diabetes) are presented [1-27].

Optical clearing agents are beneficial for enhanced multimodal spectroscopy/imaging using different combinations of optical techniques such as Raman, OCT, FLIM, MPM, SHG, PA, Diffuse, and THz with X-ray CT and MRI.

Acknowledgment: This work was supported by RF Governmental Grant № 075-15-2019-1885 and RFBR grant 18-52-16025. Author is grateful for all his colleagues and co-authors for collaboration.

References

- [1] D. Zhu, K. V. Larin, Q. Luo, and V. V. Tuchin, Recent progress in tissue optical clearing, *Laser Photonics Rev.* **7**(5), 732–757, 2013.
- [2] E. A. Genina, A. N. Bashkatov, Yu. P. Sinichkin, I. Yu. Yanina, V.V. Tuchin, “Optical clearing of biological tissues: prospects of application in medical diagnostics and phototherapy,” *J. Biomed. Photonics & Eng.* **1**(1), 22–58, 2015.
- [3] V. V. Tuchin, Polarized light interaction with tissues, *J. Biomed. Opt.* **21**(7), 071114-1-37, 2016.
- [4] A.Yu. Sdobnov, M.E. Darvin, E.A. Genina, A.N. Bashkatov, J. Lademann, V.V. Tuchin, Recent progress in tissue optical clearing for spectroscopic application, *Spectroch. Acta Part A: Molec. & Biomol. Spectrosc.* **197**, 216–229, 2018.
- [5] O.A. Smolyanskaya, et al., “Terahertz biophotonics as a tool for studies of dielectric and spectral properties of biological tissues and liquids,” *Prog. Quant. Electr.* **62**, Nov. 1-77, 2018.
- [6] A. N. Bashkatov, et al., “Measurement of tissue optical properties in the context of tissue optical clearing,” *J. Biomed. Opt.* **23**(9), 091416, 2018.
- [7] D. K. Tuchina and V. V. Tuchin, Optical and structural properties of biological tissues under diabetes mellitus, *J. Biomed. Photonics & Eng.* **4**(2) 020201-1-22, 2018.
- [8] L. Oliveira and V. V. Tuchin, *The optical clearing method: A new tool for Clinical Practice and Biomedical Engineering*, Basel: Springer Nature Switzerland AG, 2019.
- [9] I. Carneiro, S. Carvalho, R. Henrique, L. Oliveira, and V. V. Tuchin, Kinetics of optical properties of colorectal muscle during optical clearing, *IEEE J. Selec. Tops Quant. Electr.* **25** (1), 7200608-8p., 2019.
- [10] D. K. Tuchina, P. A. Timoshina, V. V. Tuchin, A. N. Bashkatov, and E. A. Genina, Kinetics of rat skin optical clearing at topical application of 40% glucose: *ex vivo* and *in vivo* studies, *IEEE J. Selec. Tops Quant. Electr.* **25** (1), 7200508-8p., 2019.
- [11] I. Carneiro, S. Carvalho, R. Henrique, L. M. Oliveira, V.V. Tuchin, A robust *ex vivo* method to evaluate the diffusion properties of agents in biological tissues, *J. Biophoton.* **12**(4), e201800333, 2019.
- [12] Q. Xie, N. Zeng, Y. Huang, V. V. Tuchin, H. Ma, Study on the tissue clearing process using different agents by Mueller matrix microscope, *Biomed. Opt. Exp.* **10** (7), 3269-3280, 2019.
- [13] P. Rakotomanga, C. Soussen, G. Khairallah, M. Amouroux, S. Zaytsev, E. Genina, H. Chen, A. Delconte, C. Daul, V. Tuchin, W. Blondel, Source separation approach for the analysis of spatially resolved multiply excited autofluorescence spectra during optical clearing of *ex vivo* skin, *Biomed. Opt. Express* **10** (7), 3410-3424, 2019.
- [14] E. N. Lazareva, P. A. Dyachenko (Timoshina), A. B. Bucharskaya, N. A. Navolokin, and V. V. Tuchin, Estimation of dehydration of skin by refractometric method using optical clearing agents, *J. Biomed. Photon. Eng.* **5** (2), 020305, 2019.
- [15] I. Carneiro, S. Carvalho, R. Henrique, L. Oliveira, V. Tuchin, Moving tissue spectral window to the deep-ultraviolet via optical clearing, *J. Biophoton.* **12** (12), e201900181, 2019.
- [16] V.V. Tuchin, J. Popp, and V.P. Zakharov (Eds.), *Multimodal optical diagnostics of cancer*, Basel: Springer Nature Switzerland AG, 2020 600 p.
- [17] A.A. Selifonov, V.V. Tuchin, Determination of the kinetic parameters of glycerol diffusion in the gingival and dentinal tissue of a human tooth using optical method: *in vitro* studies. *Opt. Quant. Electron.* **52**, 123, 2020.
- [18] S. M. Zaytsev, Yu. I. Svenskaya, E. V. Lengert, G. S. Terentyuk, A. N. Bashkatov, V. V. Tuchin, E. A. Genina, Optimized skin optical clearing for optical coherence tomography monitoring of encapsulated drug delivery through the hair follicles, *J. Biophoton.* **13** (4) e201960020, 2020.
- [19] E.A. Genina, A.N. Bashkatov, G.S. Terentyuk, V.V. Tuchin Integrated effects of fractional laser microablation and sonophoresis on skin immersion optical clearing *in vivo*. *J. Biophoton.* **13**, e2020000101, 2020.
- [20] N. Gomes, V.V. Tuchin, L.M. Oliveira, UV-NIR efficiency of the refractive index matching mechanism on colorectal muscle during treatment with different glycerol osmolarities, *J. Biomed. Photon. Eng.* **6** (2) 020307, 2020.
- [21] Q. Lin, E.N. Lazareva, V.I. Kochubey, Y. Duan, V.V. Tuchin, Kinetics of optical clearing of human skin studied *in vivo* using portable Raman spectroscopy, *Laser Phys. Lett.* **17** (10), 105601, 2020.
- [22] E.A. Genina, Y.I. Surkov, I.A. Serebryakova, A.N. Bashkatov, V.V. Tuchin, V.P. Zharov, Rapid ultrasound optical clearing of human light and dark skin, *IEEE Trans. Med. Imaging.* **39** (10), 3198 -3206, 2020.
- [23] M. V. Novoselova, T. O. Abakumova, B. N. Khlebtsov, T. S. Zatsepina, E. N. Lazareva, V. V. Tuchin, V. P. Zharov, D. A. Gorin, E. I. Galanzha, Optical clearing for photoacoustic lympho- and angiography beyond conventional depth limit *in vivo*, *Photoacoustics* **20**, 100186, 2020.
- [24] K. V. Berezin, K. N. Dvoretzkiy, V. V. Nechaev, A. M. Likhter, I. T. Shagautdinova, and V. V. Tuchin, Optical clearing of human skin using polyethylene glycols, *J. Biomed. Photon. Eng.* **6**(2), 020308-1-5, 2020.
- [25] D.K. Tuchina, I.G. Meerovich, O.A. Sindeeva, V. V. Zherdeva, A. P. Savitsky, A. A. Bogdanov Jr, V. V. Tuchin, Magnetic resonance contrast agents in optical clearing: Prospects for multimodal tissue imaging. *J. Biophoton.* **13**(11), e201960249, 2020.
- [26] G. R. Musina, I. N. Dolganova, N. V. Chernomyrdin, A. A. Gavdush, V. E. Ulitko, O. P. Cherkasova, D. K. Tuchina, P. V. Nikitin, A. I. Alekseeva, N. V. Bal, G. A. Komandin, V. N. Kurlov, V. V. Tuchin, K. I. Zaytsev, Optimal hyperosmotic agents for tissue immersion optical clearing in terahertz biophotonics, *J. Biophoton.* **13**(12), e202000297, 2020.
- [27] I. Carneiro, S. Carvalho, R. Henrique, A. Selifonov, L. Oliveira, V.V. Tuchin, Enhanced ultraviolet spectroscopy by optical clearing for biomedical applications, *IEEE J. Selec. Tops Quant. Electr.* **27** (4), 1-8, 2021.

**Chinese-Russian Workshop on
Biophotonics and Biomedical Optics-2020
Book of Abstracts**

Edited by Polina A.Dyachenko, Dan Zhu, and
Valery V.Tuchin

SEPTEMBER 29 – 30, 2020

SARATOV

[Electronic resource]. - Electron, text data.(30 MB) -- 1 electron, opt. disk (CD-ROM). - Systems. Requirements: x86 processor with a clock speed of 500 MHz and higher; 512 MB of RAM; Windows XP / 7 / 8; SVGA 1280x1024 High Color (32 bit) video card; CD-ROM drive. - Title from the screen.

Publishing house "Saratovsky source"
Saratov, Kutyakova str. 138b, 3rd floor.
Tel. (8452) 52-05-93
E-mail: saristoch@bk.ru

[Электронный ресурс]. – Электрон, текстовые дан.(30 Мб) — 1 электрон, опт. диск (CD-ROM). – Систем. требования: процессор x86 с тактовой частотой 500 МГц и выше; 512 Мб ОЗУ; Windows XP/7/8; видеокарта SVGA 1280x1024 High Color (32 bit); привод CD-ROM. – Загл. с экрана.

Издательство «Саратовский источник»
г. Саратов, ул. Кутякова 138б, 3 этаж.
Тел. (8452) 52-05-93
E-mail: saristoch@bk.ru